UNCLASSIFIED

AD NUMBER

AD805746

NEW LIMITATION CHANGE

TO

Approved for public release, distribution unlimited

FROM

Distribution authorized to U.S. Gov't. agencies and their contractors; Administrative/Operational Use; JAN 1967. Other requests shall be referred to US Air Force Weapons Laboratory, Attn: Research and Technology Division, Kirtland AFB, NM.

AUTHORITY

AFWL ltr, 30 Nov 1971

THIS PAGE IS UNCLASSIFIED

AFWL-TR-65-67

AFWL-TR
65-67

STUDY OF WAVEFORM CHARACTERISTICS FOR USE IN THE ANALYSIS OF SHOCK ISOLATION SYSTEMS FOR UNDERGROUND PROTECTIVE STRUCTURES

H. R. Saffell
The Ralph M. Parsons Company

R. T. Frankian
R. T. Frankian and Associates

C. C. Chao
Agbabian-Jacobsen Associates

Contract AF 29(601)-6277

TECHNICAL REPORT NO. AFWL-TR-65-67
JANUARY 1967

AIR FORCE WEAPONS LABORATORY
Research and Technology Division
Air Force Systems Command
Kirtland Air Force Base
New Mexico

AFWL-TR-65-67

Research and Technology Division
AIR FORCE WEAPONS LABORATORY
Air Force Systems Command
Kirtland Air Force Base
New Mexico

This document is subject to special export controls and each transmittal to foreign governments or foreign nationals may be made only with prior approval of AFWL (WLDC), Kirtland AFB, NM, 87117. Distribution is limited because of the technology discussed in the report.

DO NOT RETURN THIS COPY. RETAIN OR DESTROY.

AFWL-TR-65-67

STUDY OF WAVEFORM CHARACTERISTICS FOR USE IN THE ANALYSIS OF SHOCK ISOLATION SYSTEMS FOR UNDERGROUND PROTECTIVE STRUCTURES

H. R. Saffell
The Ralph M. Parsons Company

R. T. Frankian
R. T. Frankian and Associates

C. C. Chao
Agbabian-Jacobsen Associates

The Ralph M. Parsons Company
Los Angeles, California 90017
Contract AF 29(601)-6277

TECHNICAL REPORT NO. AFWL-TR-65-67

This document is subject to special export controls and each transmittal to foreign governments or foreign nationals may be made only with prior approval of AFWL (WLDC), Kirtland AFB, NM, 87117. Distribution is limited because of the technology discussed in the report.

FOREWORD

This report was prepared by the Ralph M. Parsons Company, Los Angeles, California, under Contract AF 29(601)-6277. The research was performed under Project 1080, Task 108015, Subtask 13.167, and was funded by the Defense Atomic Support Agency (DASA).

Inclusive dates of research were 22 December 1963 to 13 December 1966. The report was submitted 19 December 1966 by the Air Force Weapons Laboratory Project Officer, Lt Glen N. Williams (WLDC).

Contributions to the work were made by R. T. Frankian of R. T. Frankian and Associates who investigated the use of the wavefront diagram, and Drs. C. C. Chao and L. S. Jacobsen, Agbabian-Jacobsen Associates, who examined the form and strengths of Rayleigh waves resulting from pressure distributions similar to those generated by nuclear bursts.

The project was managed by H. R. Saffell of the Ralph M. Parsons Company who also analyzed and compared the studies with the observed oscillations. The support and technical contributions of Lt John F. Flory, former AFWL Project Officer, are gratefully acknowledged.

This technical report has been reviewed and is approved.

Glen N Williams

GLEN N. WILLIAMS
Lt, USAF
Project Officer

ALLEN F. DILL
CDR, CEC, USNR
Chief, Civil Engineering Branch

George C. Darby, Jr.

GEORGE C. DARBY, JR.
Colonel, USAF
Chief, Development Division

ABSTRACT

A recent review of nuclear groundshock test data revealed oscillatory motions of undetermined origin, but of sufficient magnitude to be of concern in the design of shock isolation systems for underground protective structures. Response spectra of the oscillations exhibited amplification ratios far exceeding those employed in most groundshock prediction methods, the ratios being functions of the number of oscillations, and the amplitude and period of each cycle. As the source of the oscillations was not identified, there was no rational basis for relating these waveform parameters to such basic site and weapon conditions as yield, range, geologic structure and properties of the medium. In this investigation, two possible sources of the oscillatory motion are examined. First, the propagation of waves in a stratified site are studied and their directions and phase relationships estimated by use of wavefront diagrams and time-distance curves. Second, the form and strength of Rayleigh waves in an elastic, homogeneous half-space which result from surface pressure distributions similar to those generated by nuclear bursts were calculated. In both cases, oscillatory phenomena can be predicted and certain features related to the observed oscillations. However, the simple approaches employed in this analysis will not yield realistic wave strengths and thus, the composite waveform at a point in the half-space cannot be determined quantitatively.

(DISTRIBUTION LIMITATION STATEMENT NO. 2)

This page intentionally left blank.

CONTENTS

LIST OF ILLUSTRATIONS

LIST OF TABLES

SYMBOLS

a = wavefront velocity coefficient for cylindrical loading

a_1 = angle of incidence

a_1 = wavefront velocity coefficient for ring loading

B_r = integration path for inverse Laplace transform

c = shear wave velocity

c_p = dilatational wave velocity

c_r = Rayleigh wave velocity

d = horizontal radial coordinate of cylindrical loading wavefront from epicenter

d_1 = horizontal radial coordinate of ring loading wavefront from epicenter

d_r = width of parabolic ring loading

h = depth of earth layer

$H(x)$ = Heaviside function

i = angle of incidence

I_1, I_2 = transforms of K_1, K_2

$J_o(\xi, r)$ = Bessel function of zero order of (ξ, r)

K_1, K_2 = Inverse transforms of I_1, I_2

ℓ = dimensionless location of site = z/r

$\bar{L}_r$ = longitudinal wave energy flux reflection ratio

$\bar{L}_t$ = longitudinal wave energy flux transmission ratio

p = Laplace transform parameter

p_o = pressure for cylindrical loading

p_1 = peak pressure for parabolic ring loading

P_o = product of total cylindrical load and cylinder diameter = $S_o d$

q = radial displacement of ground

$\bar{q}$ = Laplace transform of q

Q = Laplace-Hankel transform of q

r = horizontal radial coordinate of a station from epicenter

r = angle of refraction

S = total force on ground exerted by blast pressure

S_o = force on ground due to cylindrical loading

S_1 = force on ground due to ring loading

t = time

$\bar{T}_r$ = transverse wave energy flux reflection ratio

$\bar{T}_t$ = transverse wave energy flux transmission ratio

u = vertical velocity of ground due directly to overpressure

v = velocity of wavefront

V_i = wave propagation velocity in Layer i

w = vertical component of ground displacement

$\bar{w}$ = Laplace transform of w

W = Laplace-Hankel transform of w

x = ground range

x = transformation variable

z = depth of station from surface of ground

α = "Softness" or range parameter for shallow sites = $a\gamma^2/cr$

α_1 = "Softness" or range parameter for deep sites = a/cz

α_{so} = parameter α corresponding to cylindrical loading

α_{s1} = parameter α corresponding to ring loading

β = definite integral variable

γ = ratio of shear wave velocity to Rayleigh wave velocity

$\delta(x)$ = delta function
η = dimensionless velocity coordinate
μ = shear modulus of medium
ν = Poisson's ratio
ξ = Hankel transform parameter
ρ = mass density of medium
σ = normal pressure exerted on ground by blast wave
$\bar{\sigma}$ = Laplace transform of σ
σ_{zz} = stress component in vertical direction
σ_{zr} = stress component in radial direction
Σ = Laplace-Hankel transform of σ
τ = dimensionless time = ct/r
τ_1 = dimensionless time = ct/z
ϕ = dilatational potential
$\bar{\phi}$ = Laplace transform of ϕ
Φ = Laplace-Hankel transform of ϕ
ψ = shear potential
$\bar{\psi}$ = Laplace transform of ψ
Ψ = Laplace-Hankel transform of ψ

1. INTRODUCTION.

A. Background. For the past several years, considerable attention has been focused on various aspects of the design of shock isolation systems for use in underground protective structures. A better definition of the groundshock, of course, has been the goal of numerous studies of weapons effects, both from the theoretical approach and from continued efforts to extract more detailed information from the limited number of nuclear test data. Between the free field ground motion and the input to the shock isolation system lies a capsule or other enclosing structure, and its dynamic response to the groundshock defines the nature and strength of the shock from which equipment and personnel must be protected. Here again, both theory and experiment are being employed to evaluate the interactions and to formulate design procedures.

The analysis of the shock isolation system itself as an elastically supported rigid body having six degrees-of-freedom has been the subject of innumerable studies; although, in fact, methods for treating such problems, both linear and nonlinear have been well established for some time. In this case the objective has been more one of familiarizing the designer with available techniques than of developing new ones. Similarly, the feasibility of a wide variety of shock isolation devices, generally based on adaptations of existing principles, has been investigated and various systems have been proposed as offering unique advantages.

With the accumulation of a sizeable fund of operating and test experience, and here, of course, "operating" implies static operation and not exposure to the design shock, more detailed requirements have been encountered and reported in the literature. Such considerations, for example, include compensation for load changes, maintenance techniques which can be employed without sacrificing hardness level, significance of manufacturing tolerances on performance, evaluations of the magnitude of air loads acting on the structure due to its motion relative to the capsule, effects of flexibility of the supported structure and the transmission of high-frequency accelerations through the mechanical elements of the isolator.

Concept studies of advanced facilities have also contributed to the recognition of problems relating to the design of current as well as future shock isolation systems and have stimulated the investigation of exotic designs. By extrapolating current designs to very large or very hard installations, weaknesses in the designs and the design procedures now employed frequently have become apparent.

When each of these problem areas is examined in detail and it is ascertained whether engineering information or engineering knowledge is needed, it appears to be clear that almost all of the problems fall in the former category. It is not implied that the design of shock isolation systems for this application has been reduced to pure routine and that no further developmental or research effort is warranted. It is believed, however, that if performance criteria are established completely and quantitatively prior to design, and if a development program is conducted in accordance with the high standards practiced in equally important engineering undertakings, most of the problems noted above could be resolved with a high level of confidence.

The outstanding exception is with those elements of the isolation system which are sensitive to aspects of the input which cannot be evaluated with the needed accuracy by any known weapons effects prediction method. For example, certain features of the time history of the shock must be known in order to determine the dynamic responses of nonlinear or rheolinear elements or systems. Even with coupled or highly damped linear systems, accurate calculation of the peak responses requires some information on the nature of the waveform, and, to evaluate the frequency content of the output, the input disturbance must be known as a function of time. While a number of structural elements and a few shock isolation systems may be approximated with acceptable accuracy as single degree-of-freedom, lightly damped oscillators, a most significant percentage cannot. Thus, the identification of input waveform parameters which can influence the responses of systems typical of those employed in underground protective structures appears to be the most important single research problem remaining to be resolved.

It is possible through the judicious selection of suspension kinematics and isolator characteristics to minimize this dependence of isolation system response on the less predictable features of the input waveform. Indeed, to ensure that the highest level of confidence in the ability of the system to perform as expected is achieved, practical designs should begin with insensitivity as one of the stated design objectives. By assigning levels of confidence to each of the predicted parameters of the shock input and by relating the various responses or the system to these parameters, the direction in which optimization should proceed becomes clearly evident.

However, confidence level is not the only criterion of performance, and other design goals render it rarely possible to achieve the degree of uncoupling of response from input which the uncertainty surrounding the details of the input would appear to warrant. Thus while a strong effort should be made in every case to reduce the sensitivity of the system to a minimum consistent with the other performance objectives, the design of most practical systems will require more information concerning the input than that afforded by current groundshock prediction techniques.

Until recently, the only information describing the nature of the shock environment which was specified as a basis for the design of shock isolation systems was a frequency spectrum of the envelope of the responses of linear, undamped systems. These spectra were formulated by groundshock prediction methods based on tests conducted at the Nevada Test Site and the Eniwetok Proving Ground. Both waveforms and spectra were obtained during the tests. However only gross characteristic features of the waveforms could be identified; thus, except for a limited number of parameters, the prediction methods were directed toward the synthesis of response spectra rather than of time histories. Further, the geologic formations at the test sites were not typical of those at which most underground protective structures are constructed, nor were the weapon sizes of the magnitude of those now being considered. In addition, insufficient site and weapon parameters could be varied during the tests to evaluate independently the effects of each. Therefore, to extrapolate these data to other site and weapon conditions of interest, simple linear, one-dimensional relationships were used extensively.

As a means for estimating the gross strength of the shock which might be expected to occur under specified conditions, these prediction methods have been of vital importance to the protective structure program. Indeed without them, it is unlikely that the design of structures of significant hardness would have been attempted. Thus these prediction techniques, crude as they may be, have played an invaluable role in the construction of all hardened facilities in the United States.

However, to utilize the limited information available on the nature of the groundshock, early analyses of shock isolation systems and other structural components of protective facilities employed, of necessity, many simplifying assumptions. In most cases the systems were regarded as being linear and where time histories of the input were essential, any pulse whose response spectrum matched or exceeded the design spectrum in the frequency range of interest was accepted as a suitable representation. However as the intended hardness level of each new facility increased, the requirements for an ever greater reliability and a more nearly optimum design rose correspondingly. Analyses became more rigorous and now have been extended to many elements formerly treated only by gross approximation. In almost every case the greater emphasis on rigor in design analysis has demanded a more accurate and detailed definition of the shock environment.

For the most part, current weapons effects prediction methods consider two basic groundshock pulse shapes, the airblast-induced pulse and the direct-induced pulse. Procedures are given for calculating the peak motions for each type of pulse and, together with suitable amplification ratios, these peak values are used as a basis for constructing response spectra. Some guidance is provided for estimating certain other parameters of their waveforms such as acceleration rise time, positive velocity duration, and total pulse duration. The confidence level in the predictions of these latter parameters however is usually considered to be far less than those of the peak motions.

To account for the effects of all other ground motions generated by the nuclear burst, and in particular of the reflections and refractions from the various layers of stratified media, the usual practice is to increase the peak airblast-induced motions by a factor which is related to the range of the point of interest and the range at which outrunning first occurs. While this method may yield acceptable values for the peak ground motions, it gives no indication of the detailed nature of the waveform other than to describe it as a "random oscillation." As a great many facilities of interest are constructed at highly stratified sites the problem of defining time histories of the groundshock is an important one.

In the design of the shock isolation system for the Launch Control Center of the Minuteman Weapon System, the combined requirements for attenuation and rattlespace were impossible to satisfy with a linear system, and as only a response spectrum was provided to define the shock, the engineering contractor was faced with the responsibility for synthesizing waveforms which could be employed to verify the performance of the nonlinear system he had selected. Considerable discussion then centered about the validity of the waveforms he had constructed and there always remained some question that the most critical conditions had been represented.

Partially on the basis of this experience, the Air Force Special Weapons Center in 1961 initiated several studies directed toward the formulation of design methods applicable to nonlinear shock isolation systems for use in underground protective structures. In one of these (1), all available waveform data from nuclear tests were re-examined with the objective of identifying all characteristic features of the waves which might be of significance to the responses of low frequency systems. It was found that when the contribution of the direct airblast-induced motion was removed from certain test records, there remained a low frequency oscillation of sufficient strength to be of vital concern in the design of linear as well as nonlinear shock isolation systems. Although the oscillation could not be traced directly to its source, it was suggested that it resulted from refractions returning to the surface from underlying layers having higher seismic velocities. This hypothesis appeared to correlate well with the fact that in the test data, the oscillation was most apparent in the trans-seismic range where the refractions would be expected to contribute a large percentage to the total ground motion.

To explore further the possible source of such an oscillation the present investigation was undertaken. Other research projects now in progress are studying the general problem of the transmission of waves through homogeneous and layered, elastic and inelastic media. This effort, however, was concerned solely with those aspects of groundshock phenomena which might shed some light on the source and strength of the observed oscillations.

The problem of identifying possible sources of the waves was approached by two distinctly different methods. First, the wavefront diagram was employed to determine whether or not the oscillations appeared to be simple combinations of airblast-induced, direct-induced, reflected and refracted waves impinging at a point in some sequence defined by the geology of the site. The wavefront diagram is a graphical representation in a vertical plane of a wavefront as it propagates outward from a point source, and although inelastic media and arbitrary stratification of the site can be considered, it is evident that the method is strictly limited in its ability to portray faithfully all wave phenomena emanating from a nuclear explosion. Nonetheless, as noted earlier, the objective here was only to establish the phase relationships and if possible the relative strengths of the four types of waves/and, in this respect, the wavefront diagram appeared to offer some promise.

In the second approach, the contribution to the oscillatory motion of surface waves were investigated theoretically. Again, however, only forms and the relative magnitudes of such waves need be ascertained to class them as likely relatives of those observed in the test data. Thus, this effort also was conducted without the degree of detail considered necessary in a more rigorous analysis of groundshock wave propagation. In particular, the form and strengths of Rayleigh waves generated in an elastic, homogeneous half-space by a surface pressure distribution similar to that resulting from a nuclear burst were calculated and their phasing with other waves emanating from the source estimated. They were then compared with the observed oscillatory motions and points of similarity noted.

B. Observed Oscillatory Groundshock. Sauer (1, 25) was the first to attempt to synthesize the general characteristics of the strong velocity oscillations observed in several groundshock waveforms integrated from acceleration records obtained during nuclear weapon tests. While high-frequency oscillatory phenomena, of course, are frequently found in acceleration traces of this type, they can usually be expected to have little influence on the velocity curve. In this case, the relatively low frequency of the velocity oscillations together with their significant strength and apparent regularity of form lead to the hypothesis that they resulted from some undetermined but not unusual interaction of the various groundshock components.

The oscillations were observed in data taken both at the Eniwetok Proving Ground (EPG) and at the Nevada Test Site (NTS). To isolate the oscillation, the essentially regular one-sided velocity waveform commonly associated with the superseismic airblast-induced groundshock, designated as a Type I wave and shown in Figure 1, was subtracted from outrunning Operation Tumbler data and compared with data from Koa 12 where the Type I was, presumably, filtered out by the ground. The relative amplitudes of the various peaks were averaged over these data as were the relative time durations of the cycles. More weight was given to the Koa data since the yield for this shot was in the megaton range. After the first tentative velocity curve had been constructed it was integrated to give the displacement and adjustments were made in the later portions of the velocity curve so that the residual displacement would be zero.

The resulting oscillation, designated as a Type II wave, is shown in Figure 2 and is compared in Figures 3 and 4 with several traces obtained at Koa. In some cases the normalized curve fits the data very well; in others, the fit is not so good, but the normalized curve still has the general shape of the measured motions. Sauer suggests that the oscillation is related in some fashion to the outrunning condition and illustrates the development of outrunning waveforms obtained during Operation Tumbler, Shot No. 1, by appropriate combinations of Type I and Type II waveforms (25).

In reviewing the test data, Sauer noted that no characteristic features could be identified in the acceleration records. It seems reasonable however that if the Type II oscillation is the interaction of several waves reaching the point of interest by different routes and at different times, the arrival of each wave should be indicated by a fairly abrupt change in acceleration. It is possible, though, that the number of waves resulting from the disturbance in a highly stratified, nonlinear medium was so large that their identity was lost.

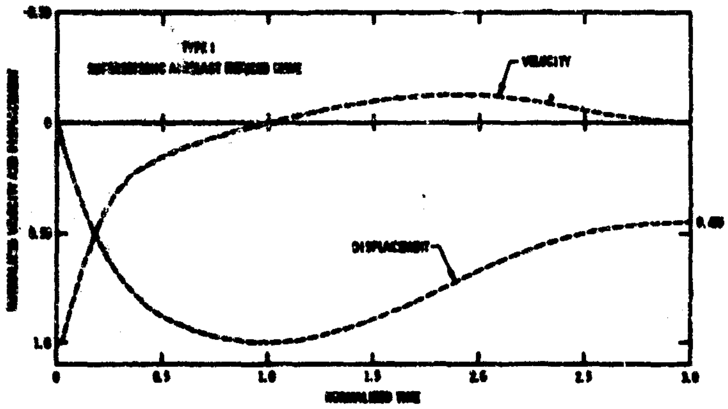

Figure 1. Type I (Superseismic Airblast) Normalized Vertical Particle Velocity and Displacement Waveforms.

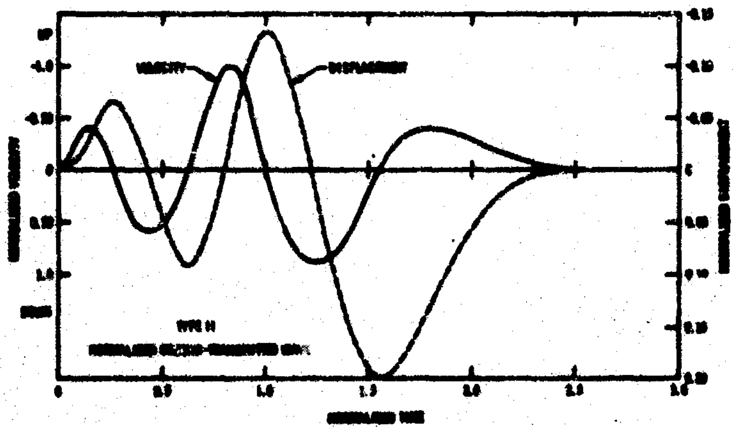

Figure 2. Type II (Outrunning Ground Motion) Normalized Vertical Particle Velocity and Displacement Waveforms.

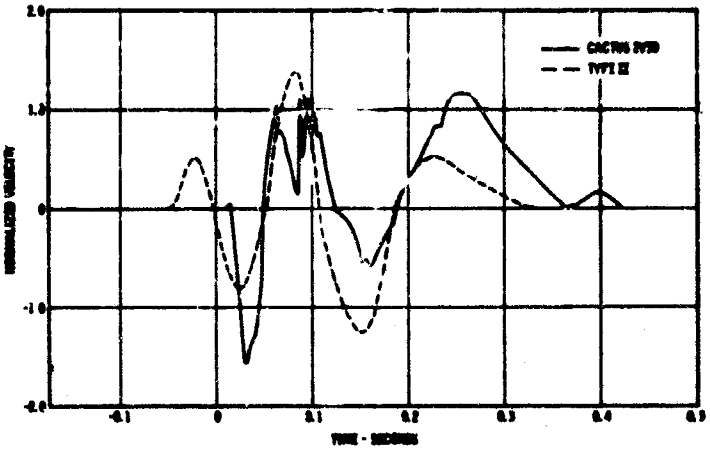

Figure 3. Comparison of the Type II Vertical Velocity Waveform with Data from Shot Cactus, Gage 2V30, 650 Foot Range, 30 Foot Depth.

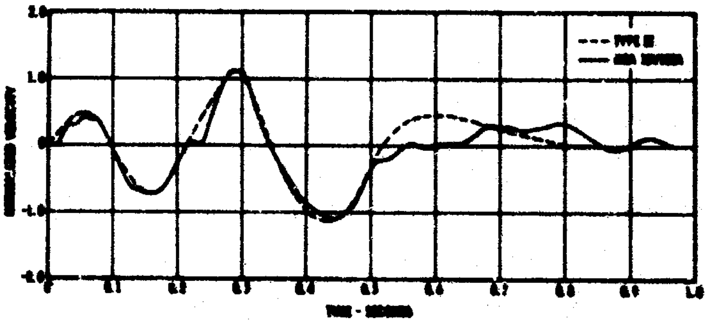

Figure 4. Comparison of the Type II Vertical Velocity Waveform with Data from Shot Koa, Gage 12V100A, 3,144 Foot Range, 100 Foot Depth.

Nonetheless it was believed to be sufficiently promising to investigate the possibility of constructing a reasonably close approximation of the shape of the Type II component by employing information obtained from the simple wavefront and time-distance diagrams together with the few data provided by the groundshock prediction methods. Although many simplifications would be required, it was hoped that the most important phenomena could be considered and that the resulting waveform would be a significant improvement over the arbitrarily selected shapes previously employed in shock isolation system analyses.

2.0 WAVEFRONT DIAGRAM.

A. Background. Calculation of the transmission of energy from an air or surface burst of a nuclear weapon to a given point on or in the ground is an exceedingly difficult task, even for sites whose geologic structure is relatively uniform. While several investigators have formulated computer programs to calculate the ground motions in inelastic, layered media, to date no computer solutions have provided time histories of the ground motion suitable for design purposes.

On the other hand, accepted weapons effects prediction methods yield little more than maximum motions of the ground resulting from a single wave. Simple pulse type waveforms are suggested for airblast-induced and direct-induced waves, but no guidance is given for predicting waveforms which might result by the impingement at a point of several waves of different magnitudes, from different directions and at phase intervals related to the specific site under consideration. Almost all of these works have been directed toward the synthesis of response spectra of the groundshock, not a waveform, and thus their direct applicability to shock isolation system design has been limited to linear systems whose equations of motion contain only constant coefficients.

As a means for better visualizing the modes of propagation of the shock through the ground, the designer may employ a wavefront diagram. The wavefront diagram is simply a representation of a vertical plane passing through the point of weapon burst and the site of interest on which the position of the wavefront is shown at discrete time intervals. Any number of layers can be shown and oriented in whatever fashion the designer believes to be most representative of the actual site. The degree of detail that can be included in the wavefront diagram is limited primarily by the patience and resourcefulness of the designer, but in most instances the assumptions of elastic, homogeneous, isotropic layers with sharp interfaces have been employed.

Data obtainable from a wavefront diagram are primarily the arrival time of a wave at the point of interest, the path by which the wave reached the point and the initial direction of propagation of the wavefront. If the assumption of a linear medium either with or without layering is reasonably valid, these data can be determined for all waves generated directly by the source or by the moving airblast wavefront. In most cases of interest however the medium is not linear even at ranges extending beyond the rupture zone and thus the velocity of propagation of each wave at each instant is dependent on the local time-stress history of the medium. Even if the nonlinear stress-strain characteristic of the medium is known, the strength of the waves cannot be determined from the wavefront diagram and thus the propagation velocity of waves of finite strength can only be approximated.

The first objective of this phase of the work then was to compare computed arrival times of various waves for site and weapon conditions corresponding to those prevailing at selected nuclear tests with the measured arrival times in order to determine the degree of error involved in the assumption of a linear medium. For a solution of the second problem, that is the estimation of the time of arrival and the magnitude of the peak motions of each wave, the wavefront and the time-distance diagrams, of course, provide little useful data.

B. The Use of the Wavefront Diagram in Ground Motion Problems. The basis and procedure for constructing wavefront diagrams and accompanying time-distance curves of the refracted and reflected waves and methods of using these diagrams with the airblast curve to compute the time of arrival of the first wave are presented in this section. The methods are then applied to test shots made during Operation Tumbler and Shot Priscilla of Operation Plumbbob. Seismic velocities measured during a conventional seismic survey are compared with the velocities measured during the test shots for the purpose of determining the effect of nonlinearity of the soil and establishing a basis for computing the time of arrival of waves subsequent to the first. Finally, the distribution of energy at the interface of two elastic layers is examined to determine the relative proportions of energy carried by the reflected and refracted waves.

(1) The Wavefront Diagram. Wavefront diagrams were developed as a tool in seismic prospecting to obtain a better "feel" for the interpretation of the time-distance graphs obtained from refraction seismic surveys. Examples of the use of wavefront diagrams appeared in the literature as early as 1950, (2). Wavefront diagrams provide a visual method for evaluating both qualitatively and, with regard to time and distance, quantitatively the nature of the motion of the ground when a source of energy is applied at a point on the surface.

(A) Basis. A typical wavefront diagram is presented in Figure 5. The diagram is simply a composite, planar, vertical cross-section of the ground showing the positions of the wavefront emanating from a point source at specific time intervals. At any given time the wavefront is a curved surface passing through the most advanced positions reached by the disturbance at that time.

To construct a wavefront diagram, it is convenient, although not essential, to assume that the wave velocity in each layer or zone is constant. To compute arrival times no assumption is necessary regarding the character of the disturbance. The boundaries of the various layers or zones may be irregular, or oriented in any direction, and the wave propagation velocity can be allowed to change in small or large steps, and in either or both the vertical or horizontal directions.

For any arrangement of layers with different wave velocities, the entire net can be constructed using Huygen's principle: every point on a wavefront acts as though it were itself a center of disturbance, sending out wavelets of its own, always away from the source, the collective effect of which constitutes a new wavefront. For complex profiles, it is usually easier to construct the wavefront diagram using just the basic principle of Huygen; however, for regular profiles, construction can be speeded by certain other aids. A detailed step-by-step example of the construction of a wavefront diagram is given in Appendix A.

(B) Character. All of the wavefronts shown in Figure 5 are not just simple spherical waves emanating from a point, but may be composed of several wavefronts of different origin and history. For example, the wavefront at a time equaling 3.0 seconds consists of a combination of four simple wavefronts. The section of the front traveling in Layer 1 is the "first underlayer wave" which has arrived at that position by being refracted along the top of Layer 2 (first underlayer) and back into Layer 1. The part of the front between the top of Layer 2 and the curve BGN is the refracted wave traveling through the body of Layer 2. The remaining part of the front in Layer 2 has been refracted into Layer 3 and back into Layer 2. This is called the "second underlayer wave." The part of the front in Layer 3 is the refracted wave traveling through the body of that layer.

Due to the higher velocity of Layer 2 compared to Layer 1, the area to the right of Point A in Figure 5 is first reached and set in motion by the refracted wave traveling in and along the top of Layer 2, not by the direct wave from Point S. The angle which the underlayer wave makes with the boundary at which it originates is independent of the position of the original source or the formation thickness and depends only on the velocity ratio of the two formations adjoining the boundary.

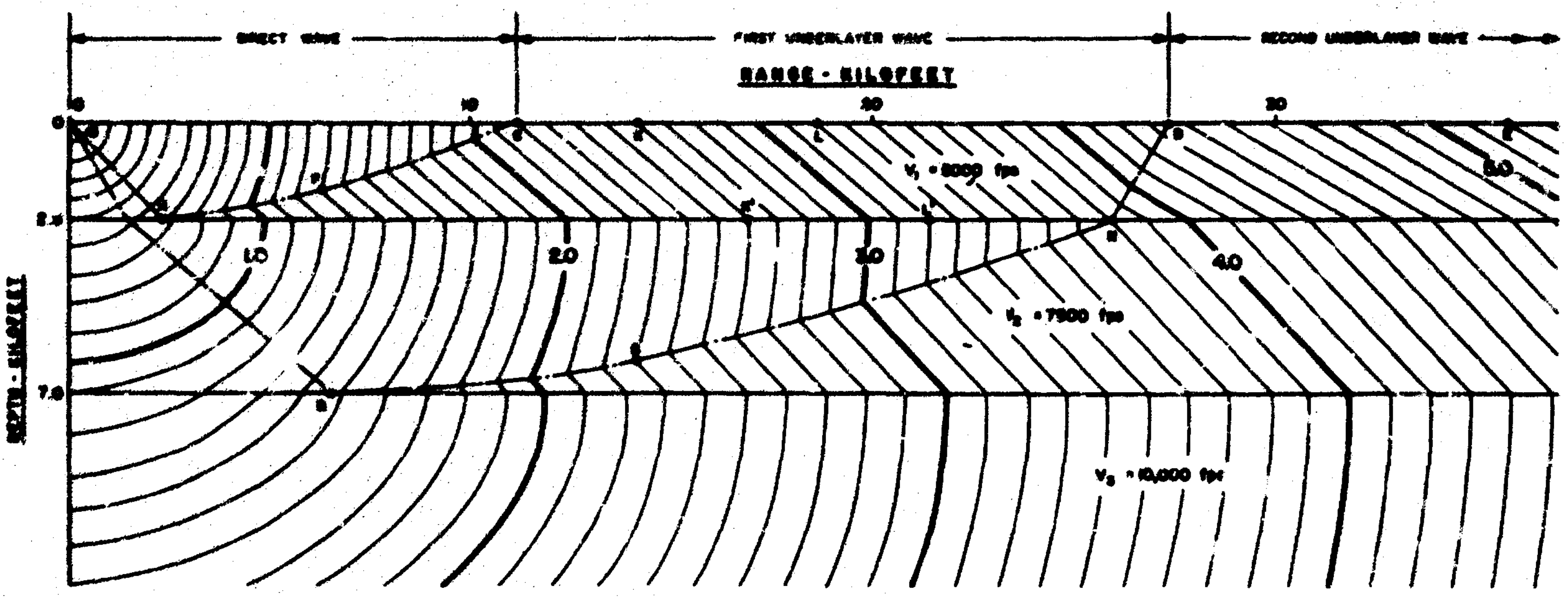

Figure 5. Wavefront Diagram

If Layer 2 had a velocity lower than that of Layer 1, the direct waves in Layer 1 would be refracted downward into Layer 2 and no "underlayer wave" would be generated. Only for those boundaries at which the velocity increases with depth will underlayer waves be generated.

Along the top of Layer 2, the wavefronts to the right of Point A appear to have originated at Point A. The same condition exists to the right of Point B in Layer 3. At both Points A and B, total reflection from a source at S would occur, according to Snell's Law.

(C) Snell's Law. The refraction of waves at the layer interfaces is governed by Snell's Law. This law was discovered experimentally, but it actually is consequence of Fermat's principle which states that rays travel along such lines that the optical distance between any two points of the rays is a minimum. If the given point is in a medium characterized by a velocity different from the medium containing the second point, then the ray path between these two points will not be a straight line.

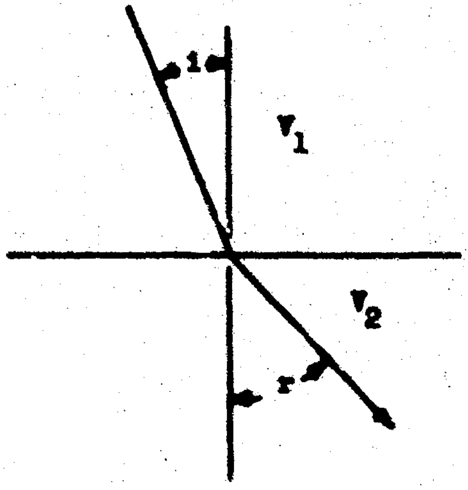

Figure 6. Angles of Incidence and Refraction

Snell's law of refraction states that refraction or bending of the ray path occurs when crossing a boundary between layers of different velocities such that, referring to Figure 6,

$$\frac{\sin i}{\sin r} = \frac{V_1}{V_2} \tag{1}$$

or, for any one ray path,

$$\frac{\sin i}{V} = \text{constant.} \tag{2}$$

When a ray in a lower velocity medium strikes an interface with a higher velocity medium, there is a certain critical angle of incidence designated as i_c, for which the angle of refraction r is 90 degrees and the refracted wave is parallel to the surface of discontinuity. Since, in this case, sin r = 1, it is evident from Snell's law that

$$\sin i_c = \frac{V_1}{V_2} \tag{3}$$

For any angle of incidence greater than i_c, there can be no refracted ray in the second medium and, therefore, no penetration into that medium, all the energy incident at such an angle being reflected. Thus, for incident angles greater than the critical angle there is total reflection.

Points A and B, in Figure 5, represent the location of a ray path from Point S at the critical angle. The wave refractions which occur to the left of Points A and B do not return to the surface. The fact that Points A and B can be located by Snell's law and represent the minimum time paths is of considerable assistance in the graphical construction of a wavefront diagram.

(D) Coincident-Time Curves. Curves represented by points ARC and BGHD of Figure 5 are formed wherever two different wavefront systems intersect. Together with the layer boundaries, these curves divide the section into zones, each zone containing wavefronts of a common origin. By construction, all points on such a curve are equally distant in time from the source along two different paths. Therefore, such lines are called coincident-time curves.

(E) Later Arrivals. The wavefronts shown in Figure 5 are only those arriving first at each point. The direct wave shown as the first arrival to the left of line AFC in Figure 5 will continue arriving later at points C, K, L, D, E, etc. However, this wave will reach these points after the arrival of waves traveling by other paths. The same is true with the first underlayer wave where it is no longer a first arrival to the right line of MD. Reflections, which are never a first arrival, will also arrive later at all points along the ground surface. In addition, the reflections will occur at the interface between Layer 1 and Layer 2, and also between Layer 2 and Layer 3.

Since shear waves travel at a velocity of about one-half that of longitudinal waves, they do not appear in a first arrival wavefront diagram. Shear waves will be generated whenever a longitudinal wave strikes a discontinuity where there is a change of elastic properties. In fact, four new waves will be set up in this situation. For example, Figure 7 shows an incident longitudinal wave P and the resulting reflected longitudinal wave PP_1, reflected transverse wave PS_1, refracted longitudinal wave PP_2, and refracted transverse wave PS_2. (The arrows parallel to the rays (⟶) indicate longitudinal waves; those perpendicular to the rays (—┼→) indicate transverse waves.) A similar set of four waves (but at different angles) would be set up if the incident wave were transverse.

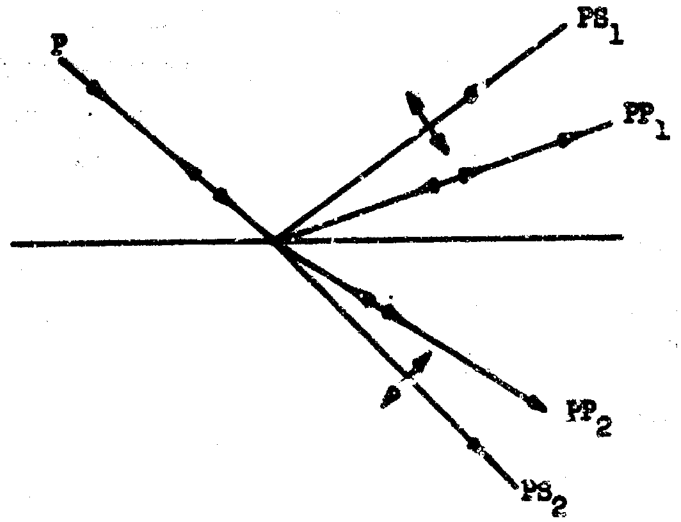

Figure 7. Reflected and Refracted Transverse and Longitudinal Waves due to an Incident Longitudinal Wave.

The division of energy between the different waves depends on the velocities and the densities of the two media (i.e., $V_{1}\rho_{1}$ and $V_{2}\rho_{2}$) and on the angle between the incident wave and the surface of discontinuity. The energy division between the various waves will be discussed in a later section. In general, for simple reflection, the proportion of reflected energy will be greater for greater differences in the elastic properties on the two sides of the discontinuity.

In seismic prospecting, concern is always with the fastest waves and, therefore, with incident longitudinal waves P, reflected longitudinal waves PP_1, and refracted longitudinal waves PP_2. At the present stage of development of seismic prospecting, little use is made of the shear waves. Occasionally, however, special purpose surveys are run to measure the shear wave velocity to provide data to calculate the elastic properties of a material, such as Poisson's ratio, (3).

The later arrivals can be shown on a wavefront diagram, but their presentation becomes very cumbersome. They are more easily presented on time-distance curves, which will be discussed in the following section. An example of a reflection wavefront diagram is shown in Figure 28.

(2) Time-Distance Curves. Time-distance curves may be constructed from data obtained from a seismic survey. In general, a particular survey will consist of measurements of either the refracted and direct waves or the reflected waves. The time of arrival of the wave is determined from inspection and correlation of the seismogram from each geophone, or record of motion vs. time. The location of each geophone in relation to the disturbance or "shot" is known. The most common type of seismic survey used for site evaluation for civil engineering purposes is the refraction survey; however, the reflection survey is the most common in petroleum or other deep studies. It will be shown later that a reflection survey would also be of significant value in the evaluation of ground motions due to nuclear blast.

The value in this application of the time-distance curves lies in the ease with which the sequence of arrival times, including the first and later arrivals, at any point of interest can be identified.

The direction of motion at the point of interest cannot be determined from the time-distance curves and requires either the construction of a wavefront diagram or a construction for the particular wave in question.

For interest, the time-distance curve derived from Figure 5 is presented in Figure 8. Additional time-distance curves for the test sites at Frenchman Flats and T-7 (Yucca Flats) in the Nevada Proving Grounds are shown in Figure 24 and Figures 26 through 28.

(A) **Basis.** Figure 9 represents a subsurface section consisting of two horizontal layers which are assumed to be isotropic and nearly homogeneous, having nominal longitudinal wave velocities V_1 and V_2 in the upper and lower layers respectively. Assume also that velocities V_1 and V_2 increase slightly with depth, but are sufficiently different so that there is an abrupt discontinuity in seismic velocity at the interface MN'. Point 0 represents the source of disturbance and S, a seismometer station located at distance x from 0.

Following the explosion at 0, surface waves and three types of longitudinal waves, direct, reflected, and refracted, are received at S, provided that x is sufficiently great. The direct wave travels along the surface, following path OS; the reflected wave follows the path OBS; and the refracted wave follows the path OACS. The time-distance curves for the three longitudinal waves may be determined as follows.

The length of the curved path OS is approximately equal to x, the slight curvature being due solely to the increase of velocity with depth. Hence, the time, t, required by the direct wave to traverse the distance OS ≈ x is

$$t = \frac{x}{V_1} \text{ and } x = tV_1 \qquad (4)$$

The position of the wavefront on the time-distance curve (Figure 10) therefore is a straight line which passes through the origin and has a slope of magnitude $1/V_1$.

From the geometry of Figure 9, it is seen that the distance from the point point 0 to the point of reflection B is

$$OB = \sqrt{\left(\frac{x}{2}\right)^2 + h^2} = \frac{1}{2}\sqrt{x^2 + 4h^2}$$

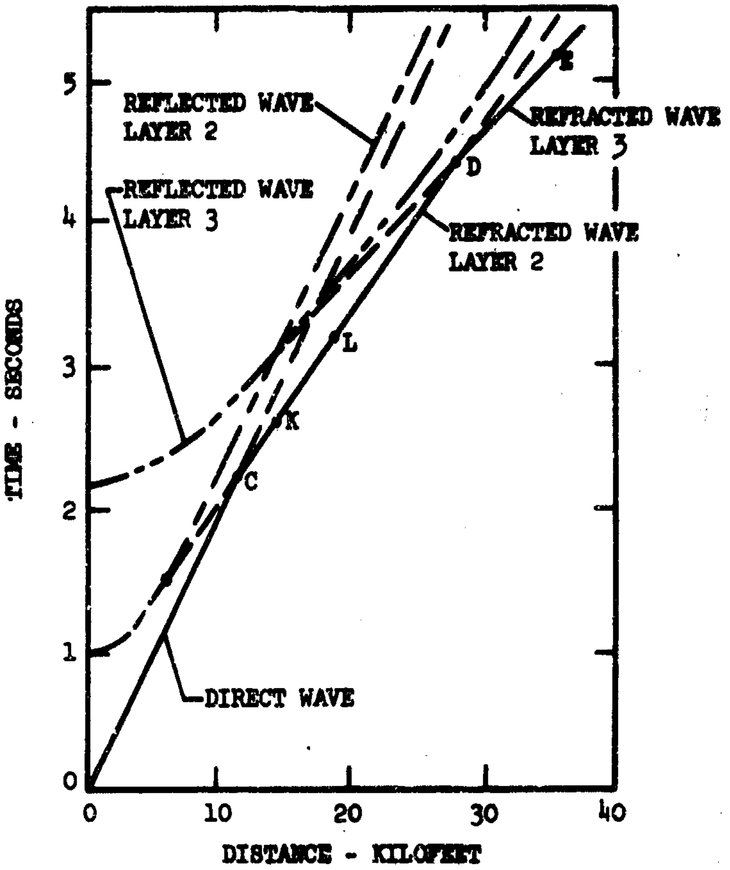

Figure 8. Time-Distance Curves for Wavefront Diagram of Figure 5.

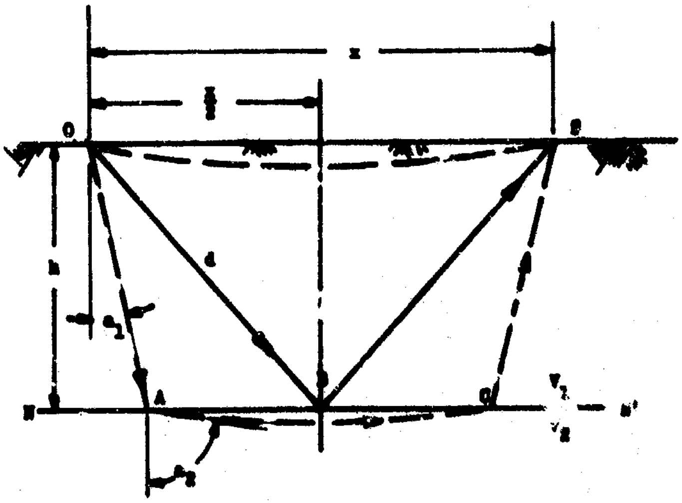

Figure 9. Ray Paths in a Two Layer System.

When the interface between Layer 1 and Layer 2 is parallel to the surface, a condition of symmetry exists and the distance $\overline{OB} = \overline{BS}$. The total distance traveled by the reflected wave is then $\overline{OB} + \overline{BS}$.

$$\overline{OB} + \overline{BS} = \sqrt{x^2 + 4h^2}$$

Since the distance $(\overline{OB} + \overline{BS})$ is also equal to tV_1, the time for the reflected wave to travel distance x is,

$$t = \frac{\sqrt{x^2 + 4h^2}}{V_1} \tag{5}$$

This is the equation for a rectangular hyperbola, as plotted in Figure 10.

The time-distance curve of the wave which is refracted near the critical angle, and therefore travels in the lower layer along a path which is approximately parallel to the boundary, is obtained by adding the time-distance in the two layers. The time-distances in the upper and lower layers are $(OA + CS)/V_1$ and AC/V_2, respectively. It is evident from Figure 9 that $OA = CS = h/\cos a_1$; also, $AC = x - 2h \tan a_1$.

Hence, the time for the refracted wave to travel path OACS is

$$t = \frac{2h}{V_1 \cos a_1} + \frac{x - 2h \tan a_1}{V_2} \tag{6}$$

Equation 6 may be simplified by replacing the trigonometric functions by their equivalents in terms of the velocities. It follows from Equation 3 that

$$\cos a_1 = \sqrt{1 - \left(\frac{V_1}{V_2}\right)^2}$$

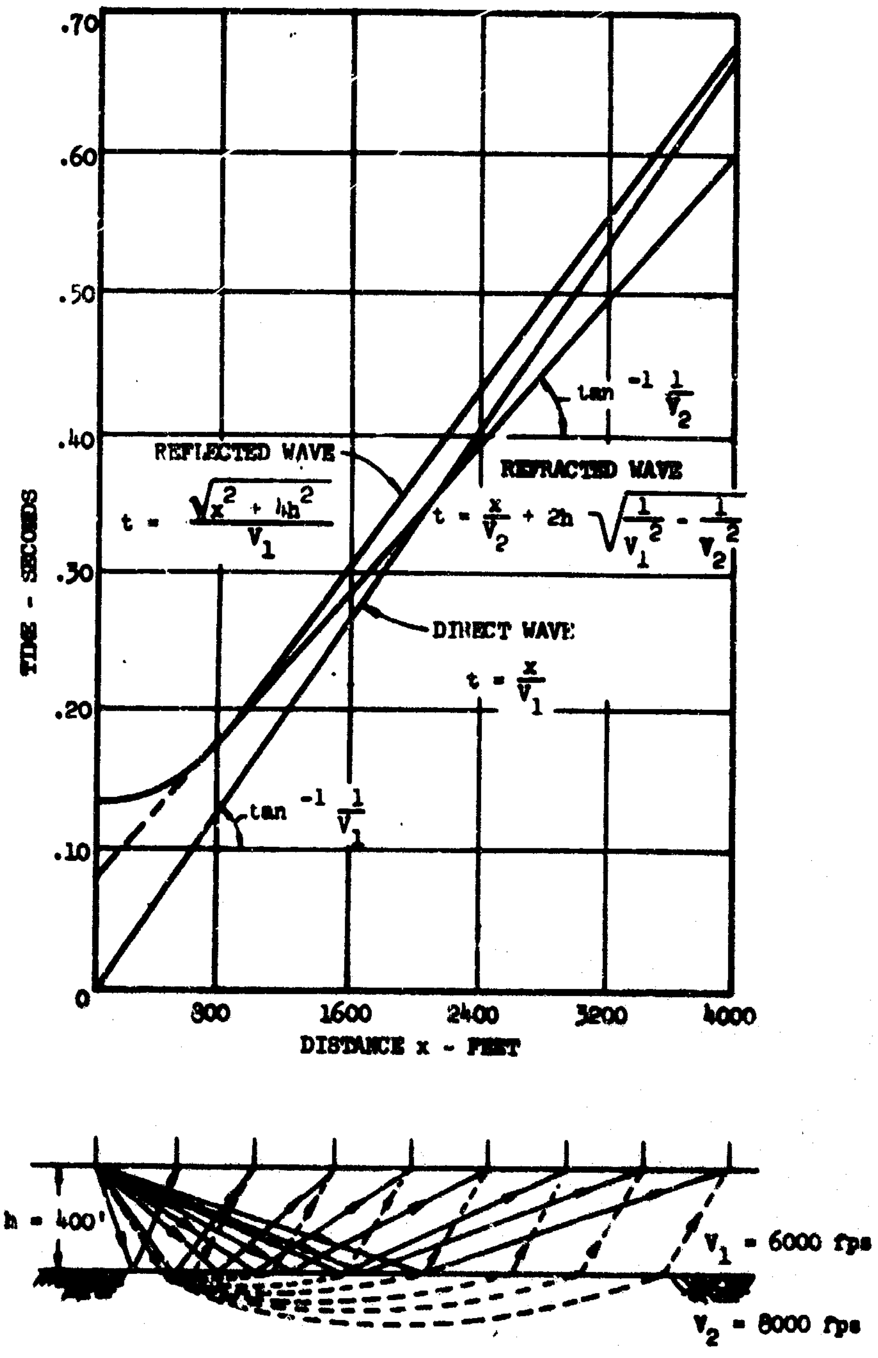

Figure 10. Typical Time-Distance Curves for a Two Layer System.

and

$$\tan a_1 = \sqrt{\frac{V_1^2}{V_2^2 - V_1^2}}$$

Hence,

$$t = 2h\sqrt{\frac{1}{V_1^2} - \frac{1}{V_2^2}} + \frac{x}{V_2} \qquad (7)$$

The time-distance curve for the refracted wave is therefore a straight line having a slope of magnitude $1/V_2$ (Figure 10).

The time-distance curve can also be used as a basis for calculating the depth, h, to a layer of a higher velocity. For the two layer case considered above it can be found that

$$h = \frac{x_c}{2}\sqrt{\frac{V_2 - V_1}{V_2 + V_1}} \qquad (8)$$

The critical distance x_c is the distance to the intersection of the curves for the direct wave and the refracted wave (beyond the range of Figure 10). This expression also indicates the horizontal distance from the source to the point where the first arrivals from the higher velocity layer first reach the ground surface.

In the usual case, the geologic section consists of more than two horizontal layers of thicknesses h_1, h_2, h_3, ... h_n of successively increasing velocities V_1, V_2, V_3, ... V_n as shown in Figure 11. The paths or rays penetrating to the various layers will be segments of straight lines, refracted at the interfaces according to Snell's law. The angle of the path taken by the minimum time ray to any interface can be found as follows (referring to Figure 11):

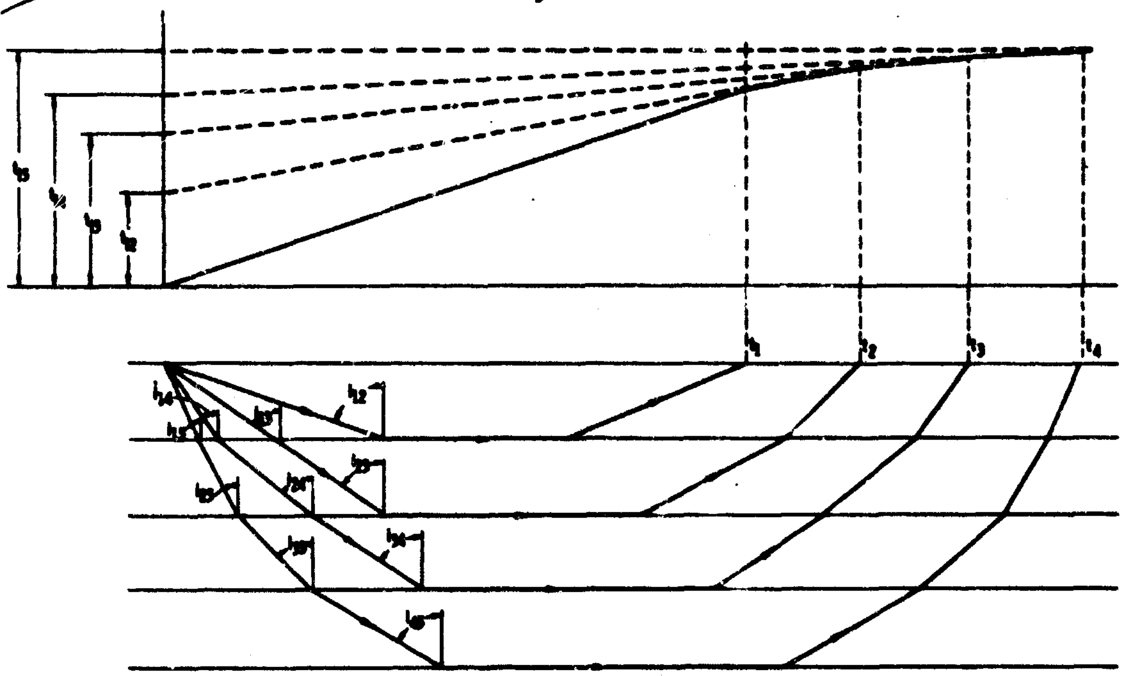

Figure 11. Minimum Time Paths for Multiple Layers.

$$\sin i_{12} = \frac{V_1}{V_2}$$

$$\frac{\sin i_{13}}{\sin i_{23}} = \frac{V_1}{V_2}\ ; \quad \text{but } \sin i_{23} = \frac{V_2}{V_3}\ ; \quad \therefore\ \sin i_{13} = \frac{V_1}{V_3}$$

$$\frac{\sin i_{14}}{\sin i_{24}} = \frac{V_1}{V_2}\ ; \quad \frac{\sin i_{24}}{\sin i_{34}} = \frac{V_2}{V_3}\ ; \quad \sin i_{34} = \frac{V_3}{V_4}$$

$$\sin i_{14} = \frac{V_1}{V_4}$$

and, in general,

$$\sin i_{mn} = \frac{V_m}{V_n} \qquad (9)$$

Thus, the angle of the minimum time path in any layer is determined by the velocity in that layer and in the fastest layer penetrated and is independent of the velocity in intermediate layers.

Using the minimum time paths given above, the equation for the time-distance curve for the refracted waves can be expressed in the following form:

$$t_n = \frac{x}{V_n} + \frac{2h_1\sqrt{V_n^2 - V_1^2}}{V_1V_n} + \frac{2h_2\sqrt{V_n^2 - V_2^2}}{V_2V_n} + \ldots + \frac{2h_{n-1}\sqrt{V_n^2 - V_{n-1}^2}}{V_{n-1}V_n} \qquad (10)$$

The intercept times shown on the top of Figure 11 can be written as

$$t_{in} = \frac{2h_1\sqrt{V_n^2 - V_1^2}}{V_1V_n} + \frac{2h_2\sqrt{V_n^2 - V_2^2}}{V_2V_n} + \ldots + \frac{2h_{n-1}\sqrt{V_n^2 - V_{n-1}^2}}{V_{n-1}V_n} \qquad (11)$$

Whenever coincident-time curves intersect the ground surface, there is an abrupt change in slope in the time-distance curve, indicating that at such points the first arrival is due to a different set of waves. As the slopes of curves of a single system are not discontinuous, the presence of such breaks in the curve is a signal that a change is taking place from one set of waves to another. Unfortunately, in practice it is not always possible to secure data sufficiently precise to detect such a break.

(3) <u>Partition of Energy in Reflected and Refracted Waves</u>. In the previous section, the leading compressional wavefront was traced from its source throughout the surrounding media, including adjacent layers. It was mentioned that in a similar manner the first arrivals of waves traveling longer paths could also be plotted, although the problem is complicated if the seismic velocity has been altered by the passage of earlier waves. It was also noted that the impingement of either a compressional or distortional wave on an interface separating media of different characteristics resulted in the generation of four new waves.

To gain some idea of the nature of the ground motion at a point, the contribution of all waves reaching that point must be evaluated. The waves reaching the point by direct passage through a single medium are usually assumed to decrease in strength with distance due to spatial dispersion. At the interfaces between layers, however, it is necessary to compare the distribution of energy among the reflections and refractions.

Equations describing the partition of energy between the reflected and refracted waves at an interface separating two media have been published by Knott (4) and are available in more recent literature (5). Numerical solutions of the equations for a wide range of density and velocity ratios were published by Muskat and Meres (6); by Ewing, Jardetsky, and Press (7); also by Howell (8). Because of their application to this study, some of the results of the work by Muskat and Meres is reproduced here. Selected results from their companion paper (9) are also presented.

(A) Energy Division. When a longitudinal wave impinges on a boundary separating layers of different elastic constants or densities, its energy will be distributed among four new waves, a longitudinal and a transverse wave in each layer. The division of energy among the different waves depends on the velocities and densities of the two layers and on the angle between the incident wave and the plane of the interface.

To illustrate the relative importance of the four waves, the division among them of the energy in the plane, longitudinal, incident wave is tabulated for one profile in Table 1. The ratio of the density of the medium in the lower layer to that in the upper layer is 1.1 and Poisson's ratio is assumed to be 0.25 for both media. The parameter "a" is the ratio of the seismic velocity in the lower layer to that of the upper layer.

The fractions of the incident longitudinal wave energy converted into energy in the reflected and transmitted longitudinal and transverse waves

Table 1

FRACTIONS OF THE INCIDENT ENERGY TRANSFORMED INTO LONGITUDINAL AND TRANSVERSE WAVES CREATED AT AN ELASTIC INTERFACE AFTER INCIDENCE OF A PLANE LONGITUDINAL WAVE (ℓ)

θ		a = 0.75	1.0	1.25	1.50	1.75	2.00
0°	$\bar{L}_r$	0.0092	0.0023	0.0249	0.0602	0.1001	0.1406
	$\bar{T}_r$	0	0	0	0	0	0
	$\bar{L}_t$	0.9908	0.9977	0.9751	0.9398	0.8998	0.8594
	$\bar{T}_t$	0	0	0	0	0	0
5°	$\bar{L}_r$	0.0090	0.0022	0.0243	0.0587	0.0975	0.1370
	$\bar{T}_r$	0.0002	0.0001	0.0005	0.0013	0.0023	0.0031
	$\bar{L}_t$	0.9905	0.9977	0.9748	0.9386	0.8972	0.8547
	$\bar{T}_t$	0.0004	0.0000	0.0004	0.0014	0.0030	0.0051
10°	$\bar{L}_r$	0.0083	0.0021	0.0227	0.0545	0.0904	0.1270
	$\bar{T}_r$	0.0008	0.0002	0.0021	0.0051	0.0084	0.0117
	$\bar{L}_t$	0.9895	0.9977	0.9736	0.9347	0.8890	0.8407
	$\bar{T}_t$	0.0014	0.0000	0.0015	0.0057	0.0122	0.0206
15°	$\bar{L}_r$	0.0072	0.0019	0.0201	0.0484	0.0803	0.1130
	$\bar{T}_r$	0.0017	0.0004	0.0043	0.0103	0.0168	0.0229
	$\bar{L}_t$	0.9879	0.9977	0.9721	0.9283	0.8753	0.8174
	$\bar{T}_t$	0.0032	0.0000	0.0035	0.0129	0.0277	0.0468
20°	$\bar{L}_r$	0.0060	0.0016	0.0172	0.0415	0.0696	0.1002
	$\bar{T}_r$	0.0027	0.0006	0.0069	0.0158	0.0247	0.0318
	$\bar{L}_t$	0.9856	0.9977	0.9698	0.9195	0.8560	0.7842
	$\bar{T}_t$	0.0056	0.0000	0.0061	0.0232	0.0496	0.0838
25°	$\bar{L}_r$	0.0048	0.0013	0.0142	0.0355	0.0632	0.1036
	$\bar{T}_r$	0.0036	0.0010	0.0091	0.0197	0.0278	0.0281
	$\bar{L}_t$	0.9828	0.9978	0.9670	0.9081	0.8306	0.7373
	$\bar{T}_t$	0.0088	0.0000	0.0097	0.0367	0.0784	0.1310
30°	$\bar{L}_r$	0.0038	0.0010	0.0119	0.0331	0.0764	0.8178
	$\bar{T}_r$	0.0041	0.0012	0.0105	0.0199	0.0189	0.0687
	$\bar{L}_t$	0.9793	0.9978	0.9635	0.8935	0.7909	0
	$\bar{T}_t$	0.0128	0.0000	0.0141	0.0535	0.1138	0.1135

are then given as functions of seismic velocity ratio, a, and angle of incidence (with the vertical) θ, where:

$\bar{L}_r$ = longitudinal wave reflection coefficient

$\bar{T}_r$ = transverse wave reflection coefficient

$\bar{L}_t$ = longitudinal wave transmission coefficient

$\bar{T}_t$ = transverse wave transmission coefficient

The sum of the coefficients must equal unity, i.e.,

$$\bar{L}_r + \bar{T}_r + \bar{L}_t + \bar{T}_t = 1$$

It may be seen from Table 1 that at angles of incidence less than critical, a large fraction of the energy in the incident wave is transferred to the refracted longitudinal wave. Much of this transferred energy is then refracted into still lower layers. In each of the layers into which waves are refracted, and at ranges beyond their respective critical angles, the refracted wave propagates outward in a direction parallel to the upper interface of the layer. Under these conditions, however, the transfer of energy across the interface is not a strong one and only a small percentage of the energy in the refracted waves returns to the upper layer.

It is evident that at angles of incidence greater than the critical value, all of the energy in the incident longitudinal wave must be reflected since refractions cannot occur. The energy flux density, or energy per unit area, in the reflected wave decreases slightly with increasing angles of incidence, reaches a minimum and then increases slowly. However larger angles of incidence imply greater ranges and for cases where the incident wave is spherical, rather than plane, spatial dispersion tends to offset the effect of the increases in the reflection coefficients. Nonetheless, the net result is that the reflections have a greater influence on the motion in the upper, softer layer than the refractions returning from the lower layer. It may be noted, however, from Figure 8 that the first wave arriving at the surface will always be a direct wave or a refraction, never a reflection.

This conclusion is supported by the work of Wolf (10) who attempted to explain the low amplitudes and low frequencies of refracted waves observed in seismic explorations. Wolf considered a profile consisting of two semi-infinite elastic media with both the source of disturbance and the recording station located in the upper, softer medium. In a numerical example, he assumed that the seismic velocity in the upper layer was 10,000 feet per second, the seismic velocity in the lower layer was 15,000 feet per second, and the range was 5000 feet. The disturbance was a displacement pulse of 0.02 second duration.

The calculated horizontal displacement at the recording station is shown in Figure 12. The refracted wave, RR, arrived at the station at time 0.33 seconds after the initiation of the disturbance and consisted of a unidirectional pulse which lasted until time 0.5 seconds when the direct wave, D, arrived. Shortly after the arrival of the direct wave, the motion due to a reflection, RF, from the interface was observed.

Wolf notes that for this case the amplitude of the horizontal component of the displacement due to the refraction was only 0.08 times the amplitude of the direct wave and that the direction of the returning refracted wavefront was that of total reflection, i.e., at the angle of critical refraction.

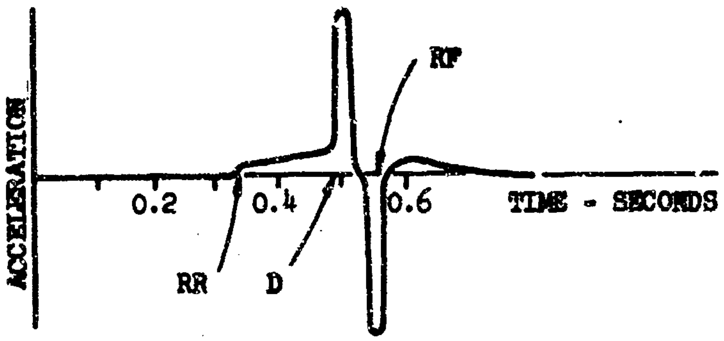

Figure 12. Waveform of Horizontal Ground Motion: RR - Refracted Wave, D - Direct Wave, RF - Reflected Wave (10).

The previous discussion has been concerned with waves generated by a single point source of energy. However the nuclear burst also generates a strong airblast wave which loads the ground surface progressively as it propagates outward from the origin. As a result, the strengths of the refracted waves could be reinforced by the loading of subsequent points as the air wave advances over the ground surface. The direct and reflected waves could also be reinforced in the same manner. The degree of reinforcement would also depend upon the seismic velocities, thicknesses of the layers, and velocity of the air wavefront. Since both the reflected and refracted waves result from the incidence of the direct wave on an interface, it is probable that if reinforcement were to occur from the air wave, all waves would benefit nearly proportionately and the amplitude ratios would remain about the same. This reasoning will be examined further in the section comparing the actual test data with the predictions using the wavefront diagram.

The transmission and reflection coefficients contained in Table 1 are derived for a two layer case. The results may, of course, be applied to a multiple layer system in a step-by-step process. However, in order to show the influence of the angle of incidence and the influence of multiple stratification, Muskat and Meres (9) presented a number of examples. Figure 13 is taken from their work.

Examination of the examples of Figure 13 show that, when the angle of incidence is less than the critical angle, the effect of the magnitude of the angle of incidence is small. For most estimates of the energy return, an assumption of normal incidence is justified, and the angle of incidence with the deepest layer should suffice for all purposes when normal incidence is not explicitly assumed.

It can also be seen from the examples that the presence of intermediate interfaces greatly attenuates the energy ultimately returning from the layer of greatest depth. A single intermediate interface reducing the total velocity contrast by two will reduce the fraction of incident energy returning from the highest velocity layer by a factor of five. An additional intermediate interface causes a further reduction by a factor of about five, so that the energy returning ultimately from the 16,000 feet per second velocity layer would be only 0.4 percent in Figure 13(g), as compared to 11.1 percent of the incident energy in Figure 13(a). Part of this attenuation is due to the energy reflected from the intermediate interfaces. However, about half of the total decrease is due to the higher ultimate loss of the incident energy by transmission into the highest velocity layer because of the reduced velocity contrast.

Figures 13(h) and 13(i), which correspond in their gross features to the type of section encountered in certain Midwestern districts, show again the high degree of attenuation resulting from the intermediate reflection processes. Under the assumed conditions, less than one percent of the incident energy will return from the highest velocity and deepest layer, whereas more than five percent will return from the two upper interfaces.

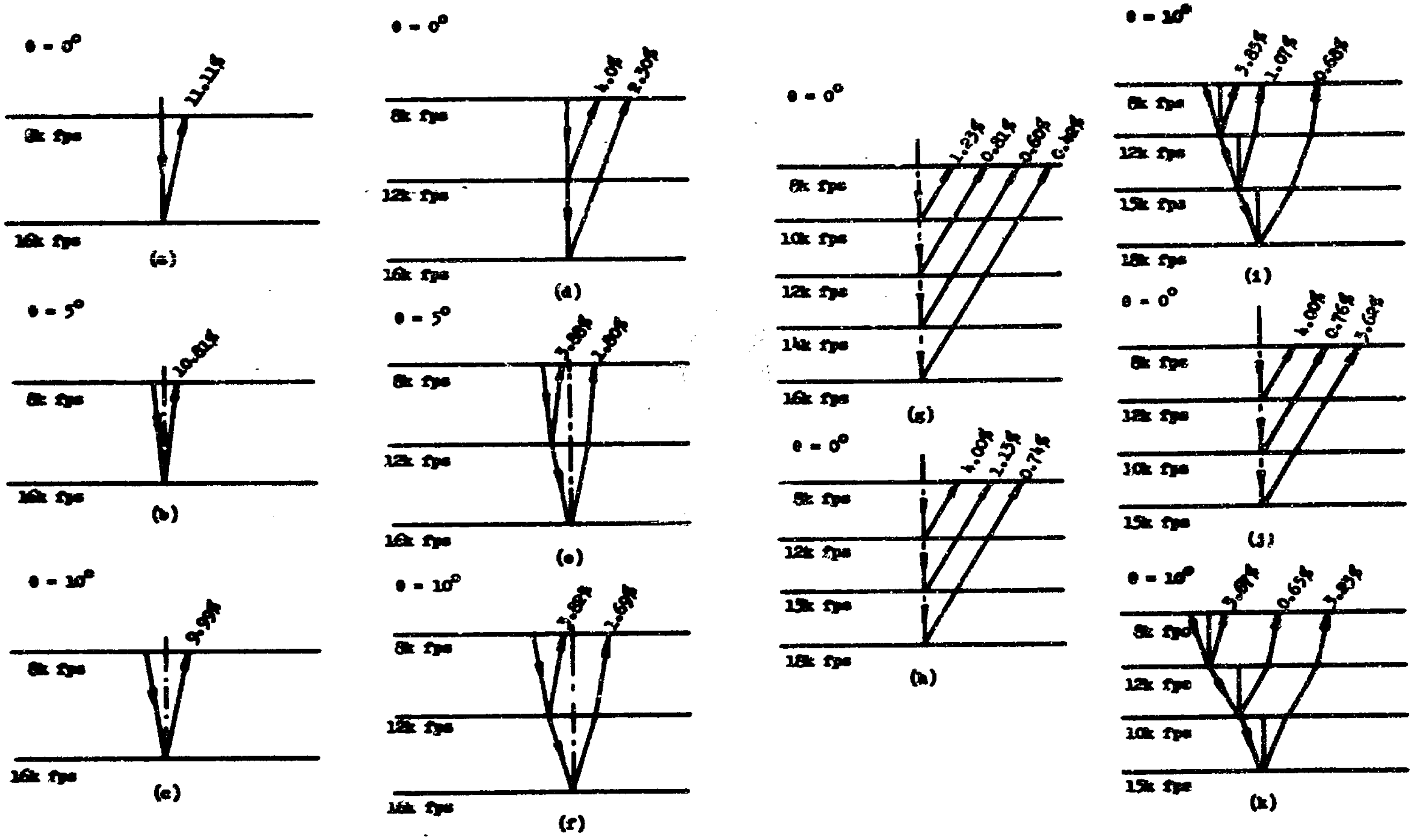

Figure 13. Reflected Energy in Multiple Layer System.

The velocity sections of Figures 13(j) and 13(k) show the influence of an intermediate low-velocity layer. It is seen that, if the section resumes its normal velocity increase with depth after passing the low-velocity layer, the high contrast at the base of the latter will give rise to high reflection coefficients and greater ultimate returns of reflected energy to the surface than will sections where the velocities increase monotonically with depth and where all the contrasts are rather small. Thus, in the specific cases shown in Figures 13(j) and 13(k), almost as much energy will be returned from the deepest layer as from the first interface. Moreover, in comparing Figure 13(j) with 13(h), more than three times as much energy will be reflected from the 15,000 feet per second layer in Figure 13(j) than in Figure 13(h), although the latter has one less intermediate interface.

The percentage of the energy reflected from a weathered or indistinct interface between layers would be significantly reduced below the values given in the tables or examples. An indistinct boundary between layers of a geologic formation is often the result of a gradual change in the conditions of deposition or weathering prior to deposition of the succeeding layer. In this case, the velocity gradient is gradual and may result in more of the energy being refracted into the deeper formation and less being reflected.

The percentage of energy reflected at a discontinuity increases rapidly as the angle of incidence approaches the critical refraction angle. However, Gutenberg (11) showed that there would be no corresponding increase in the amplitudes of the reflected waves at the ground surface. Instead, the maximum amplitudes of reflected waves are found near the source of the disturbance. This is because the ground motion is due both to the reflection from the interface and to its subsequent re-reflection downward from the ground surface. The amplitude also depends on the rate of change of the angle of incidence with distance. That is, the larger the angle of incidence the larger the area will be at the ground surface over which the initial energy intensity will be spread.

(4) Use of Time-Distance Curves and Wavefront Diagram with Airblast Arrival Curve. The time-distance curves, whether derived from the construction of a wavefront diagram or plotted from a seismic survey, can be used in conjunction with the airblast arrival curve to predict the point of first outrunning and the arrival time of various ground waves at the point of interest. Figures 14 through 17 present the time-distance curves derived from the wavefront diagram of Figure 5, and the airblast arrival curve for a 20 MT weapon, (Figure 18). The series of figures illustrates the procedure used in locating the range where the arrival time of the refracted wave coincides with that due to the airblast. At greater ranges the refracted wave will arrive prior to the airblast pressure. In addition to the arrival times of the refracted waves, the arrival times of the direct wave and the reflected wave from the two deeper layers are also indicated.

The range at which outrunning first occurs may be found by sliding the origin of the refracted wave time-distance curve along the airblast arrival time curve until the two intersect at the minimum ground range. This point will be found when the origin of the refraction time-distance curve is located at the point on the airblast arrival curve where the velocity of the airblast wave equals the velocity of the layer whose time-distance curve intersects the airblast wave arrival time curve. For example, in Figure 14 the origin is located at a point on the airblast curve where the airblast front is traveling with a velocity of approximately 10,000 feet per second. This is equal to the velocity of Layer 3.

In this example, outrunning occurs first on the ground surface at Station 6200. The origin of the refracted wave arriving first at Station 6200 was the disturbance generated by the airblast wave when it

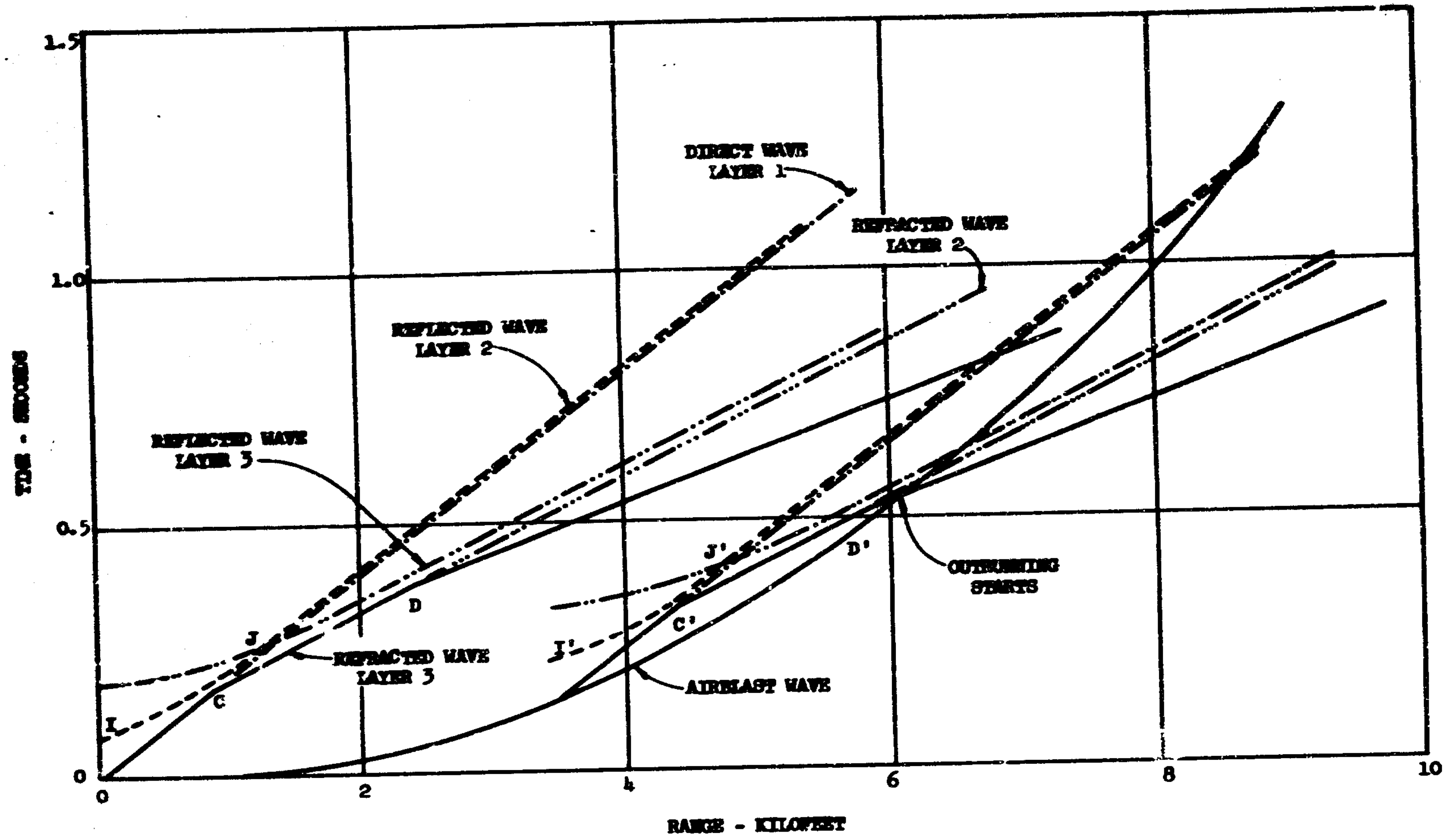

Figure 14. Location of Range of First Outrunning with Source at a Range of 3500 Feet.

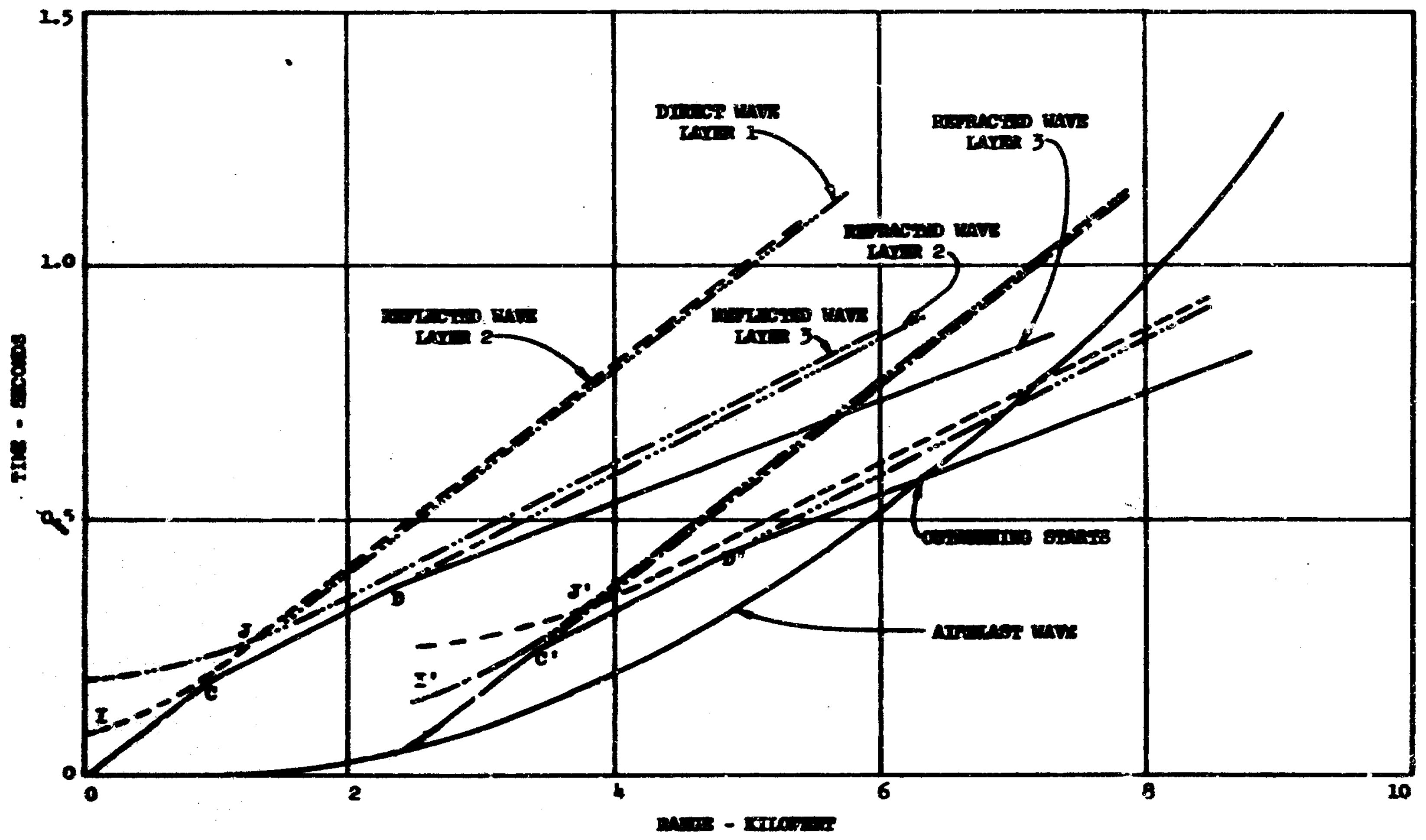

Figure 15. Location of Range of First Outrunning with Source at a Range of 2500 Feet.

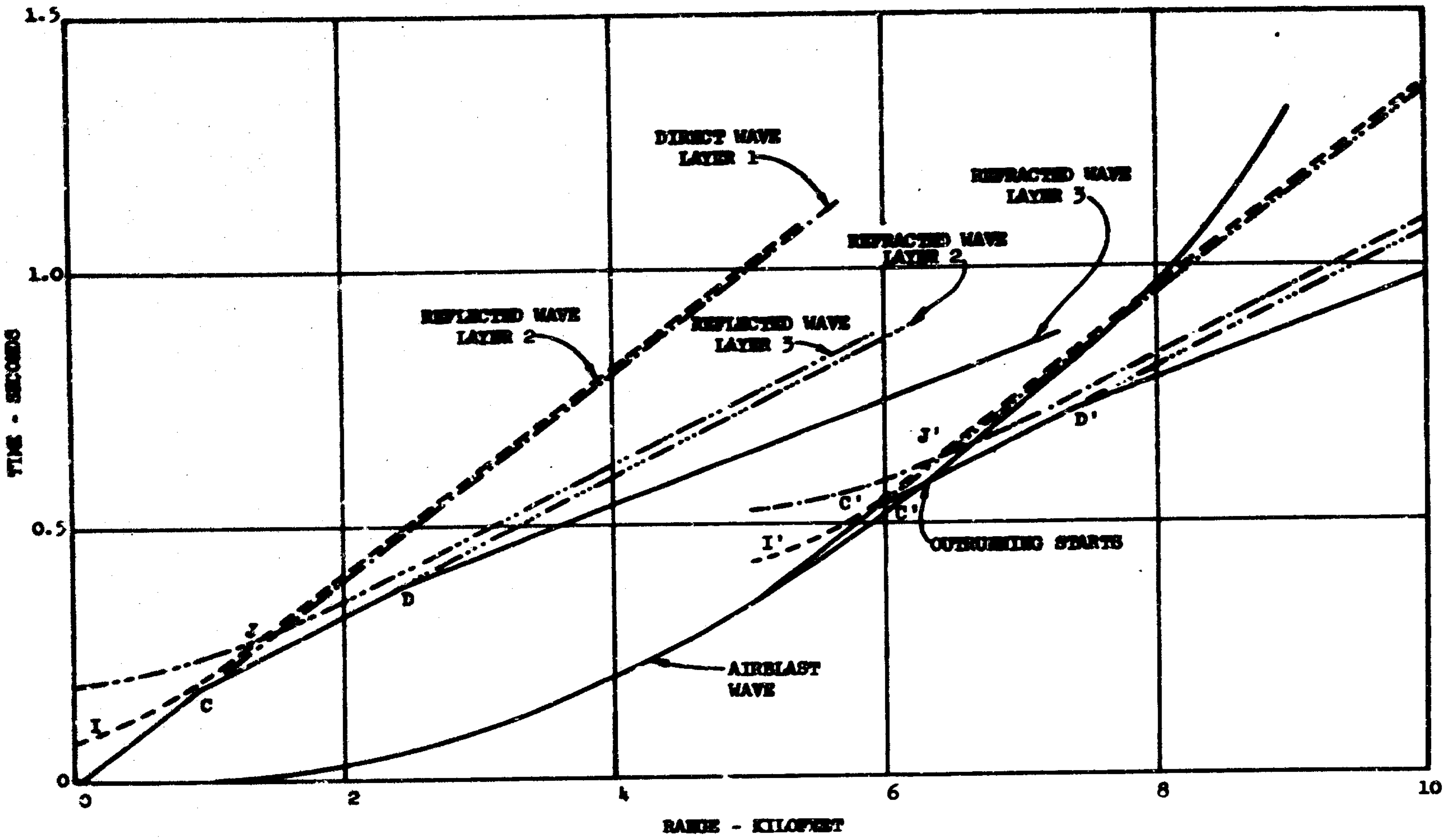

Figure 16. Location of Range of First Outrunning with Source of a Range of 5000 Feet.

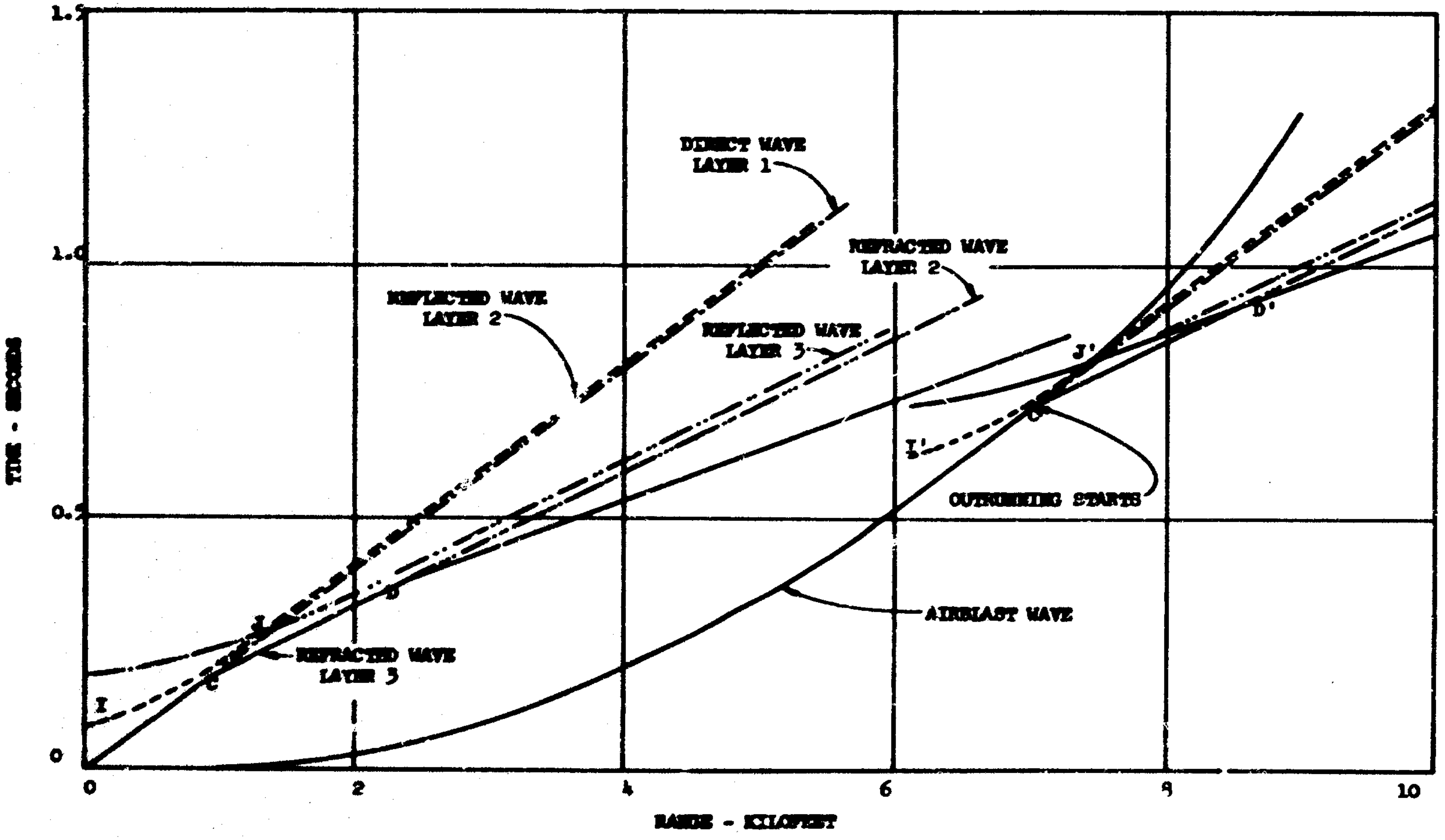

Figure 17. Location of Range of First Outrunning with Source at a Range of 6100 Feet.

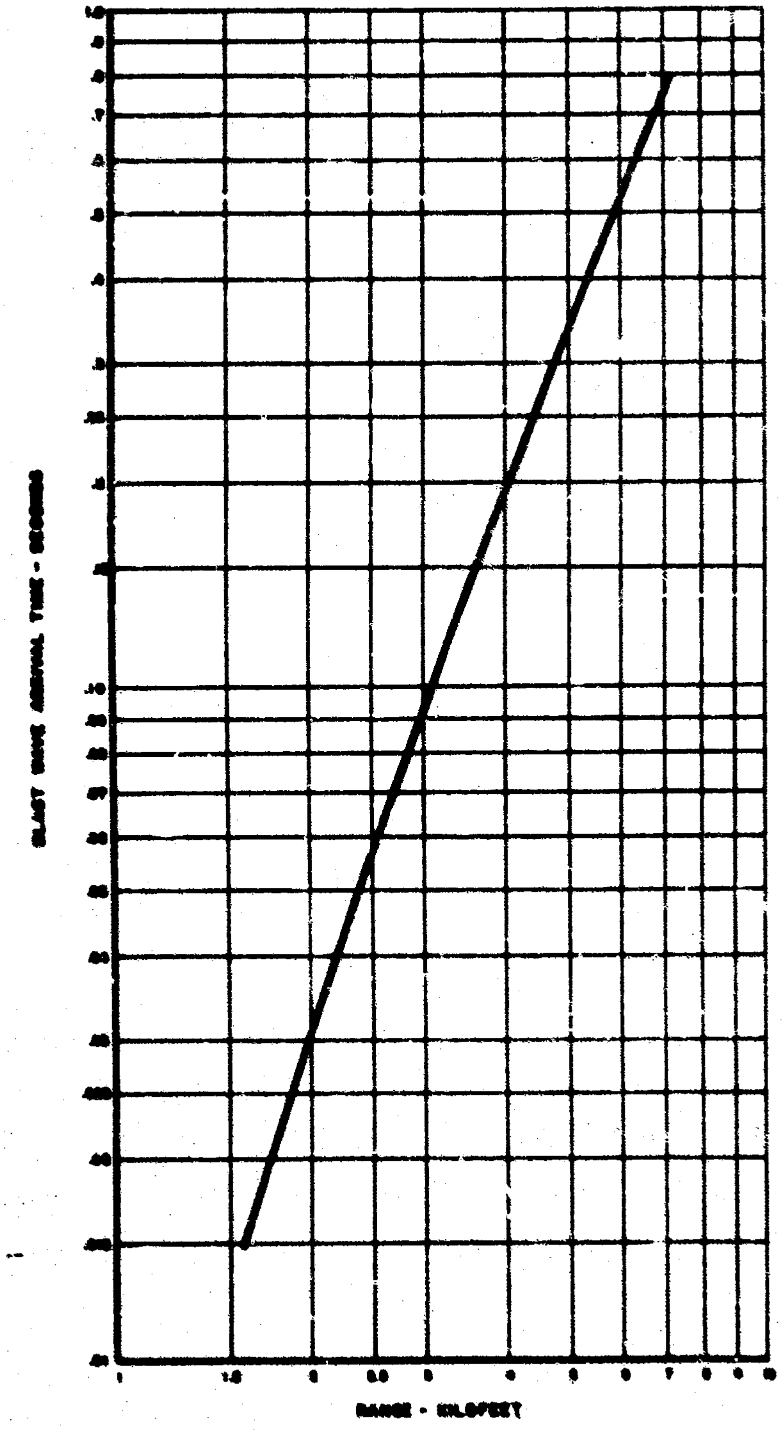

Figure 18. Airblast Arrival Time Curve for 20 MT Weapon.

was at a range of 3500 feet. The peak overpressure at Station 6200 is 300 pounds per square inch, and at Station 3500 is 1500 pounds per square inch (27).

It may be noted in Figures 14 through 17 that the refracted wave reaches stations between 6200 and 6300 feet when the origin varies over a range between 2500 and 5000 feet. Due to the velocity variation of the airblast wave and the seismic velocities, all the energy carried by the critically refracted waves between this range will arrive at nearly the same time.

Figures 19 through 23 indicate the contours on which disturbances generated at time t arrive simultaneously at the point of interest. Figure 19 is a plan view of the ground surface and contains one set of concentric curves radiating from Ground Zero (GZ), representing the position of the airblast wavefront at various time intervals. The airblast data are from Operation Tumbler Shot No. 1, and are presented with the wavefront diagram in Figures 24 and 25. The concentric circles radiating from Station 5V are lines of constant transit time from a disturbance on the surface to Station 5V. The transit times were obtained from a modified time-distance curve (Figure 26) for Frenchman Flat (FF-1). The time-distance curve for this site in turn was obtained by construction of a refraction wavefront diagram (Figure 27). The somewhat elliptical contours were then drawn through points which yielded equal transit times from Ground Zero to Station 5V. The diagrams and figures are used later to compare the predictions of the direction of motion and arrival times with the field data from the shots performed at this site during Operation Tumbler Shot No. 1.

It can be noted by examination of Figure 19 that the areas within which an impetus of finite duration may be generated and may arrive at the station at the same time represent a wide range of instantaneous pressures and transit distances. In the particular conditions used to construct Figure 19, it can be seen, for example, that the refracted wave at an

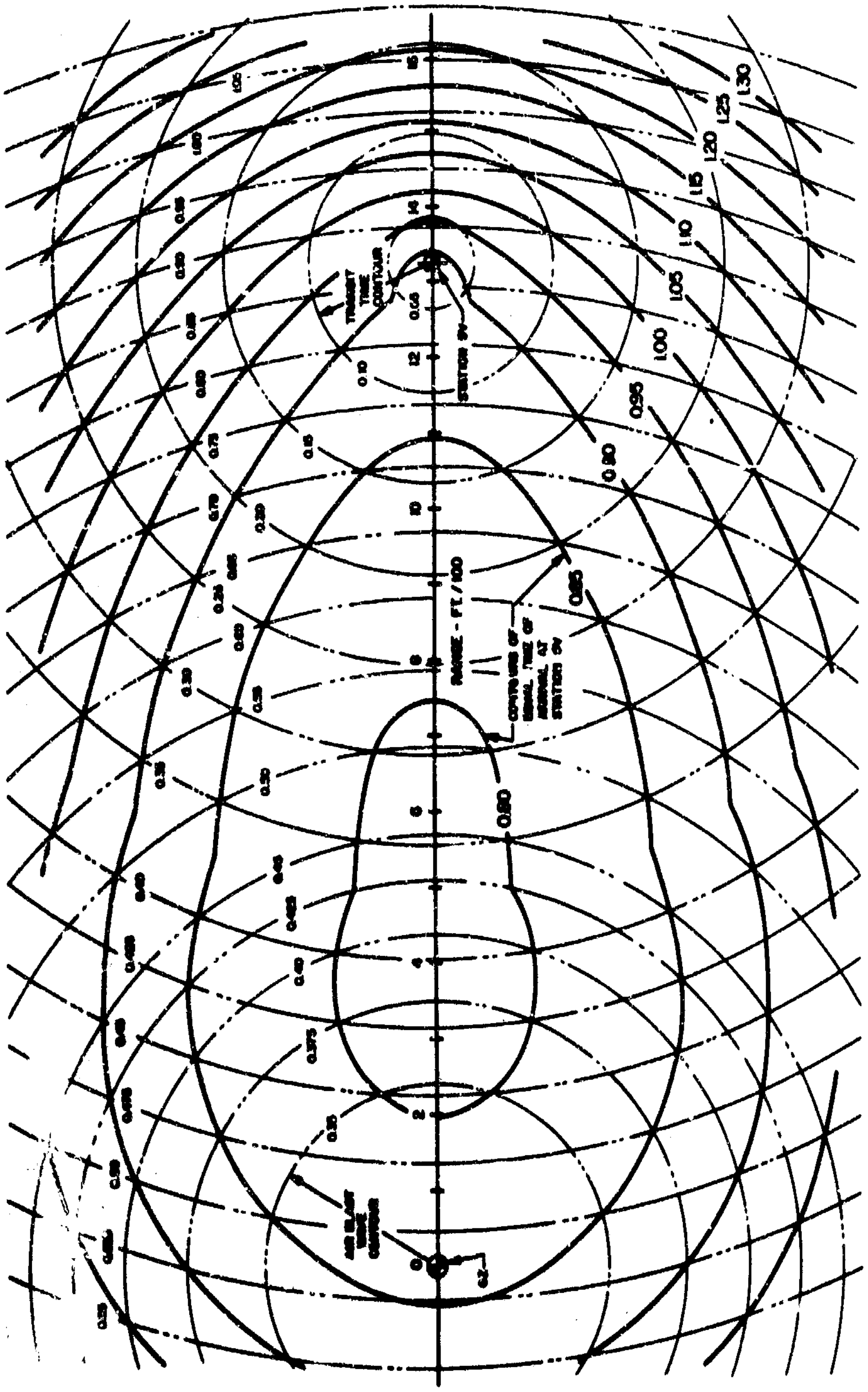

Figure 19. Contours of Equal Arrival Time, First Arrivals, Operation Tumbler, Shot No. 1, Station 5V.

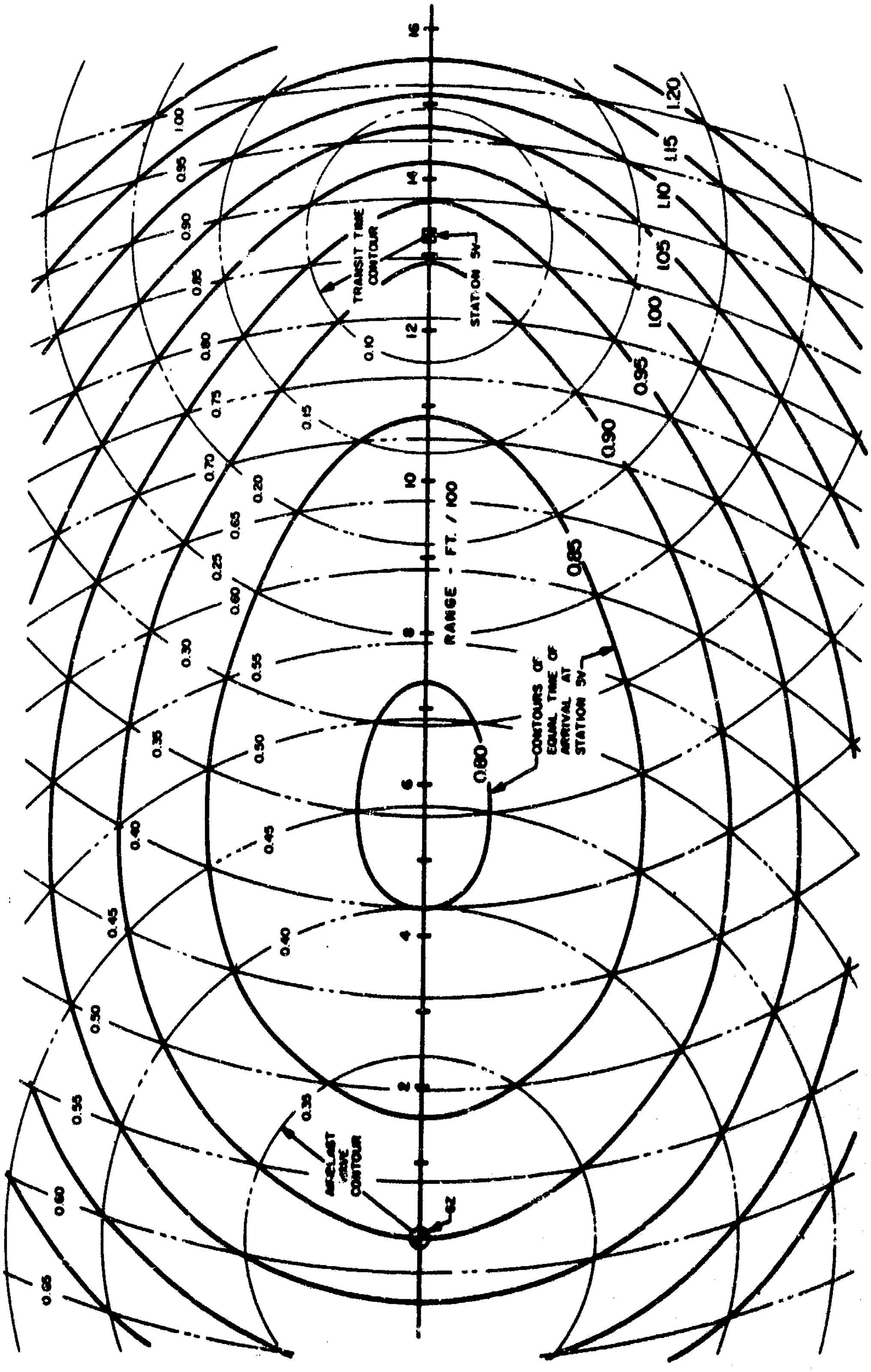

Figure 20. Contours of Equal Arrival Time, Refracted Waves from Layer 2, Operation Tumbler, Shot No. 1, Station 5V.

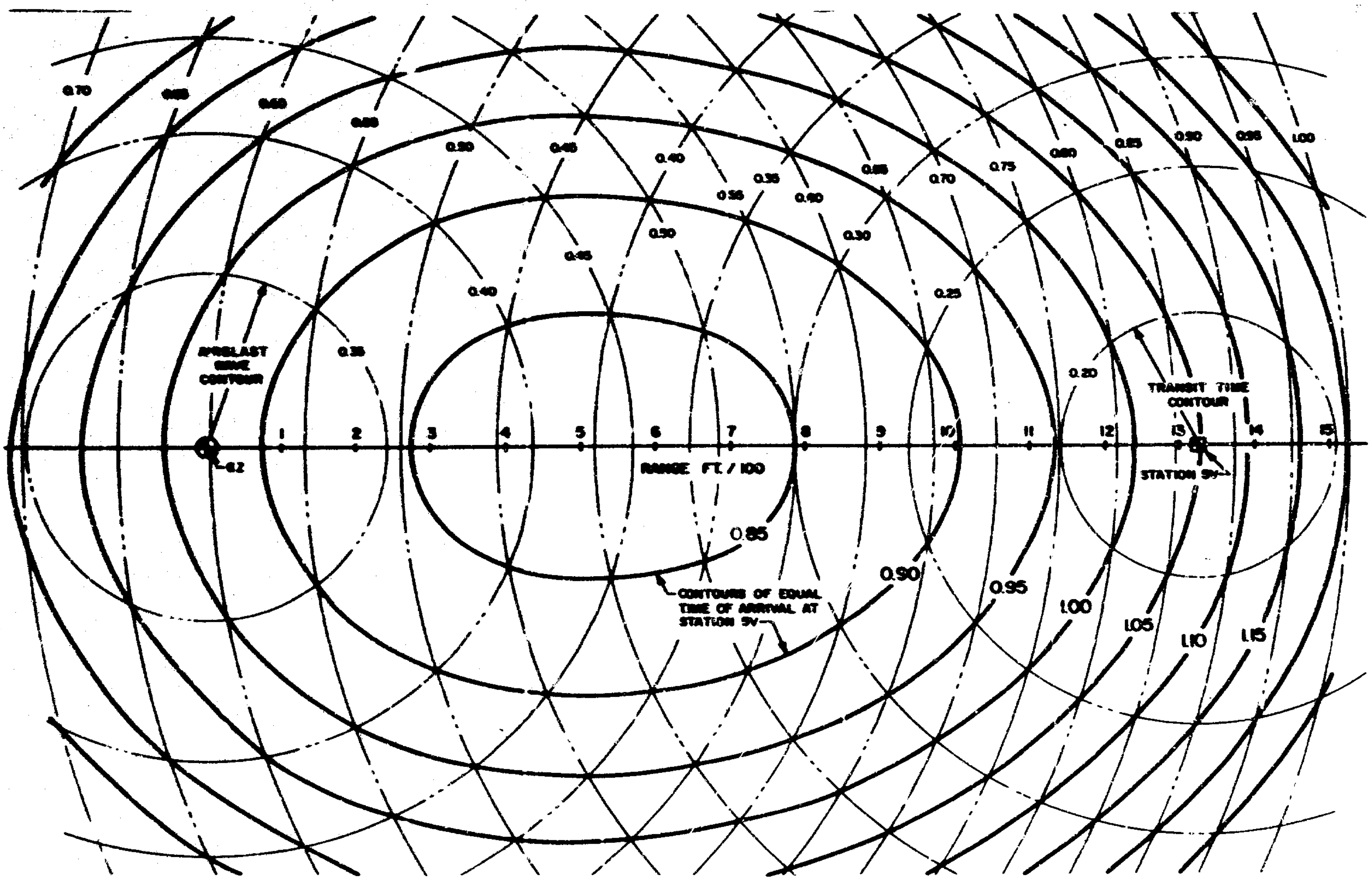

Figure 21. Contours of Equal Arrival Time, Reflected Waves from Layer 3, Operation Tumbler, Shot No. 1, Station 5V.

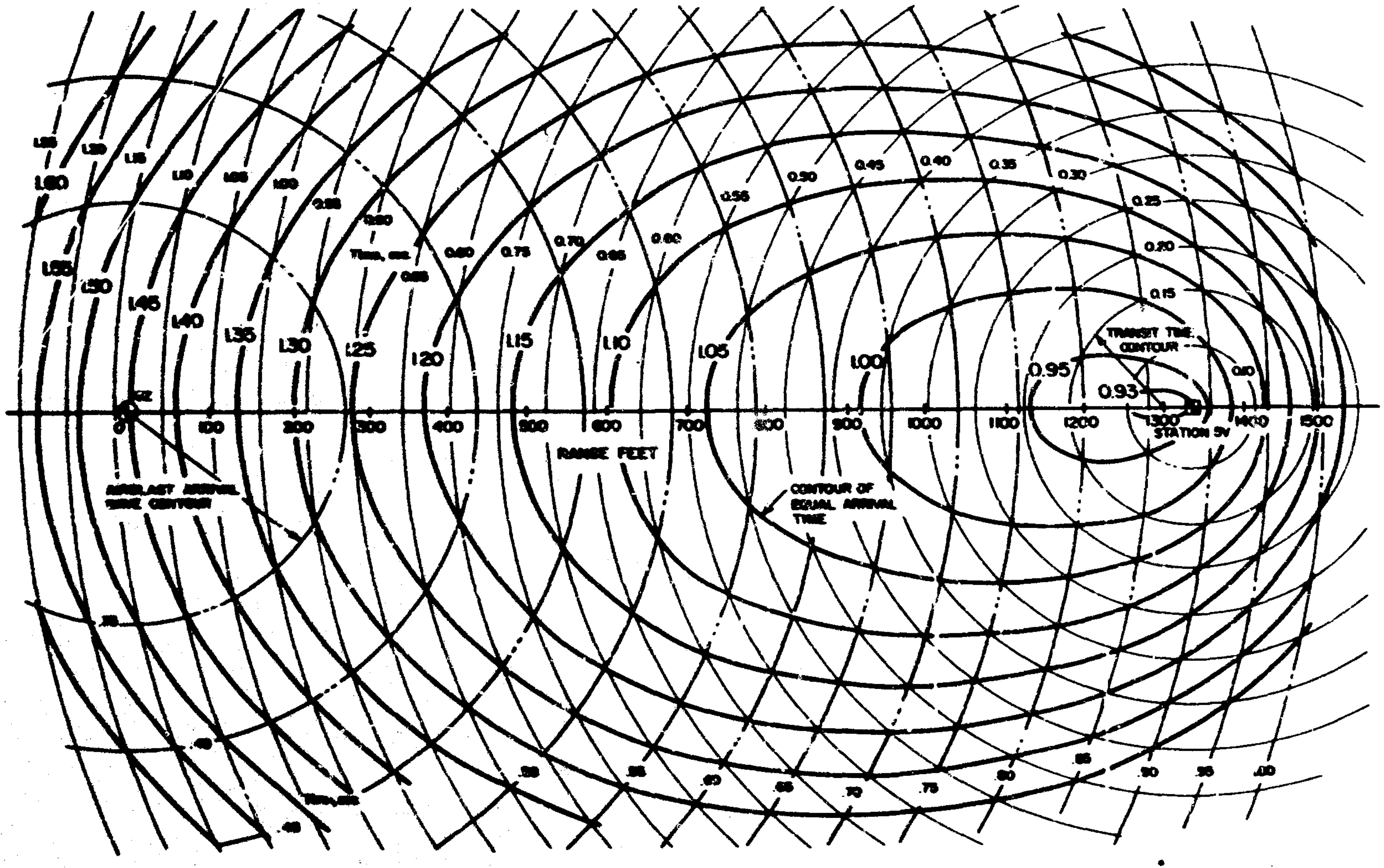

Figure 22. Contours of Equal Arrival Time, Reflected Waves from Layer 2, Operation Tumbler, Shot No. 1, Station 5V.

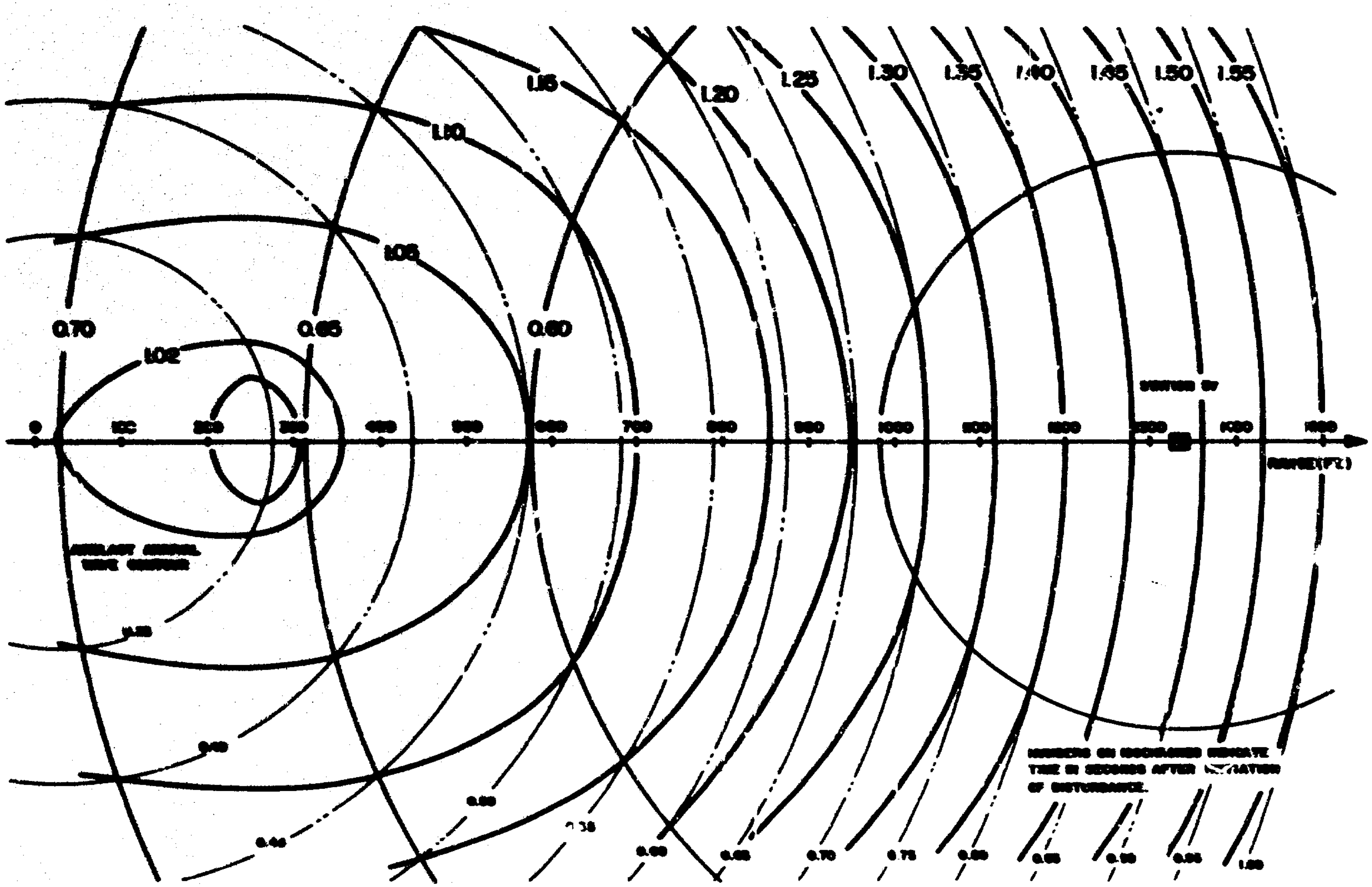

Figure 23. Contours of Equal Arrival Time, Reflected Waves from Layer 4, Operation Tumbler, Shot No. 1, Station 5V.

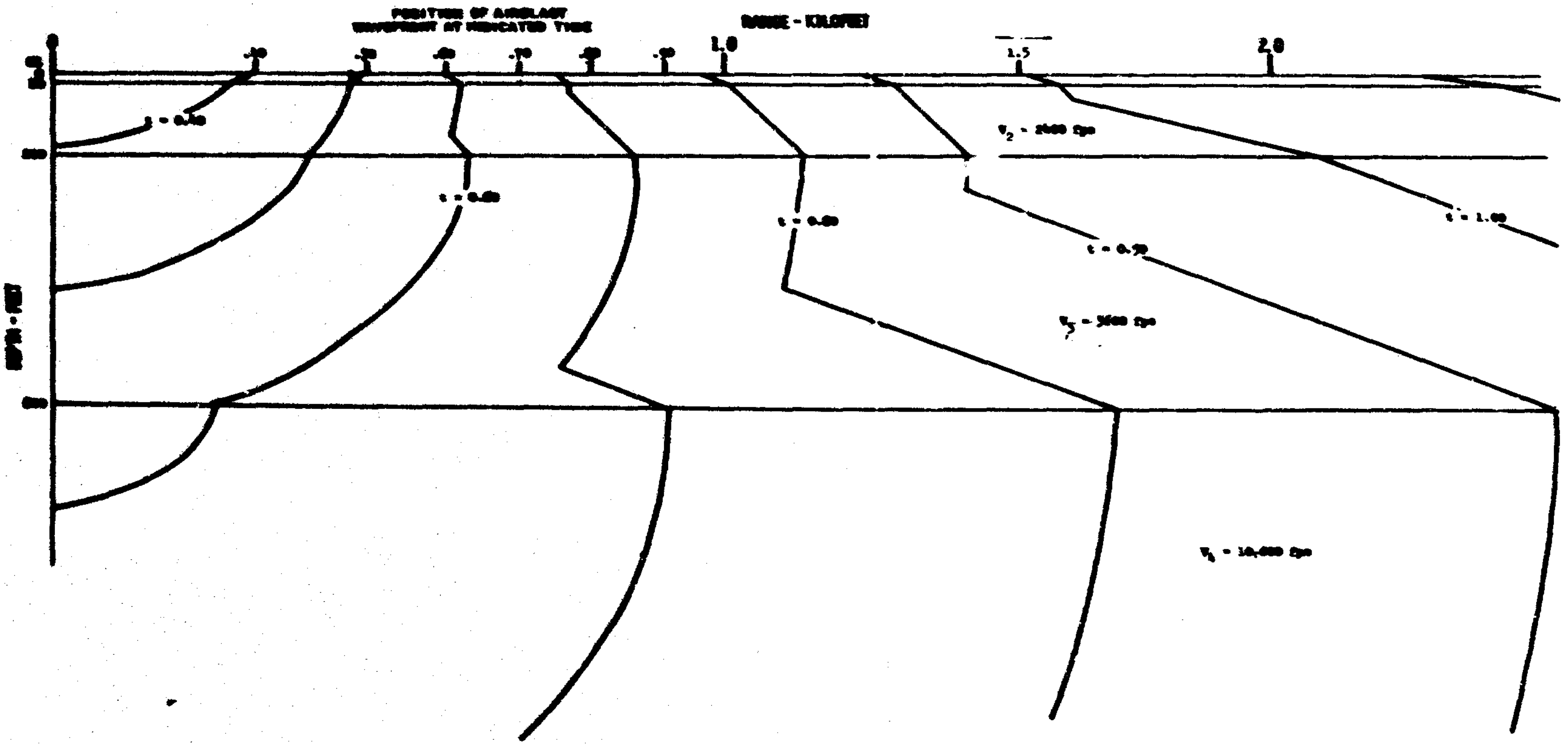

Figure 24. Wavefront Diagram Adjusted to Indicate Refractions from Moving Airblast Wave. Data from Operation Tumbler, Shot No. 1.

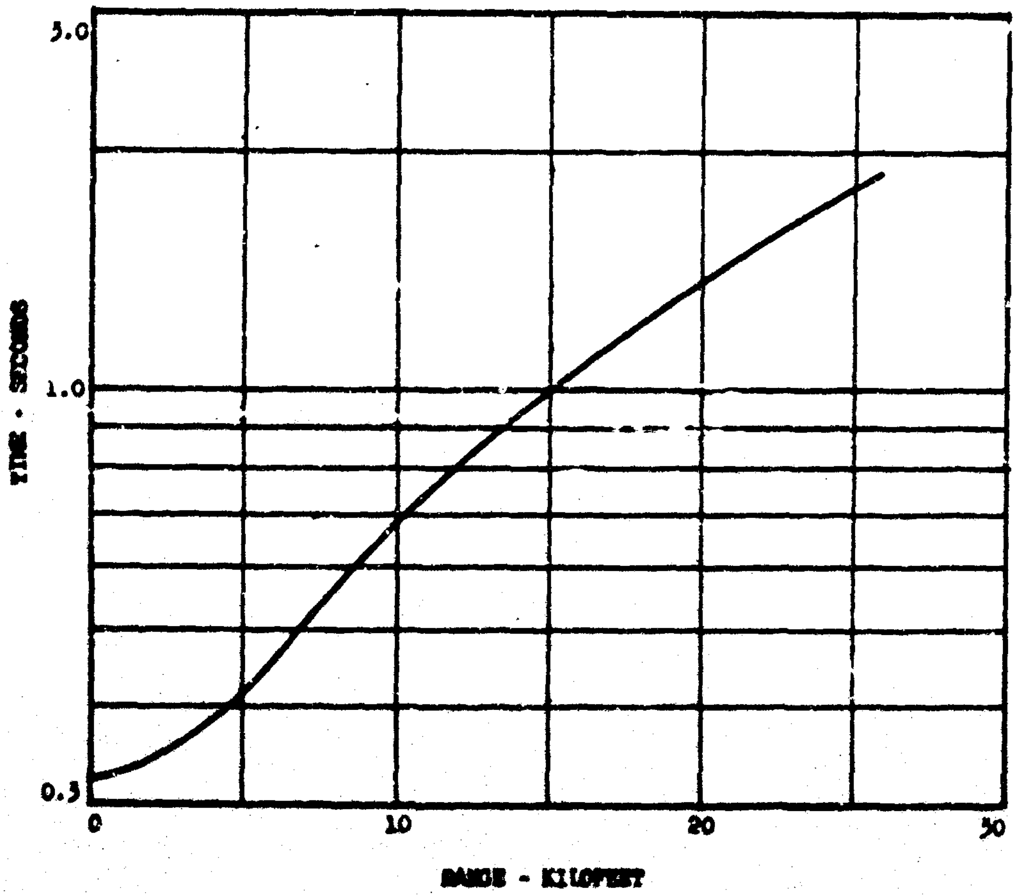

Figure 25. Airblast Arrival Time, Operation Tumbler, Shot No. 1, Yield - 1.05 Kilotons, Height of Burst - 793 Feet.

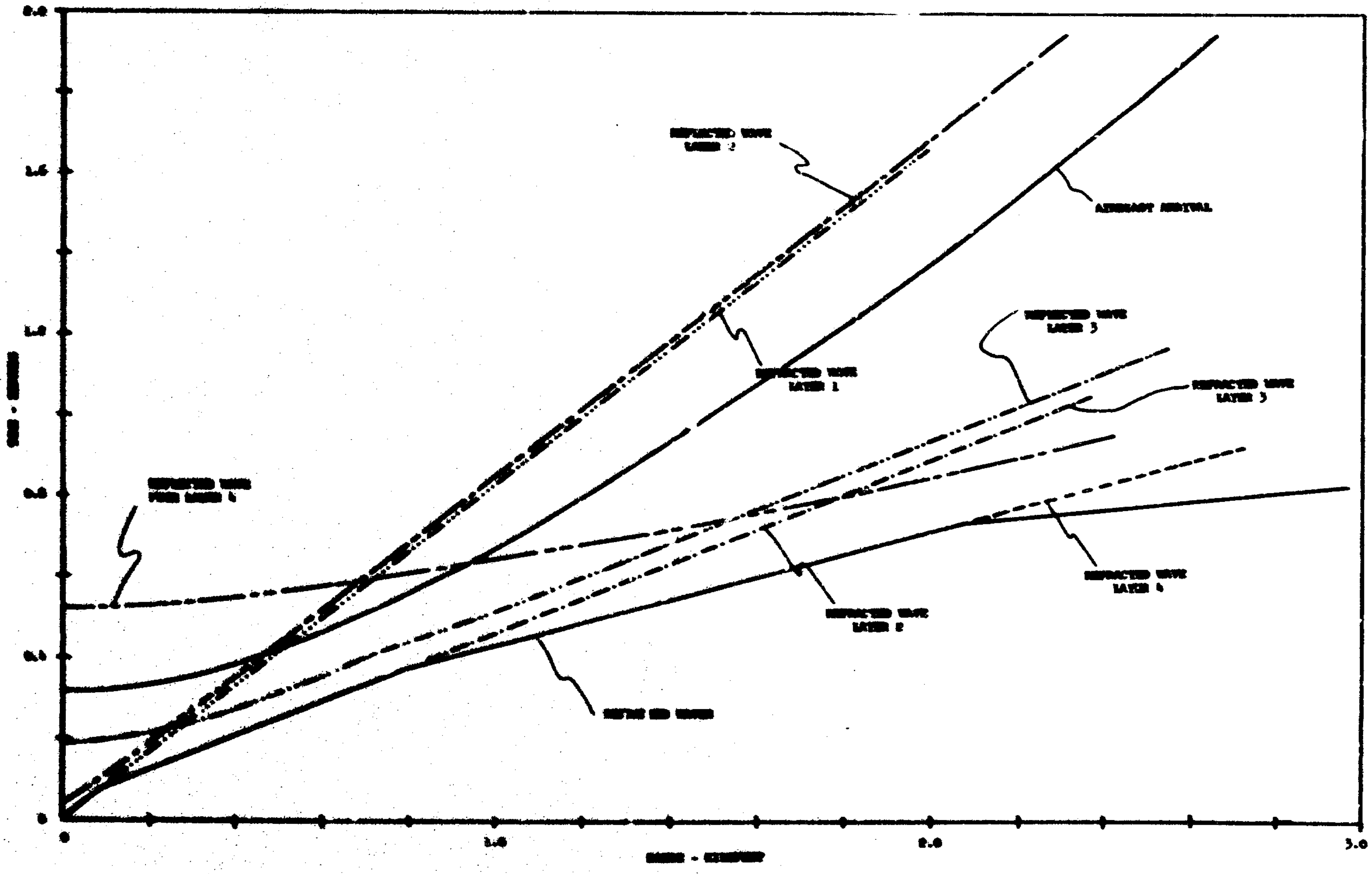

Figure 26. Modified Time-Distance Curve, Operation Tumbler, Shot No. 1.

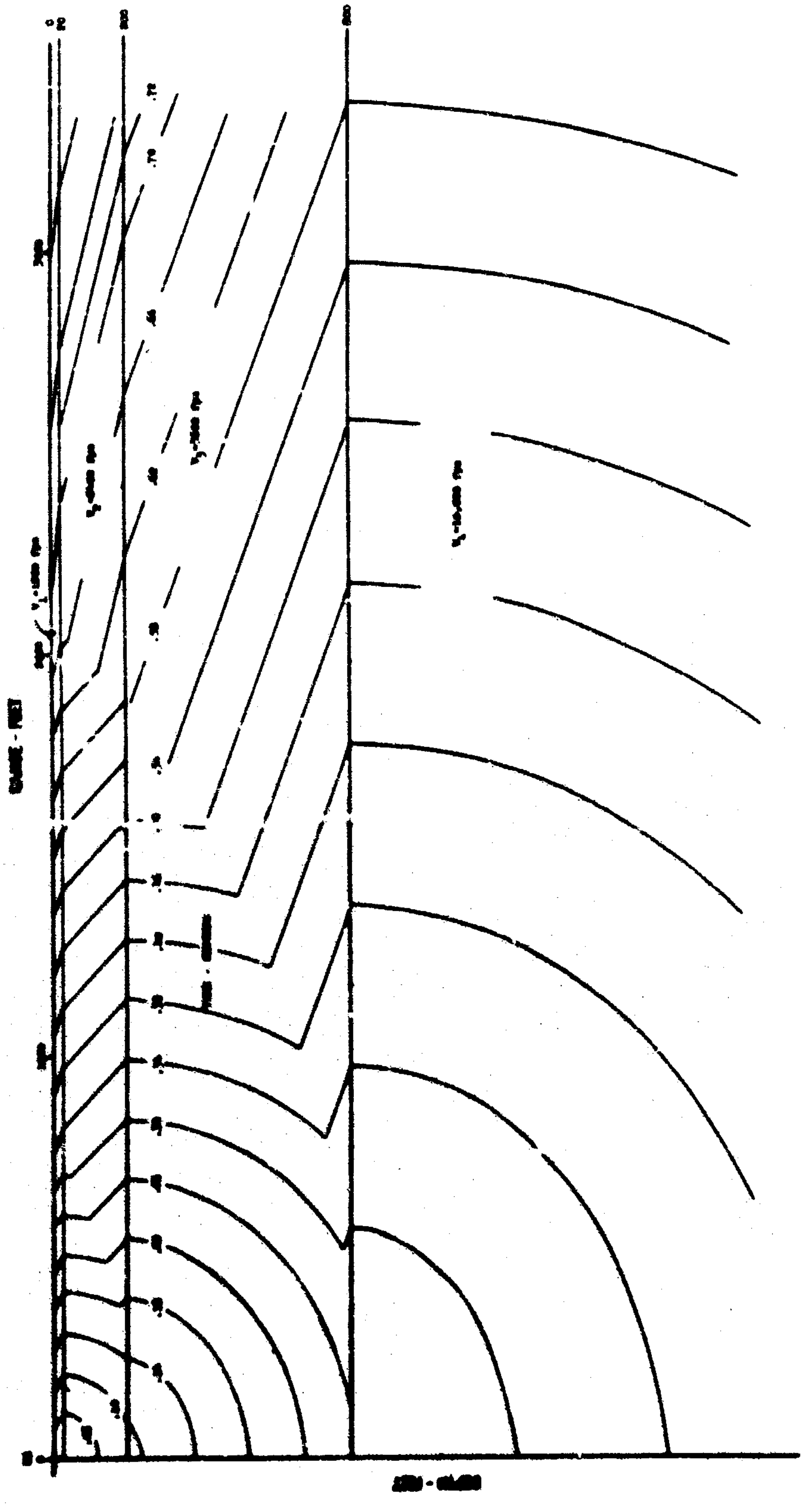

Figure 27. Refraction Wavefront Diagram, Operation Tumbler, Shot No. 1.

arrival time of 0.95 seconds is generated from both the far side of Ground Zero and from points beyond the station of interest. The same general situation is true for the arrivals of the other waves as shown on the other figures. This is one of the several complications which make the prediction of energies at a given station so difficult by graphical methods. General observations regarding the intensities of the various arrivals will be discussed in the section comparing the predictions with the actual field data.

Figure 24 represents the position of the refracted wavefront when the refracted wavefront diagram shown in Figure 27 is combined with the airblast arrival data given in Figure 25. It differs from the refraction diagram of Figure 27 in that in Figure 27 the refracted wavefronts emanate from a point source at "0" while in Figure 25, the refracted wavefronts are generated by the airblast wave moving along the ground surface. Figure 25 is constructed by shifting the origin of the wavefront diagram (Figure 27) so that it represents the position of the airblast front. The various positions of the refracted wave are sketched and their transit time recorded. The envelopes which represent the most advanced positions of the wavefront at a given time are those shown on Figure 24. The times shown represent the total elapsed time since the burst. Since Operation Tumbler, Shot No. 1 was an airblast, the initial time at Ground Zero was equal to 0.32 seconds.

Figure 24 shows the general change of direction and slope of the first arrival wavefronts as they recede from the point of disturbance. From this curve it is possible to scale the arrival times and direction of the first refracted wave at any point below the surface. This diagram does not show the area from which a given wave was generated. If desirable, it would be possible to construct in a similar manner a diagram showing the propagation of reflected waves.

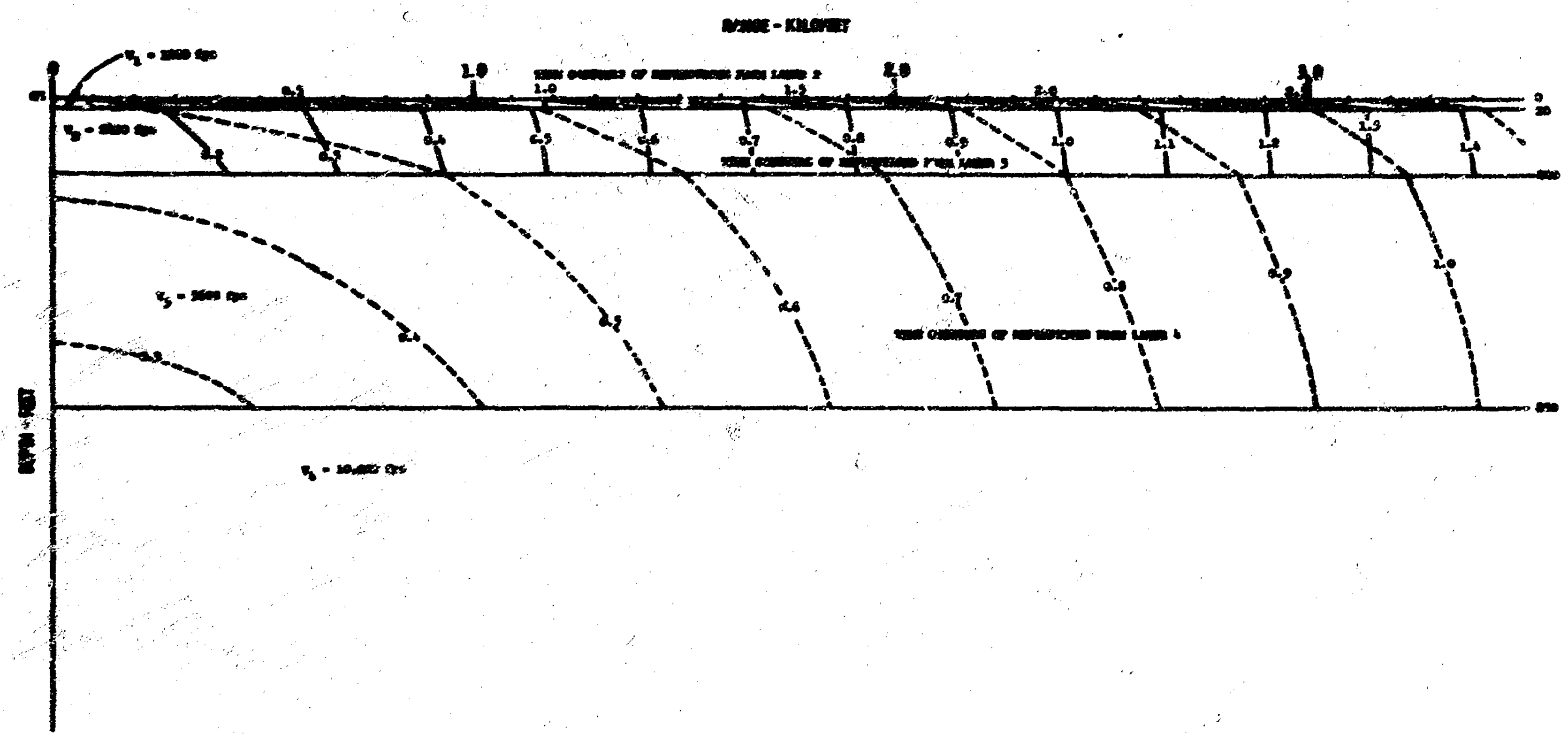

Figure 28. Reflection Wavefront Diagram, Operation Tumbler, Shot No. 1.

C. Comparison of Predictions with Field Data. In this section the acceleration-time waveforms of several test shots are compared with predictions based on the wavefront diagram method outlined in this report. Field conditions and measurements used in this comparison have been obtained from the unclassified reports of Operation Tumbler, Shots No. 1 through No. 4 (12) and from Operation Plumbbob, Shot Priscilla (13). Data from Operation Hardtack-1 (14) are not presented due to their classified nature; however, some of the pertinent observations obtained from a comparison with the data from those shots will be discussed.

First, seismic velocities computed from data obtained in a refraction survey at the test site are compared with those indicated by the shock arrival times during a nuclear test. The comparison of velocities measured during a low stress seismic survey with those of the much higher stress test should indicate the variation of wave velocity with wave strength. A considerable volume of material is available concerning the theoretical and experimental inelastic and dynamic behavior of soils (15); therefore, a discussion of this aspect will not be included in this paper.

In the second part of this section a comparison is made of the predicted arrival times and directions of motion using the wavefront diagram method with the field test records.

(1) Field Test Data. Field test data used in the remaining portions of this section are presented in Tables 2 through 12.

Table 2

FIELD TEST DATA, OPERATION TUMBLER (12)

SHOT	LOCATION	DATE	HEIGHT OF BURST (ft)	YIELD (KT)
1	FF	1 April 1952	793	1.05
2	T-7	15 April 1952	1109	1.15
3	T-7	22 April 1952	3447	30.00
4	T-7	1 May 1952	1040	19.60

Table 3

SEISMIC VELOCITIES (MODIFIED), OPERATION TUMBLER SIZES (12)

FRENCHMAN FLAT		YUCCA FLAT, T-7 AREA	
DEPTH (ft)	SEISMIC VELOCITY (fps)	DEPTH (ft)	SEISMIC VELOCITY (fps)
0-20	1500	0-5	800
20-60	2400	5-100	VARIABLE (1200 fps USED)
60-200	2800	100-275	3500
200-800	3600	275-500	5000
800	10,300	500	6000

Table 4

OPERATION TUMBLER, SHOT NO. 1 - GROUNDSHOCK DATA

Station Number	Gage Code Number	Ground Range (ft)	Depth (ft)	Maximum Acceleration (g)			Arrival Time (sec)		Maximum Air Pressure (psi)[k]
				Direct Transmitted	Airblast Induced Negative	Airblast Induced Positive	Direct Transmitted	Airblast Induced	
200	0V	227	5	-	15.0	3.89	-	0.347	25.7
201	1V	384	5	-	10.53	1.57	-	0.384	22.1
202	2V	607	5	-	5.57	1.04	-	0.466	13.8
203	3V1	*	*	*	*	*	*	*	*
203	3V	845	5	-	4.10	0.74	-	0.583	10.1
203	3V50	861	50	0.03	0.65	0.19	0.58	0.598	10.2
203	3H	845	5	-	0.62	0.75	0.58	0.581	10.1
203	3H50	861	50	-	1.26	0.68	0.57	0.578	10.2
203	3T	845	5	-	0.72	0.81	0.58	0.583	10.1
203	3T50	861	50	-	0.18	0.13	0.58	0. 84	10.2
204	4V	1089	5	0.48	3.44	1.17	0.67	0.729	10.8
205	5V	1335	5	0.16	3.72	1.38	0.76	0.842	9.7
206	6V	1582	5	0.12	3.10	0.45	0.80	1.062	7.8
207	7V	1830	5	0.12	2.71	0.85	0.83[b]	1.247	6.7
208	8V	2078	5	0.11	1.92	0.46	0.95	1.434	5.2
209	9V	2576	5	0.07	1.39	0.43	1.00	1.826	3.4
210	10V1	*	*	*	*	*	*	*	*
210	10V	3075	5	0.05	1.03	0.44	1.06	2.226	2.47
210	10V50	3079	50	0.02	0.17	0.19	1.04	2.227	2.47
210	10H	3075	5	0.04	0.32	0.38	1.06	2.234	2.47
210	10H50	3079	50	c	0.07	0.09	1.05	c	2.47
210	10T	3075	5	c	0.09	0.12	1.03	2.240	2.47
210	10T50	3079	50	**	**	**	**	**	**

b Later arrival at 0.90 sec.
c Direct transmitted and airblast induced waves interfere; value uncertain
k Interpolated from original air pressure data
* Gage not connected for this shot
** Gage out of order

Table 5

OPERATION TUMBLER, SHOT NO. 2 - GROUNDSHOCK DATA

Station Number	Gage Code Number	Ground Range (ft)	Depth (ft)	Maximum Acceleration (g)			Arrival Time (sec)		Maximum Air Pressure (psi) k
				Direct Transmitted	Airblast Induced Negative	Airblast Induced Positive	Direct Transmitted	Airblast Induced	
200	0V	127	5	-	2.74	2.25	-	0.554	13.04
201	1V	625	5	-	2.38	1.14	-	0.676	9.85
202	2V	1374	5	0.09	1.22	0.54	0.95f	1.069	6.24
203	3V1	*	*	*	*	*	*	*	*
203	3V	2120	5	0.07	1.12	1.28	1.13f	1.589	4.58
203	3V50	2123	50	0.03	0.18	0.47	1.10f	1.589	4.57
203	3H	2120	5	0.05	0.68	0.47	1.10f	1.592	4.58
203	3H50	2123	50	0.03	0.18	0.47	1.12f	1.590	4.57
203	3R	2120	5	0.06	0.20	0.33	1.13f	1.58	4.58
203	3R50	2123	50	0.02	0.10	0.09	1.12f	1.58	4.57
204	4V	2874	5	0.04	0.74	0.75	1.27f	2.165	3.52
205	5V	3624	5	0.03	0.48	0.20	1.40f	2.778	2.29
206	6V	4374	5	0.02	0.37	0.50	1.52f	c	1.89
207	7V	5124	5	0.02	0.41	0.36	1.65f	c	1.24
208	8V	5875	5	0.02	0.55	0.68	2.10gh	c	1.07
209	9V	7375	5	0.01	0.33	0.30	2.36g	c	0.89
210	10V1	*	*	*	*	*	*	*	*
210	10V	8875	5	0.01	0.21	0.25	2.58g	c	0.48
210	10V50	8875	50	0.01	0.014	0.01	2.58g	c	0.48
210	10H	8875	5	0.01	0.18	0.36	2.53g	c	0.48
210	10H50	8875	50	0.01	0.014	0.01	2.55g	7.30	0.48
210	10R	8875	5	e	0.032	0.04	3.07g	7.23	0.48
210	10R50	8875	50	0.001	0.007	0.006	2.76g	7.22	0.48

c Direct transmitted and airblast induced waves interfere; value uncertain
f Negative acceleration
g Positive acceleration
h Very faint negative acceleration at 1.76 sec.
k Interpolated from original air pressure data
* Gage not connected for this shot

Table 6

OPERATION TUMBLER, SHOT NO. 3 - GROUNDSHOCK DATA

Station Number	Gage Code Number	Ground Range (ft)	Depth (ft)	Maximum Acceleration (g)			Arrival Time (sec)		Maximum k Air Pressure (psi)
				Direct Transmitted	Airblast Induced Negative	Airblast Induced Positive	Direct Transmitted	Airblast Induced	
200	0V	226	5	-	4.60	1.69	-	1.720	11.48
201	1V	681	5	-	3.28	1.15	-	1.766	11.70
202	2V	1414	5	-	1.88	0.84	-	1.932	10.15
203	3V1	2160	1	-	5.52	2.26	2.18	2.202	8.72
203	3V	2160	5	-	1.78	1.03	2.18	2,210	8.72
203	3V50	2165	50	-	0.99e	0.50e	2.18e	c,e	8.72
203	3H	2160	5	-	1.54	0.72	2.18	c	8.72
203	3H50	*	*	*	*	*	*	*	*
203	3T	*	*	*	*	*	*	*	*
203	3T50	*	*	*	*	*	*	*	*
204	4V	2907	5	0.12	1.26	0.74	2.37	2.567	7.47
205	5V	3656	5	0.06	1.69	0.11	2.53	2.992	6.34
206	6V	4405	5	0.06	1.52	0.57	2.64	3.462	6.06
207	7V	5154	5	0.08	1.22	9.98	2.65	3.970	4.82
208	8V	5903	5	0.04	1.36	1.60	2.87	4.505	5.32
209	9V	7403	5	0.05	1.32	0.89	3.33	5.637	3.93
210	10V1	8902	1	0.02	1.83	0.88	3.62	6.322	2.83
210	10V	8902	5	0.02	0.92	0.76	3.64	6.825	2.83
210	10V50	8902	50	0.02	0.09	0.21	3.60	c	2.83
210	10H	8902	5	0.03	0.89	1.20	3.64	6.833	2.83
210	10H50	8902	50	0.02	0.09	0.05	3.62	c	2.83
210	10T	8902	5	0.02	0.15	0.21	3.7	6.832	2.83
210	10T50	*	*	*	*	*	*	*	*

e Direct transmitted and airblast induced waves interfere; value uncertain

c Gage rings

k Interpolated from original air pressure data

* Gage not connected for this shot

Table 7

OPERATION TUMBLER, SHOT NO. 4 - GROUNDSHOCK DATA

Station Number	Gage Code Number	Ground Range (ft)	Depth (ft)	Acceleration (g) Maximum Direct Transmitted	Acceleration (g) Precursor Negative	Acceleration (g) Precursor Positive	Acceleration (g) Maximum Negative Airblast Induced	Acceleration (g) Maximum Positive Airblast Induced	Maximum Air Pressure (psi) [k]
200	0V	275	5	-	-	-	28.9	36.8	138
201	1V	626	5	-	-	-	p	p	p
202	2V	1354	5	-	1.19	0.53	0.34	0.97	26
203	3V1	2098	1	0.12	2.20	0.48	0.66	0.93	9.53
203	3V	2098	5	0.22	0.97	0.90	0.30	0.50	9.53
203	3V50	2104	50	0.17	0.42	0.15	0.08	0.28	9.53
203	3H	2098	5	0.31	1.44	0.65	0.39	0.64	9.53
203	3H50	*	*	*	*	*	*	*	*
203	3T	*	*	*	*	*	*	*	*
203	3T50	*	*	*	*	*	*	*	*
204	4V	2844	5	0.22	-	-	1.79	1.29	8.48
205	5V	3593	5	0.19	-	-	1.72	0.46	6.35
206	6V	4342	5	0.06	-	-	1.38	0.93	4.62
207	7V	5091	5	0.07	-	-	1.34	1.28	3.75
208	8V	5841	5	0.06	-	-	0.94	1.17	3.02
209	9V	7339	5	0.07	-	-	0.80	0.63	2.04
210	10V1	8838	1	0.04	-	-	1.06	0.43	1.51
210	10V	8838	5	0.03	-	-	0.49	0.46	1.51
210	10V50	8840	50	0.03	-	-	0.03	0.06	1.51
210	10H	8838	5	0.03	-	-	0.54	0.52	1.51
210	10H50	8840	50	0.03	-	-	0.02	0.05	1.51
210	10T50	8838	5	0.01	-	-	0.10	0.12	1.51
210	10T50	*	*	*	*	*	*	*	*

k Interpolated from original air pressure data

p Gage IV shows two shocks; air pressure, 26 and 45 psi; neg. airblast induced acceleration 3.95 and 8.13 G; pos. airblast induced acceleration 1.58 and 6.40 G; max. neg. vel., 0.74 and 2.35 fps

* Gage not connected for this shot

Table 8

OPERATION TUMBLER, SHOT NO. 1 - AIRBLAST DATA

Station Number	Ground Range (ft)	Maximum Pressure (psi)	Arrival Time (sec)
			Main Airblast Shock
200	166	26.80	0.331
201	352	22.80	0.369
202	587	14.52	0.451
203	831	10.00	0.569
204	1077	10.86	0.717
205	1326	9.74	0.880
206	1575	7.84	1.053
207	1824	6.71	1.236
208	2073	5.23	1.425
209	2570	3[illegible]3	1.818
210	3069	2.47	2.225

Table 9

OPERATION TUMBLER, SHOT NO. 2 - AIRBLAST DATA

Station Number	Ground Range (ft)	Maximum Pressure (psi)	Arrival Time (sec)
			Main Airblast Shock
200	151	12.92	0.551
201	629	9.86	0.674
202	1376	6.24	1.063
203	2125	4.57	1.583
204	2875	3.52	2.162
205	3625	2.29	2.771
206	4375	1.89	3.395
207	5125	1.24	4.029
208	5875	1.07	4.673
209	7375	0.89	5.968
210	8875	0.48	7.273

Table 10

OPERATION TUMBLER, SHOT NO. 3 - AIRBLAST DATA

Station Number	Gage Code Number	Ground Range (ft)	Maximum Pressure (psi)	Arrival Time (sec)
				Main Airblast Shock
200	0B	166	11.18	1.708
201	1B	664	11.75	1.759
202	2B	1406	10.15	1.928
203	3B	2154	8.73	2.198
204	4B	2903	7.47	2.561
205	5B	3653	6.34	2.984
206	6B	4402	6.06	3.456
207	7B	5152	4.82	3.962
208	8B	5902	5.32	4.498
209	9B	7402	3.93	5.631
210	10B	8901	2.83	6.319

Table 11

OPERATION TUMBLER, SHOT NO. 4 - AIRBLAST DATA

Station Number	Gage Code Number	Ground Range (ft)	Pressure (psi)		Arrival Time (sec)	
			Precursor	Main Air-blast Shock	Precursor	Main Airblast Shock
200	0B	223	-	140	-	0.225
201	1B	605	q	p	q	p
202	2B	1344	8.1	26	0.483	0.585
203	3B	2091	7.6	m	0.904	m
204	4B	2840	-	8.3	-	1.431
205	5B	3589	-	6.35	-	1.972
206	6B	4338	-	4.62	-	2.538
207	7B	5087	-	3.75	-	3.126
208	8B	5837	-	3.02	-	3.728
209	9B	7337	-	2.04	-	4.962
210	10B	8837	-	1.51	-	6.222

m No distinct main shock.

p Gage 1B has three separate shocks;
arrival times, 0.284, 0.295, and 0.307 sec;
pressures, 26, 42, and 45 psi.

q Record not clear; possibly a precursor exists with arrival time of 0.245 sec., and pressure of 5.2 psi.

Table 12

OPERATION TUMBLER, SHOT NO. 4 - ARRIVAL TIMES

Station Number	Gage Code Number	Ground Range (ft)	Depth (ft)	Arrival Time (sec)		
				Direct Transmitted Wave	Precursor	Main Airblast Shock
200	0V	275	5	—	—	0.238
201	1V	626	5	—	—	p
202	2V	1354	5	—	0.491	m
203	3V1	2098	1	0.73	0.89	m
203	3V	2098	5	0.74	0.91	m
203	3V50	2104	50	0.74	0.93	m
203	3H	2098	5	0.73	0.925	m
203	3H50	*	*	*	*	*
203	3T	*	*	*	*	*
203	3T50	*	*	*	*	*
204	4V	2844	5	0.91	—	1.438
205	5V	3593	5	1.05	—	1.980
206	6V	4342	5	1.19	—	2.542
207	7V	5091	5	1.19	—	3.131
208	8V	5841	5	1.24	—	3.731
209	9V	7339	5	1.34	—	4.967
210	10V1	8838	1	2.11	—	6.226
210	10V	8838	5	1.47	—	6.228
210	10V50	8840	50	1.47	—	c
210	10H	8838	5	1.94	—	6.230
210	10H50	8840	50	1.84	—	c
210	10T	8838	5	1.93	—	6.237
210	10T50	*	*	*	*	*

c Earth wave and slap interfere; value uncertain

m No distinct main shock

p Gage 1V shows two shocks, arrival times, 0.295 and 0.314 sec.

* Gage not connected for this shot

(2) Comparison of Seismic Velocity with Test Velocity. As a means of comparing the velocity measured during a normal refraction seismic survey with the velocity of the groundshock wave from a nuclear explosion, time-distance curves were constructed using the published seismic velocities of the test sites. The time-distance curve was then shifted along the airblast arrival curve until the point of outrunning was determined. The results of this operation are presented in Figures 29 through 33.

The comparison of the predicted times of arrival of the outrunning ground waves with those actually observed for the Tumbler series of shots shows remarkable agreement. It should be noted that the range of overpressures for the Tumbler series is relatively low, varying between 138 and 2 pounds per square inch. Thus, at these pressures, the seismic survey velocities appear to be good approximations to use in predicting first arrivals for outrunning.

The comparison shown in Figure 30, using the Shot Priscilla data, was not conclusive since outrunning did not occur at the test stations. A comparison of the velocities calculated from the arrival of the peak pressure wave at the gages between the surface and a depth of 50 feet at Frenchman Flat at presumably the 100 pounds per square inch level and those measured by a refraction seismic survey is reported by Sauer (11). The velocity of the peak stress wave is shown to be between 2/3 and 3/4 of that measured by the seismic survey.

A survey made after Shot Priscilla showed no permanent displacement below overpressures of about 40 pounds per square inch. Permanent displacement of course, would imply inelastic behavior of the soils.

In contrast to the dry, desert type playa soils of Frenchman and Yucca Flats at the Nevada Test Site, the soil conditions of the Pacific Proving Grounds are saturated coral sands and coral conglomerate. Typical of the coral atoll of the Eniwetok Proving Grounds, site of Shot Koa and Cactus, is a surface layer 5 to 7 feet thick of dry, loose coral sand and broken shells. The seismic velocity of the surface layer is approximately 800 feet per second. The surface layer is underlain by the water surface, and, in places, by a very hard layer, several feet thick, of cemented coral conglomerate. The seismic velocity of the conglomerate is on the order of 8,000 feet per second. Below the water table the sites are underlain by alternating, random, and discontinuous layers of loose to dense coral sand and shells, and other remnants of cemented coral conglomerate shells. The velocity of the saturated sands is on the order of 5,000 feet per second.

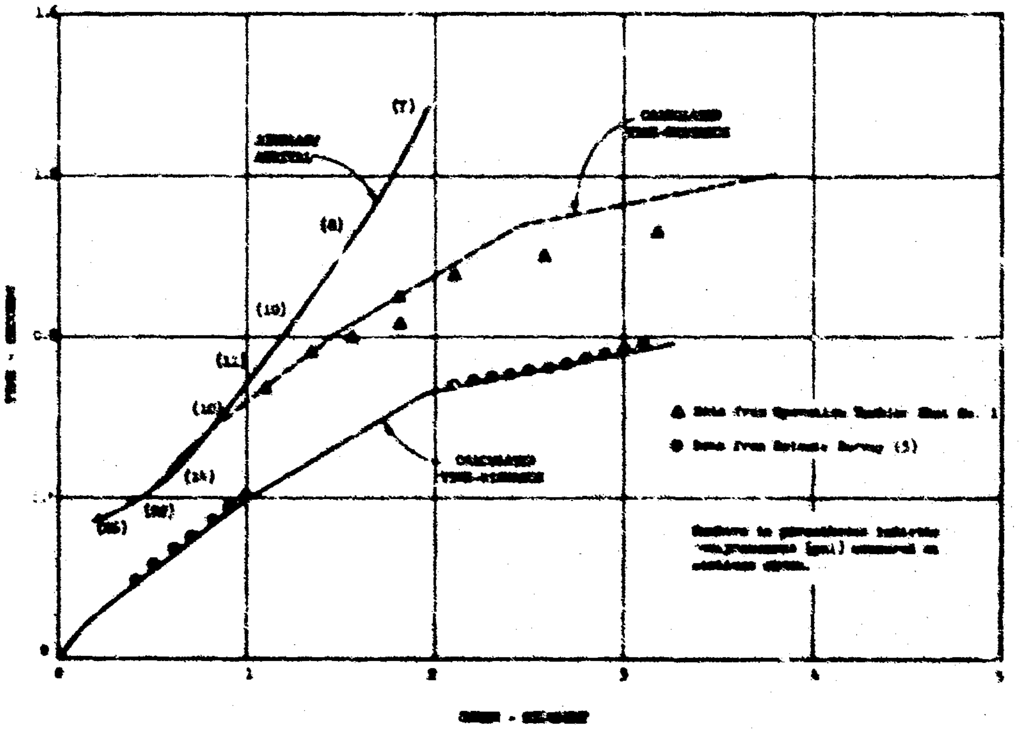

Figure 29. Comparison of Field Data with Calculated Time-Distance Curve, Operation Tumbler, Shot No. 1.

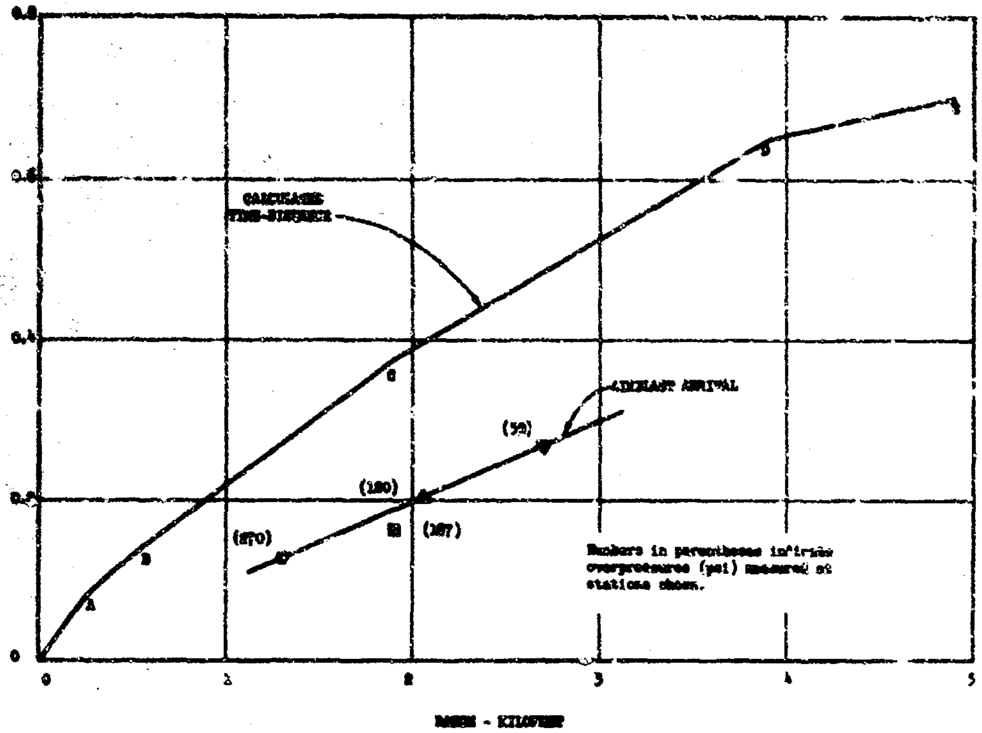

Figure 30. Comparison of Field Data with Calculated Time-Distance Curve, Operation Plumbbob, Shot Priscilla.

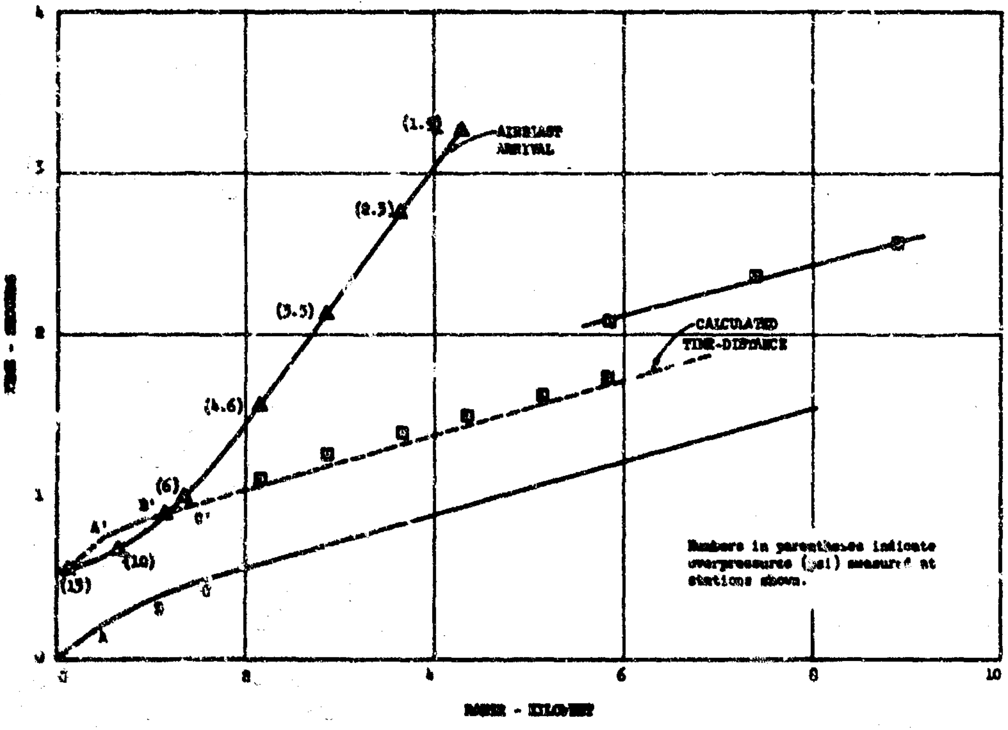

Figure 31. Comparison of Field Data with Calculated Time-Distance Curve, Operation Tumbler, Shot No. 2.

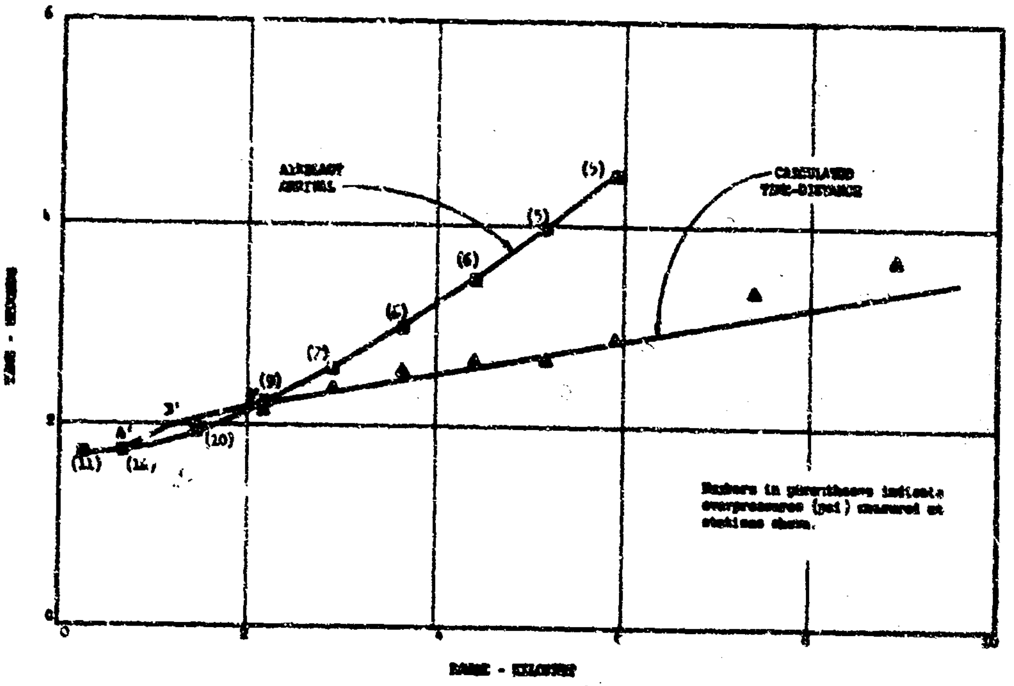

Figure 32. Comparison of Field Data with Calculated Time-Distance Curve, Operation Tumbler, Shot No. 3.

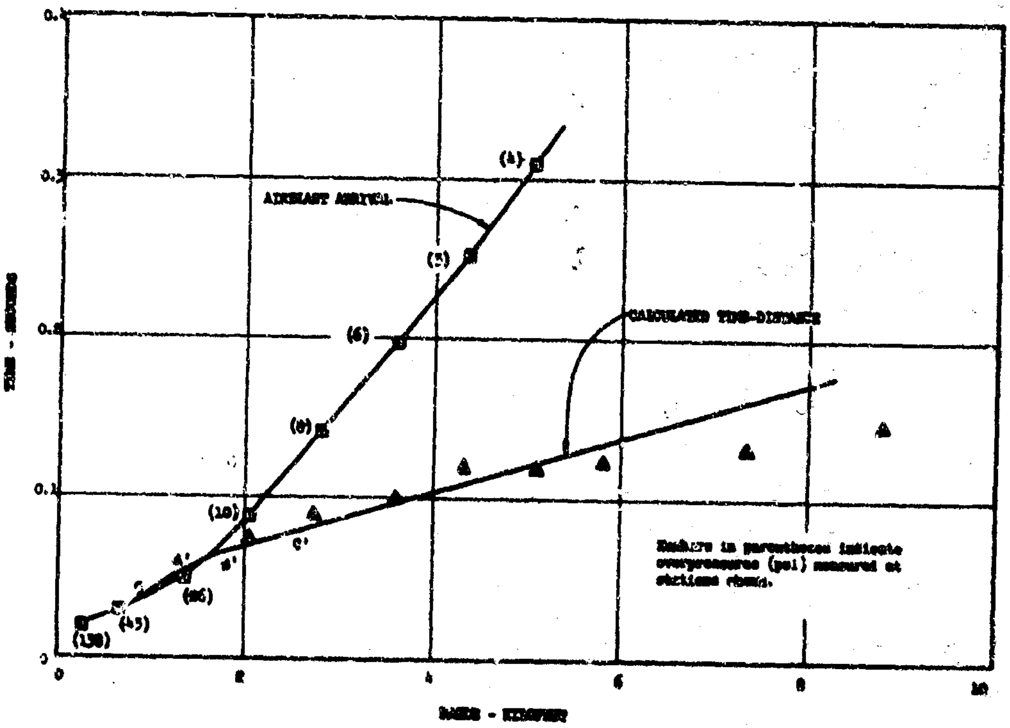

Figure 33. Comparison of Field Data with Calculated Time-Distance Curve, Operation Tumbler, Shot No. 4.

The test shot for Koa was arranged so that the first gages recording groundshock were located at stations where the overpressures were about 1000 pounds per square inch. Gages were also located at stations which would receive overpressures of about 100 pounds per square inch.

The significant feature of the ground motions for Shots Koa and Cactus was that the waveforms had the character of the refracted wave, but of large amplitude, (Figures 3 and 4). The velocities of these very strong waves were slightly higher than measured by the refraction seismic surveys at the respective sites (14).

It is probable that the hard coral conglomerate acted nearly elastically, as perhaps did the saturated coral sands. Although the final result of the pressure and vibrations on the saturated, loose coral sand was densification, this may not have occurred until the water had time to drain from between the sand grains. As a result, the sand-water system may have acted elastically during the passage of the first high intensity waves. This possibility may also explain why the maximum displacement did not occur until a time after the entire airwave had passed over the recording stations.

The inelastic behavior of a soil would be most evident when a large change in stress occurs relative to the initial stress of the soil. Considering, for a typical site that is not saturated, that the vertical stress due to the overburden is about 0.9 pounds per square inch per foot of depth, at depths on the order of 100 to 200 feet, the soil is initially stressed to and under equilibrium at pressures of 90 to 180 pounds per square inch. The overpressures at the ground surface, considering attenuation of stress with depth, may have to be much higher than the initial stress of the soil before the velocity of the ground waves is significantly reduced by nonlinearities.

The velocity at which soils below the water level transmit a high stress wave would be close to that of the seismic velocity of water. Thus the velocity of a saturated soil as measured during a seismic survey would seem to be a good approximation to use in constructing a wavefront diagram.

Sauer (16) suggests that in predicting peak amplitudes of ground motion three fourths of the seismic velocity for soils and fractured rock should be used. Based upon the evidence shown by the comparison of the predicted arrival time of the refracted wave and that actually measured during the weapon tests, it would seem reasonable to use the three fourths reduction for dry soils at overpressures over 40 pounds per square inch; and for the case of saturated soils, rock, and perhaps soil at depths greater than 200 feet, to use the velocity as measured by a seismic survey.

(3) Comparison of Predicted Arrival Times and Direction of Motions with Test Acceleration Waveforms. To demonstrate the manner in which the contours of equal arrival time (Figures 19 through 23) may be combined with the time-distance curves (Figures 26 through 28) to yield arrival times and directions of motion, and as an indication of the validity of the predictions, test data from Operation Tumbler, Shot No. 1, are compared with the predicted motions in Figures 34, 35 and 36. At the top of each figure, acceleration waveforms, recorded at Stations 3 and 5, are reproduced here from Reference 12. The station number and direction of motion are indicated by the symbols near the vertical scale; that is, "3V" denotes that the record was taken at Station 3 and that the vertical motion was measured. The letter "H" indicates horizontal motion while tangential motion is labeled "T". The lower charts, characterized

by the arrows, show the predicted arrival times of the refracted, direct and reflected waves and their directions of motion.

Subsequent to the earliest arrival of each wave indicated by the arrows, the motion continues as long as the disturbance remains. The position of the arrows after the first arrival therefore is somewhat arbitrary and is indicative only of the general motion at these later times. The intensity of the motion varies as the intensity of the source changes. However, the lengths of the arrows shown in the figures are not intended to indicate relative strengths of the waves.

The time of arrival of the first of each type of wave can be determined directly from the contours of Figures 19 through 23. Knowing the range from the source, the direction of motion of refracted waves will be normal to the refraction wavefront at that range as shown in Figure 27. From Figure 28, the direction of motion of reflected waves can be found in a similar manner.

If contours of equal arrival time have not been plotted for the site and weapon conditions, the same results can be obtained from time-distance curves such as that shown in Figure 26. This figure was employed in predicting the arrival times shown in Figures 34 and 35 for Station 3. By sliding the origin of the time-distance curve along the airblast arrival curve in the same manner that the point of outrunning is located, the total time required for each wave to travel a given range may be determined. It will be found to be faster, however, to draw contour maps of equal arrival time. In either case, the direction of motion is obtained by the use of the appropriate wavefront diagram as before. It should be noted that time-distance curves must be constructed for horizontal planes passing through the point of interest.

The geologic model used in this comparison was modified somewhat from the test data in order to simplify the calculations and in an attempt to correct for the lower effective velocity of the surface layer while loaded by the overpressure. The velocity profile used appears on Figure 28. In reality, the seismic velocity profile measured in a boring by Shannon and Wilson (3) indicated the existence of a layer with a velocity of 2500 feet per second sandwiched between the two surface layers with a velocity of 1500 feet per second. As shown in Figure 13, when such a condition exists the reflected energy from the next deeper high-velocity layer is nearly as high as that from the first high-velocity layer.

The presence of this 2500 feet per second layer may account for the apparently late reflection arrivals, since this layer was not included in the construction of the wavefront diagram and other curves.

There appears to be reasonably good agreement between the arrival times and between the phasing of the vertical motion with the horizontal motion. It appears quite clear, in the cases shown, that the first arrivals of the refraction wave do not carry much energy in relation to the direct wave and early reflections. At later times, when energy is arriving from many sources, the waveform could be expected to have a widely fluctuating pattern. Relatively minor changes in the sequence of stratification would significantly alter the pattern.

The negative (downward) acceleration occuring near t = 0.8 seconds (Figure 36) is not indicated in the diagram as being initiated by the arrival of a wave. Not all waves, of course, have been included in the diagram. Shear waves, plastic shock fronts, and reflections due to the impingement of the refracted waves on the ground surface, for example. have not been represented on the time-distance curve although some greater detail could have been shown if desired.

It is more likely, however, that the full cycle oscillation of the acceleration curve is due to the relatively short duration of the airblast-loading which generated the refraction. At the range at which the refracting wave was initiated, the time of decaying of the overpressure to fifty percent of its peak value was less than 0.10 seconds. The rapid decay of the pressure would propagate as a family of expansions which would account for the oscillation but which have not been shown on the time distance curve.

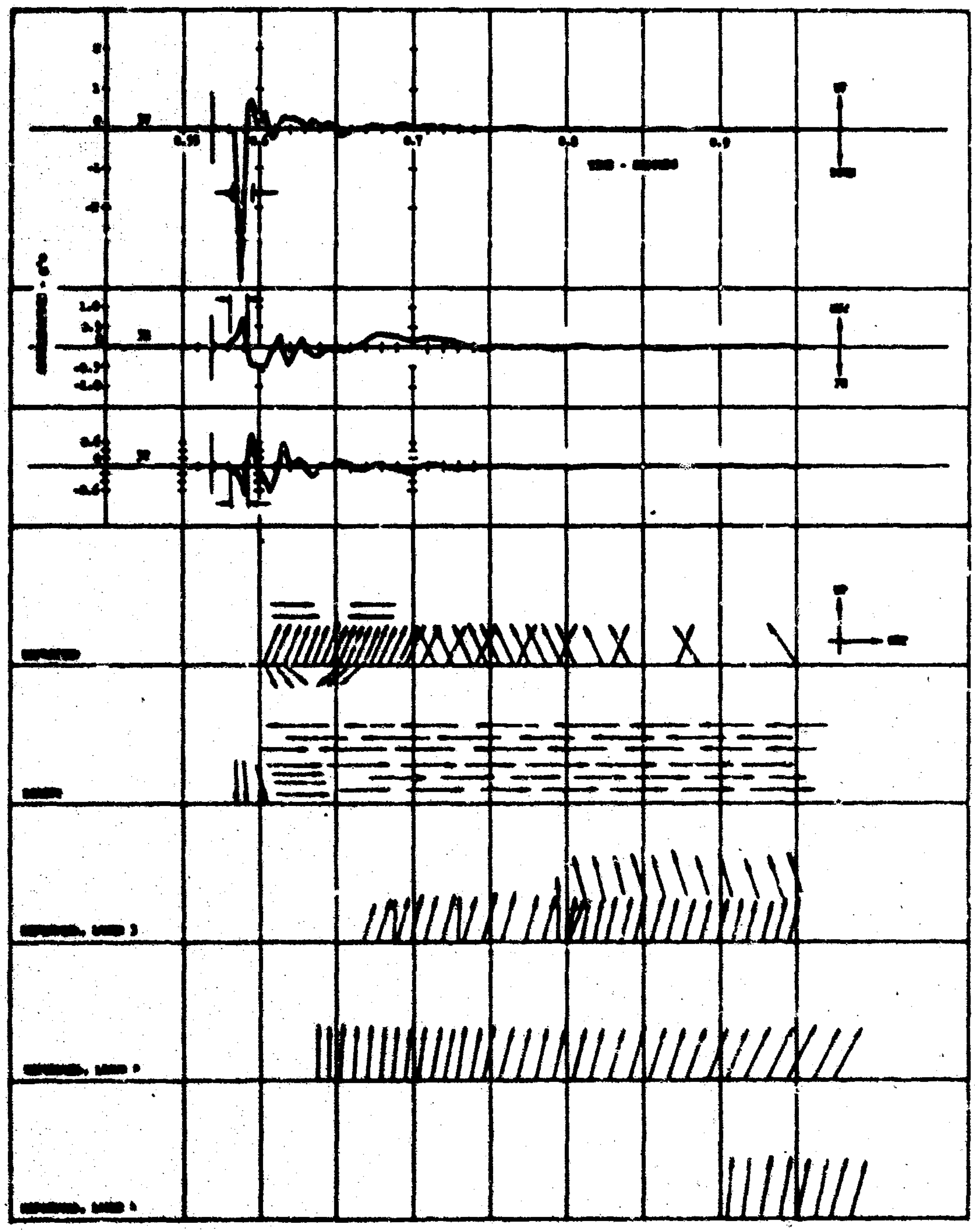

Figure 34. Predicted vs. Measured Arrival Times and Directions of Motion, Operation Tumbler, Shot No. 1, Stations 5V, 5H, 5T, Depth 5 Feet, Range 845 Feet.

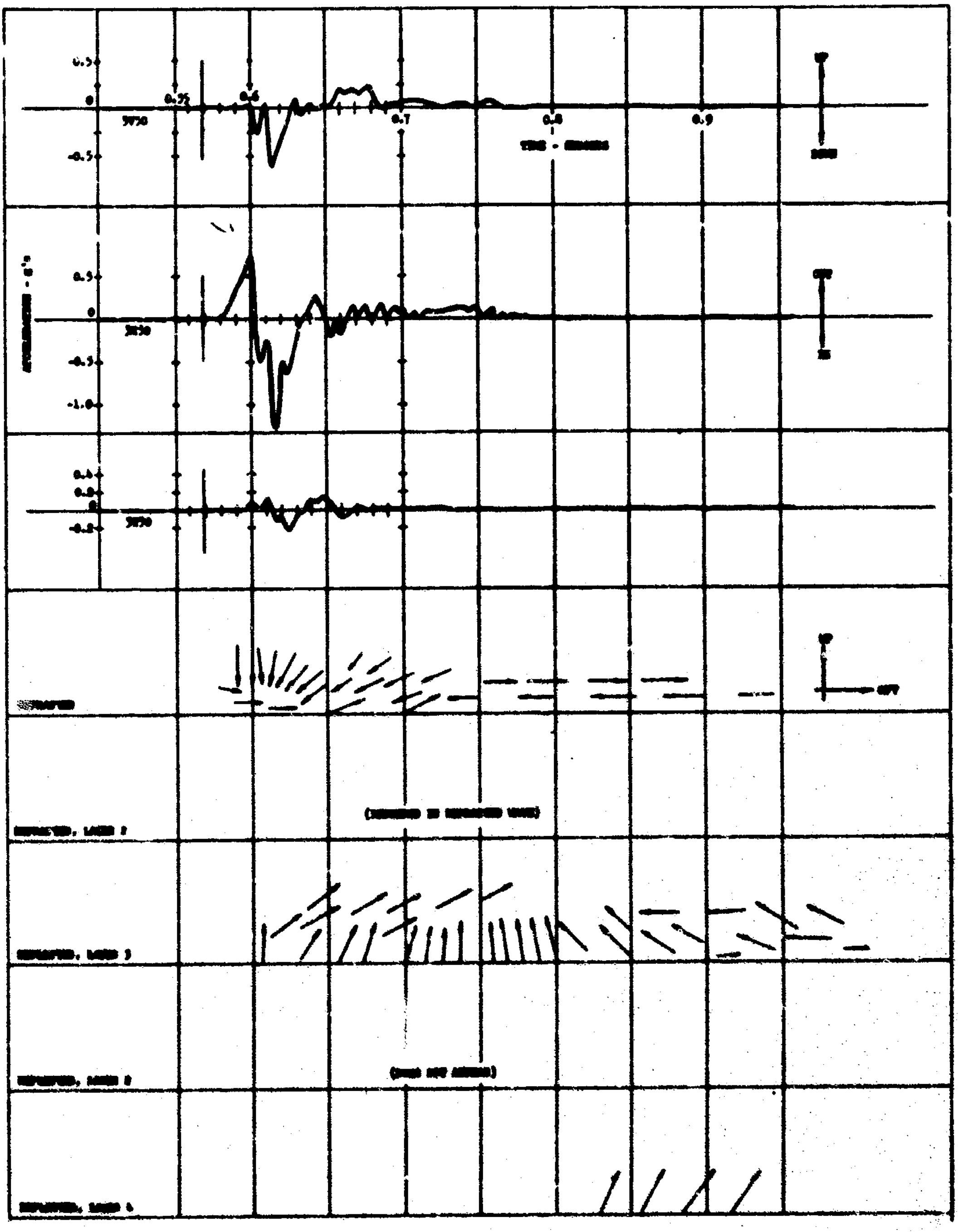

Figure 35. Predicted vs. Measured Arrival Times and Ground Motions, Operation Tumbler, Shot No. 1, Stations 3V50, 3H50, 3T50, Depth 50 Feet, Range 861 Feet.

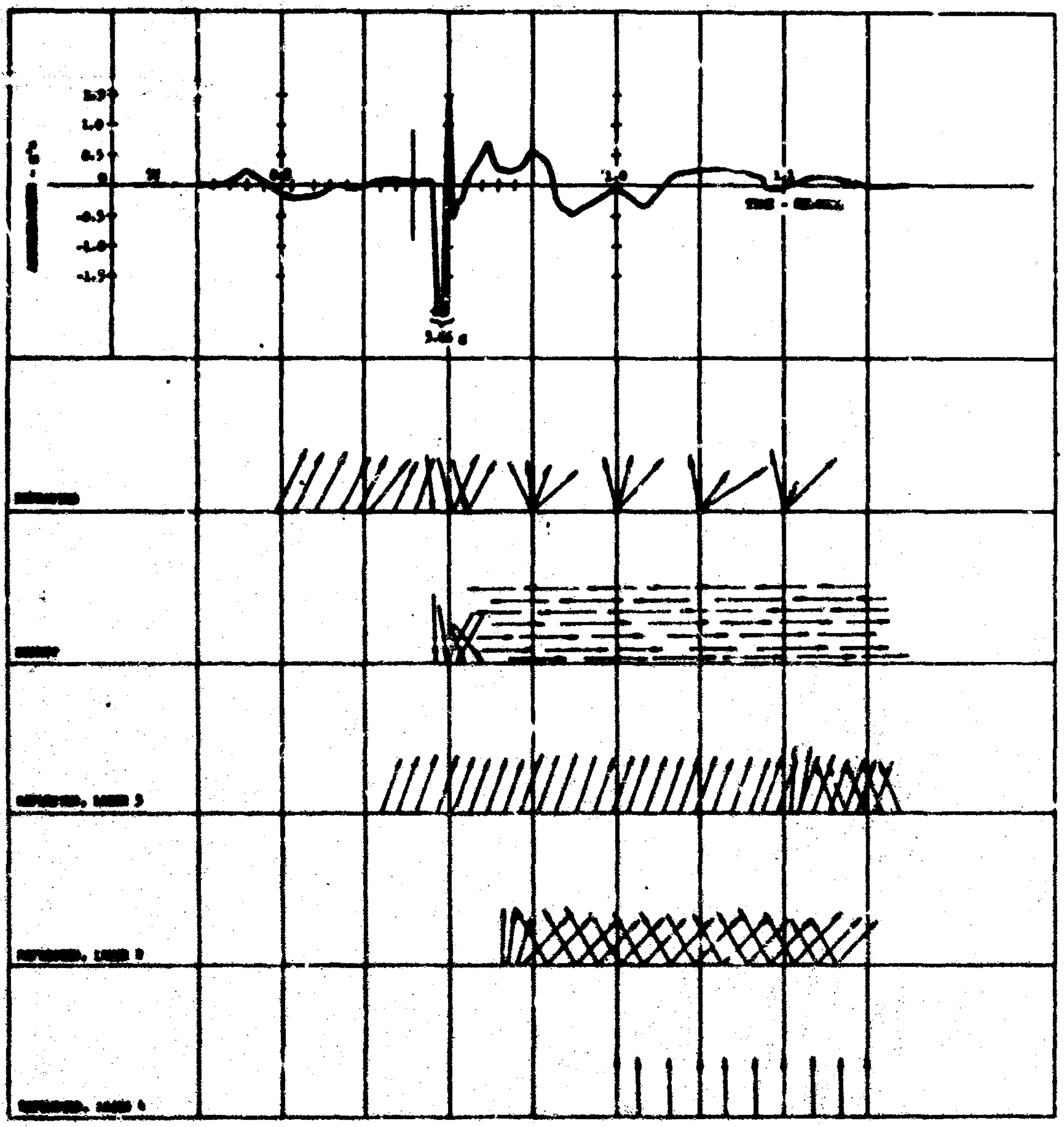

Figure 36. Predicted vs. Measured Arrival Times and Ground Motions, Operation Tumbler, Shot No. 1, Station 5V, Range 1535 Feet.

Although the first reflections from lower layers to arrive at the station come from sources varying widely in range and overpressure, the work of Gutenberg (11) shows that the close-in sources contribute the largest percentage of energy even though they may not represent reflections of rays flatter than the critical angle.

No quantitative estimates can be made regarding the energy associated with the various waves. The evaluation of the stress at a point by spatial dispersion using the relationships of Boussinesq or Westergaard have been applied to given areas upon which the load intensity varies with time. This approach may be feasible for gross low-frequency characteristics of the waves, but probably would not reveal the detail needed in this application.

D. Conclusions. The wavefront diagram is a useful and simple means for predicting certain waveform parameters of importance to shock isolation system design. If the site geology is known in reasonable detail, the type of wave first arriving at the point of interest, the first arrival times of waves due to the airblast, those transmitted directly from the source, and those reaching the point of interest by reflections or refractions from underlying layers can be estimated with good accuracy. Thus, the time differences between the arrivals of the various waves can be determined.

Nonlinearities in the stress-strain relationship of the soil are of little importance in calculating the arrival time of the first wave to reach the point of interest, as the wave will travel at the seismic velocity of the undisturbed medium. For subsequent waves, it is found that the initial state of stress at depths where high-intensity waves from large yield weapons would be reflected or refracted is usually sufficiently high so that the soil modulus remains fairly constant. Therefore, in regions outside the rupture zone, it is probable that the waves will travel at velocities nearer to the measured seismic velocity than to those which might be predicted on the basis of an initially unstressed medium.

On the basis of comparisons of the predicted arrival times of refracted waves with those measured during several weapons tests, it appears to be reasonable to base calculations on a wave velocity equal to three fourths of the measured seismic velocity for dry soils and pressures in excess of 40 pounds per square inch. For saturated soils and rock and for all types of soil formations at depths greater than 200 feet, the use of the measured seismic velocity appears to yield good correlations with NTS and EPG data.

In Reference 1, it was suggested that the Type II wave was the effect of an interaction of the airblast wave with waves refracted from lower surfaces. However the present study has shown that relatively small amounts of energy are carried back into the upper layers by refracted waves. Instead, it is the reflections which are primarily responsible for the return of energy from a lower to an upper layer.

For this reason it is recommended that the normal refraction survey made during site evaluation be supplemented with a reflection seismic survey of the area near the proposed facility location. The refraction survey will yield data which can be used directly in the construction of the wavefront diagram as described earlier in this section. Data from the reflection seismograms will not only be of value in constructing the wavefront diagram but should also assist in evaluating the relative amplitudes of the reflections from lower layers.

Further, while the airblast-induced wave may contribute to the oscillatory nature of the Type II wave, combinations of refractions, and reflections, with the direct compressional and expansion waves can produce oscillations without the necessity for the presence of the airblast-induced component.

From the wavefront diagram and supporting calculations the direction of each wave reaching the point of interest from each of the sources can be determined and, with certain assumptions, the energy in each ray grossly approximated. It is evident from the preceeding discussions, however, that the total number of waves emanating from each source is very large. In the examples only the simplest of the compressional body waves have been considered, the loading function has been assumed to be invariant with time, and shear and surface waves have been neglected entirely. While propagation of all of these phenomena could be included in the time-distance curve and wavefront diagrams could be drawn, the fact that only the roughest estimates can be made of the time-history of the motion due to each of the waves severely restricts the usefulness of this graphical method for predicting the waveform of the Type II ground motion.

Nonetheless, the wavefront diagram and the time distance curves can be useful tools in providing a simple means for better visualizing the routes by which certain waves reach the point of interest and for determining quantitatively some important time parameters of the composite waveform. One simple application which has been used extensively in the past is that of determining the time interval between the arrivals of the Type I airblast-induced wave and the Type II oscillatory component. The interval between the arrivals of the first refraction and the first reflection can also be estimated with fair accuracy. These data together with, say, a triangular representation of the moving airblast loading permit the gross calculation of the relative strengths of these early motions.

If, as in many cases it is, the response spectrum of the total motion of the ground as determined by current groundshock prediction techniques is provided as a criterion of the strength of the motion in a given application, the problem of synthesizing acceptable time-histories of the ground motion is reduced appreciably. As the arrival time and [illegible] strength and form of the airblast-induced motion can be estimated with good accuracy, and as the arrival times of reflections, refractions and other waves as desired can be obtained from the time-distance curve, only the relative strengths of these latter waves must be estimated, as the response spectrum of the composite wave must match the given spectrum. Obviously a great deal of intuition is involved in assigning even relative strengths, but at least this method provides a broad guideline for constructing the Type II oscillation which heretofore has not been available. And furthermore, the resulting waveform will reflect the influence of the particular site and weapon parameters.

The directions and phasing of the strong early motions is of vital importance in the design of many hardened structures, in particular those extending to or above the surface of the ground. Here, owing to the lack of appreciable stiffness in the upward direction, the phasing between upward and downward outrunning ground motions and between these motions and the arrival of the airblast wave can have a significant influence on the response of the structure. Again, while the strength of the motions can only be approximated grossly, the range of phase relationships of the first arrivals can be obtained directly from the time-distance curve.

It is clear that a wavefront diagram, time-distance curve or other highly simplified graphical means cannot be expected to yield accurate, detailed time-histories of a phenomenon as complex as the propagation of nuclear blast generated waves in an inelastic, stratified half-space. In the absence of further atmospheric nuclear testing, more accurate solutions must come from comprehensive analytical treatments supported by experiment. However, until the results of such solutions become available in a form which will permit the engineer readily to construct waveforms directly applicable to the site and weapon conditions of interest to him, these graphical techniques, qualitative as they may be, offer vitally needed assistance.

3. THEORETICAL ANALYSIS OF GROUNDSHOCK WAVEFORMS.

A. Background. Body waves generated in an infinite or semi-infinite homogeneous, elastic, undamped medium by the action of a disturbance applied suddenly at a point do not exhibit oscillatory motions unless the disturbance itself is oscillatory. In any case, the input wave is propagated throughout the medium unchanged in form. In seeking an explanation for the oscillations reported in Reference 1, possible deviations from these ideal conditions therefore were investigated.

In Section 2, the possibility was examined that the oscillatory nature of the observed waves (Figure 2) was due to the superposition of waves arriving at the point of interest from a common source, but by different routes. Although except for the very early motions, quantitative correlations could not be obtained, it was shown that nonuniformities in the site properties are undoubtedly responsible to a large if not major extent for the oscillatory nature of the Type II wave. Nonhomogeneity of the site, however, is not the only possible cause of irregularity in the waveform. The energy transmitted to the ground by a surface burst of a nuclear weapon is not steady either in space or in time. The airblast wave moving outward from the point of burst varies in strength and in waveform, and as it is continuously imparting energy to a nonlinear medium, deviations from the initial pulse shape will be generated.

Damping characteristics of the soil might also lead to oscillations. For example, the theory is advanced in Reference 17 that a sharp seismic disturbance in a homogeneous half-space gives rise to a traveling wavelet of a shape determined by the nature of the earth's absorption spectrum for elastic waves. It is shown that seismograms can be duplicated by successions of these wavelets generally overlapping but sometimes in the clear. It was further shown that the center of the wavelet travels with a velocity characteristic of the medium and that the wavelet broadens as it propagates outward from the source. While this phenomenon may not be of principal significance either here or in seismograms, it does serve to indicate the variety of effects which may lead to oscillations.

A further possibility is that the oscillations are not due entirely to body waves but that they also include motions due to surface waves of the Rayleigh type. The strengths of the oscillations due to surface waves would be expected to be greatest at the near-surface locations at which the Type II waves were measured. This possibility was investigated here and Rayleigh wave motions resulting from loading patterns typical of those generated by nuclear blasts were examined.

In Reference 18, previous studies of magnitudes and forms of Rayleigh waves generated by nuclear-burst-type loading functions are reviewed. The complete solution for stresses and displacements produced by a suddenly-applied concentrated load with a step distribution in time has been treated by Pekeris and Lifson (19). The portions of these quantities which are due to Rayleigh effects were extracted from these results by Chao, Bleich, and Sackman (20) as the contribution of certain poles in the inversion integrals of the Pekeris solution. Baron and Lecht (18) extended this work, considering the Rayleigh effects due to a decaying pressure pulse of uniform strength acting over a circular surface area of increasing radius.

In this study, the loading function was further modified to include a very strong initial pulse which is more nearly representative of the high yield nuclear blast. A load of varying magnitude and waveform was considered to move across the interface of an elastic, homogeneous, isotropic half-space. The ground motion due to Rayleigh waves alone was calculated for shallow depths at various ranges, and the equations for the body waves at depths directly below the center of burst were derived. The oscillatory nature of the Rayleigh waves was examined and their strengths compared with the form and strength of the airblast induced groundshock.

B. Mathematical Model.

(1) Assumptions. It was assumed that the half-space is homogeneous and elastic. The pressure due to a surface burst of a nuclear weapon was represented as an instantaneous point loading followed by a

radially expanding ring or circular line loading of high intensity with the loading within the ring being of relatively low intensity. The radial velocity of the loading front was assumed to be inversely proportional to the square root of the time. Only the effect of normal pressure on the surface of the half-space was considered.

(2) Simplified Analysis. The expanding ring loading or blast wavefront of high intensity was based on data given in Reference 21 for a 20 megaton weapon and reproduced here as Figure 37. Here the radial distances traveled by the wave and the peak pressures are given for six locations of the wavefront. In converting these data to a more amenable form for use in the analysis, they were first approximated by a ring of uniform, but time-varying distribution, of total force S_o, and a ring with a parabolic distribution, representing the steep wavefront, of total force S_1 (Figure 38). The parabolic ring was further simplified by expressing it as a Delta function traveling with a velocity inversely proportional to the square root of the time. The expanding circular area loading was approximated by a Heaviside step function (Figure 39).

The circular line ring loading front was assumed to travel slower than the area loading front since the resultant force of the former is at a distance $d_r/4$ behind the leading edge of the latter.

In Table 13 the data of Figure 37 have been tabulated and several significant parameters calculated. It is seen that the ratio of S_1/S_o is fairly constant for the range of primary interest and was thus fixed at 0.3. Moreover, the product $P_o = S_o d$ is also seen to be reasonably constant, averaging about 12 x 10^{15} pound feet.

Table 13

LOADING PARAMETERS BASED ON CURVES OF FIGURE 37

t (m.s)	d (ft)	d_r (ft)	p_1 (kpsi)	p_o (kpsi)	S_o (lb x 10^{12})	S_1 (lb x 10^{12})	S_1/S_o	$S_o d$ (lb ft x 10^{15})
6.4	1110	430	64	27	15	4.8	0.32	16.5
14.6	1570	470	24	8	8.9	3.3	0.37	14.0
18.9	1710	530	17.5	5	6.6	3.1	0.47	11.3
42.0	2360	660	6.6	2	5.0	2.0	0.39	11.8
122	3560	900	1.8	0.57	3.3	1.1	0.34	11.8
291	5040	1120	0.7	0.22	2.5	0.8	0.31	12.7

To evaluate the wavefront velocity, let the velocity

$$v = \sqrt{a/t}$$

where

a = wavefront velocity coefficient

t = time

Then the distance, d, is

$$d = 2\sqrt{at}$$

and

$$a = d^2/4t$$

Similarly,

$$a_1 = d_1^2/4t$$

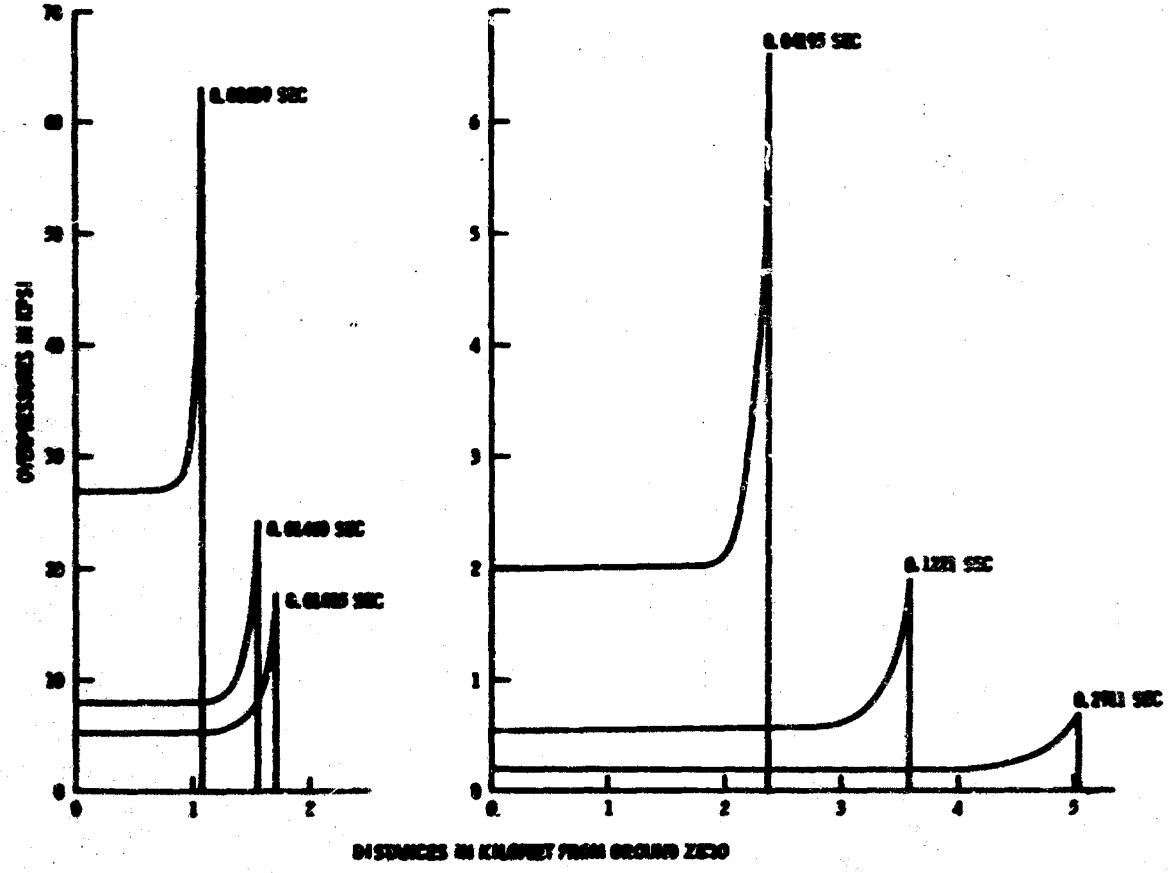

Figure 57. Space Plots for Blast Wave from a 20 MT Surface Burst at Various Times after Detonation (21).

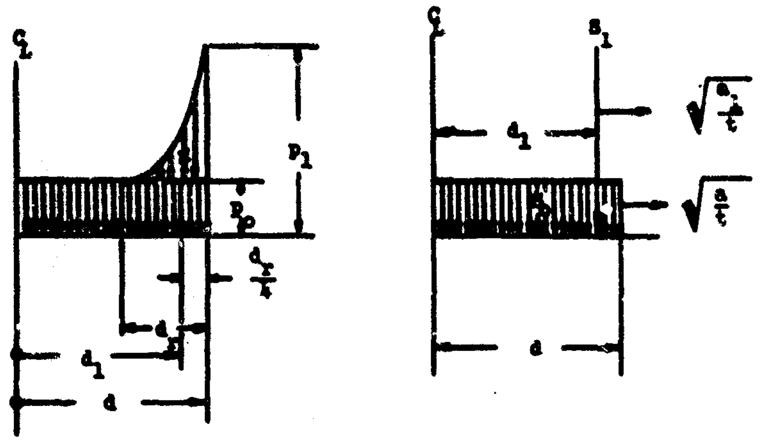

Figure 38. Simplified Parabolic Ring and Uniform Circular Loading.

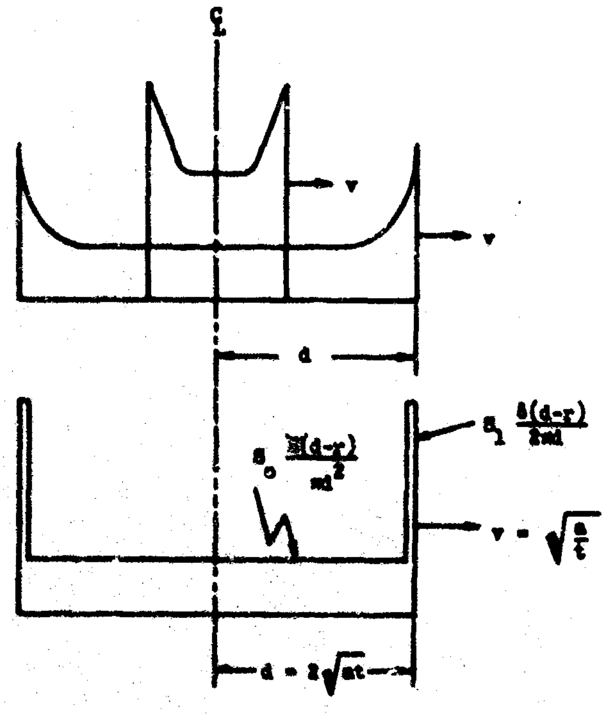

Figure 39. Loading Functions used in Computer Program.

where a_1 is the wavefront velocity coefficient for the ring loading wave. The coefficients a and a_1, based on the data of Figure 37 are presented in Table 14.

Table 14

EVALUATION OF WAVEFRONT VELOCITY COEFFICIENTS a AND a_1 (FROM FIGURE 37)

t (ms)	d (ft)	d_r (ft)	d_1 (ft)	a (ft^2/sec x 10^6)	a_1 (ft^2/sec x 10^6)
42	2360	660	2190	33	28
122	3560	900	3330	26	22
291	5040	1120	4760	22	19

The average of a is about 25 x 10^6 square feet per second (Figure 40) while the value of a_1 might be taken about 20 x 10^6 square feet per second. However, in view of the indicated trend of the center of the ring loading to lag more and more as time advances, the value for a_1 used in the computer solution was taken as only 60 percent of that for a. Thus,

$$a_1 = 0.6\ a$$

As a first approximation, only the vertical component of the Rayleigh wave was considered for stations away from the loading zone and near the surface. Stations at those locations are referred to as Region I, (Figure 41). For stations located directly under the loading zone and deep underground, the radial horizontal projection r was assumed to be small in comparison with the depth, z. For these stations, Region II (Figure 42), the vertical particle velocity is the quantity of interest.

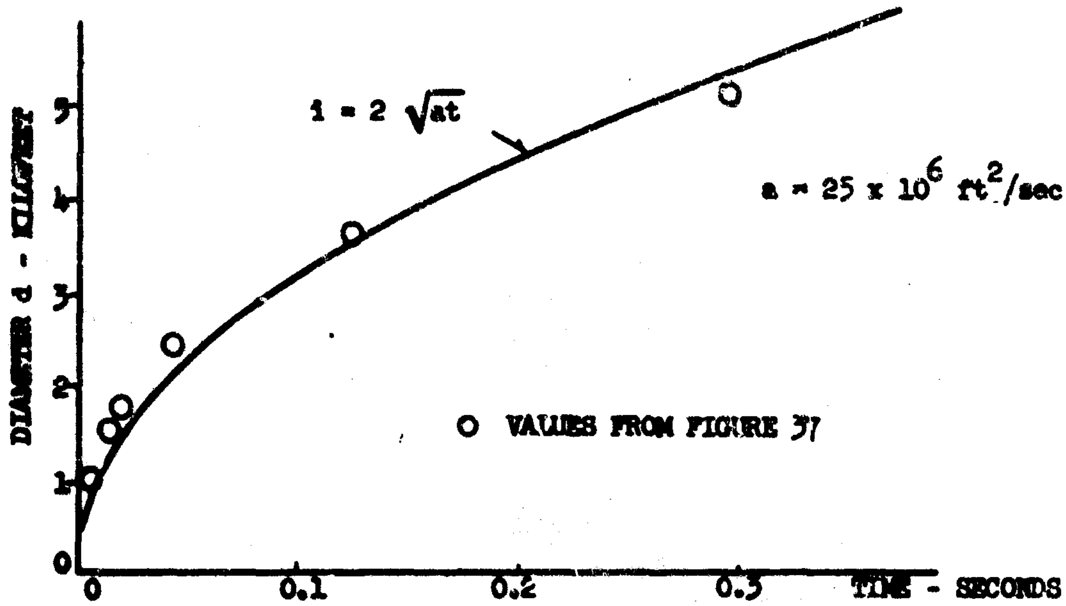

Figure 40. Comparison of Wavefront Velocity of Figure 37 with Simplified Value Where $a = 25 \times 10^6$ ft^2/sec.

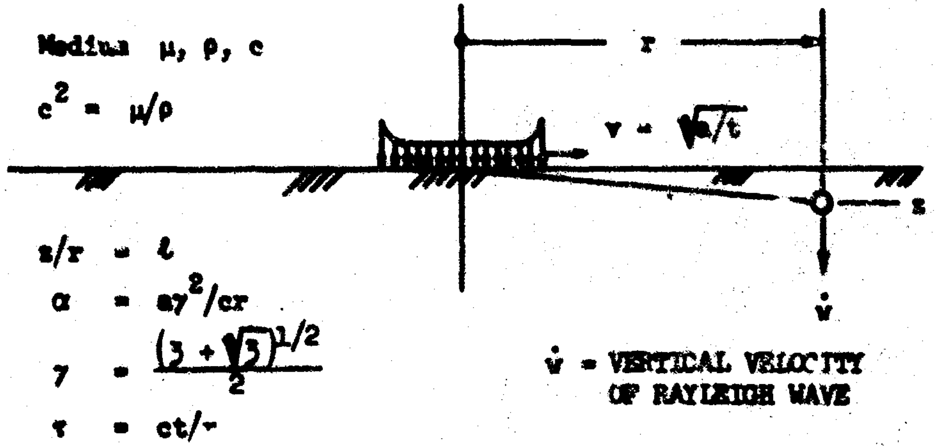

Figure 41. Location of Sites in Region I Relative to Load Source.

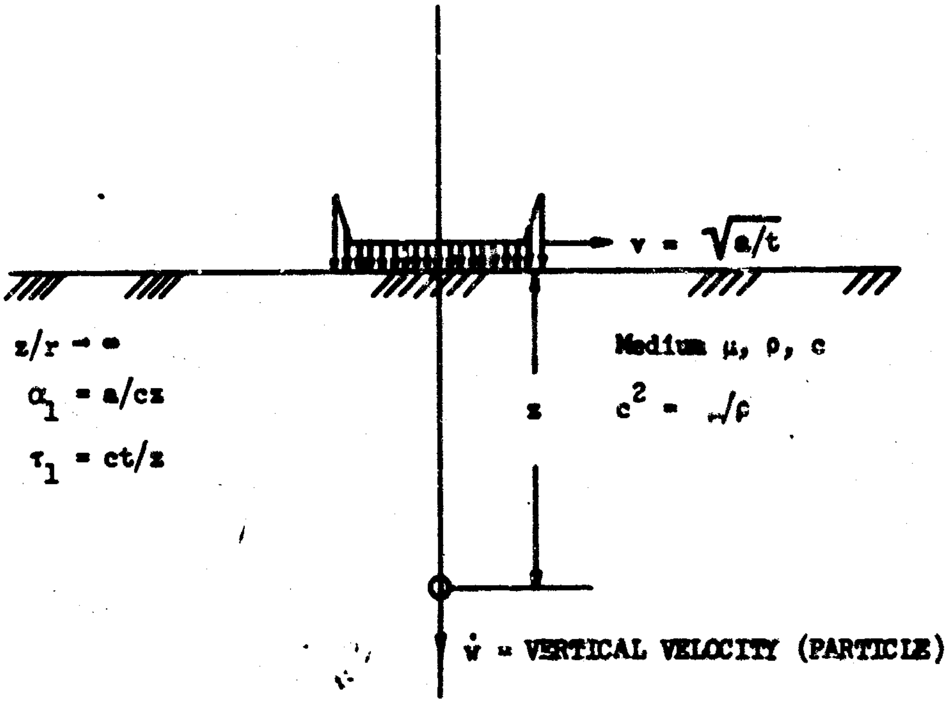

Figure 42. Location of Sites in Region II Relative to Load Source.

(3) Log of Computed Curves. For Region I, the vertical velocity component of the Rayleigh wave is given by Equation 34, (Appendix B). The dimensionless velocity coordinate η is defined:

$$\eta = \frac{16\pi r^2 \mu}{cS_o} \frac{2\dot{w}}{\sqrt{3\gamma^2 - 1}} = \frac{2\pi r^2 \mu}{cS_o} 10\dot{w} = 62.8 \frac{r^2 \mu \dot{w}}{cS_o}$$

In presenting the results of the calculations, η has been plotted against the dimensionless time

$$\tau = ct/r$$

for the dimensionless depth ratios

$$\ell = z/r = \begin{cases} 0.001 \\ 0.010 \end{cases}$$

for the dimensionless "spike ratio"

$$\frac{S_1}{S_0} = 0.3$$

(this ratio is fairly constant throughout the range covered by Figure 37 and listed in Table 13), and for the dimensionless "softness" levels, α, where α has been interpreted as a "softness" and/or location level. An increase in α indicates that the medium becomes softer, or if the softness is unchanged as the range of the site from ground zero becomes less.

In the following tabulation, the figures in which the results are plotted for various values of α_{so} and ℓ are shown.

$$\alpha_{so} = a\gamma^2/cr \left\{ \begin{array}{l} \left. \begin{array}{lll} 0.1 & \text{Hard,} & \text{Figure } 45 \\ 0.3 & \text{Hard-Soft,} & \text{Figure } 46 \\ 0.5 & \text{Soft-Hard,} & \text{Figure } 47 \\ 1.0 & \text{Soft,} & \text{Figure } 48 \end{array} \right\} \ell = 0.001 \\ \\ \left. \begin{array}{lll} 0.1 & \text{Hard,} & \text{Figure } 49 \\ 0.3 & \text{Hard-Soft,} & \text{Figure } 50 \\ 0.5 & \text{Soft-Hard,} & \text{Figure } 51 \\ 1.0 & \text{Soft,} & \text{Figure } 52 \end{array} \right\} \ell = 0.010 \end{array} \right.$$

For Region II, the vertical particle velocity component is expressed by Equation 48, but numerical calculations have not been made.

C. Discussion of Equation. The parameter α has been described as an index of "softness" of the medium through which the wave travels. However, it can also be shown to indicate whether the point of interest lies in a subseismic or a superseismic region. By definition

$$\alpha = \frac{a\gamma^2}{cr} \tag{12}$$

But

$$a = \frac{d^2}{4t} = \frac{vd}{2}$$

then

$$\alpha = \frac{\gamma^2}{2}\left(\frac{v}{c}\right)\left(\frac{d}{r}\right)$$

The shear wave velocity c can be related to the dilatational wave velocity c_p by the expression

$$c = c_p\sqrt{\frac{1 - 2\nu}{2(1 - \nu)}}$$

and when Poisson's ratio ν is 0.25, $c = 0.577\ c_p$. γ has been given previously as

$$\gamma = \frac{1}{2}\left(3 + \sqrt{3}\right)^{1/2} = 1.08$$

then

$$\alpha = \frac{1.17}{1.15}\left(\frac{v}{c_p}\right)\left(\frac{d}{r}\right) = \left(\frac{v}{c_p}\right)\left(\frac{d}{r}\right)$$

For a homogeneous medium, the transeismic point is defined as the location at which the blast wave velocity is equal to the dilatational wave velocity, that is, where $v = c_p$. Then at this point

$$\left(\alpha\right)_{v = c_p} \sim \left(\frac{d}{r}\right)$$

In the cases considered here responses have been evaluated for $\alpha_{so} = 0.1$, 0.3, 0.5 and 1.0. In the first three cases, then, the point of interest lies well beyond the transeismic point while in the last case the point of interest coincides with the transeismic point.

Similarly, α can also be expressed in terms of the Rayleigh wave velocity, c_r. Then since $c_r = c/\gamma$,

$$\alpha = \frac{\gamma}{2}\left(\frac{v}{c_r}\right)\left(\frac{d}{r}\right)$$

and when $v = c_r$

$$\left(\alpha\right)_{v = c_r} = \frac{\gamma}{2}\left(\frac{d}{r}\right)$$

where in this case d is the distance to the point at which the velocity of the Rayleigh wave coincides with that of the airblast wave. Then the corresponding time, t_s, is

$$t_s = \frac{d^2}{4a} = \frac{r\alpha}{c}$$

and

$$\tau_s = \alpha$$

A simple analysis of the vertical velocity response of the medium at the surface will reveal readily some interesting relationships without the aid of the electronic computer. Placing $\ell = 0$ in Equation 34, the following expression for the vertical velocity is obtained:

$$\dot{w}\Bigg|_{\ell = 0} = \frac{-c\sqrt{3}\left(\gamma^2 - \frac{1}{3}\right)^{\frac{1}{2}}}{16\pi r^2 \mu} I_m \left\{ -\frac{S_o}{\alpha_{so}}\left[\frac{1}{\sqrt{\tau^2 - \gamma^2}} - \frac{1}{\sqrt{(\tau + \alpha_{so})^2 - \gamma^2}}\right] - S_1 \frac{\tau + \alpha_{s1}}{\left[(\tau + \alpha_{s1})^2 - \gamma^2\right]^{\frac{3}{2}}} \right\} \qquad (13)$$

The above expression shows that at three values of the nondimensional time τ, the velocity $\dot{w}$ at the surface approaches infinity; namely, at $\tau_o = \gamma$; at $\tau_{so} = \gamma - \alpha_{so}$; and at $\tau_{s1} = \gamma - \alpha_{s1}$. The significance of the three values of τ which yield infinite velocities at the surface is easily seen from the time-distance curve of Figure 43(a). Here two curves are used to indicate the travel of the blast wave, one for the ring loading and one for the cylindrical loading. The point on each curve at which the Rayleigh wave velocity is equal to the blast wave velocity was shown previously to be at times $\tau = \alpha_{s1}$ and $\tau = \alpha_{so}$ and at ranges $d/r = 2\alpha_{s1}/\gamma$ and $d/r = \alpha_{so}/\gamma$ respectively.

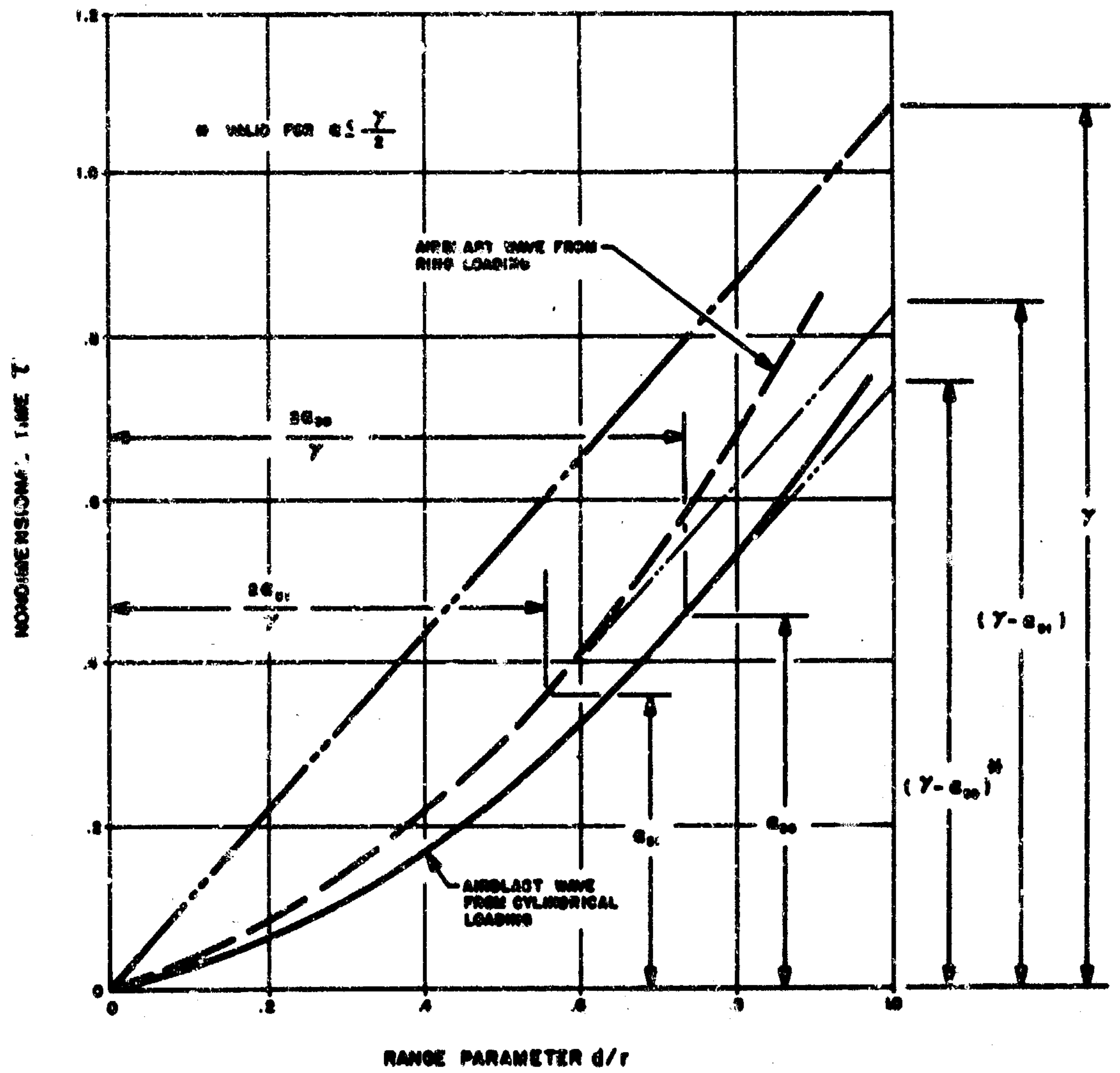

Figure 43(a). Time-Distance Curve for Rayleigh Waves Generated by Cylindrical and Ring Airblast Loadings.

Nondimensional velocity can be related to the dimensional velocity by the expression:

$$\frac{d(d/r)}{d\tau} = \frac{1}{c}\,\frac{d(d)}{dt}$$

Then when

$$\frac{d(d)}{dt} = c, \quad \frac{d(d/r)}{d\tau} = 1.0$$

$$\frac{d(d)}{dt} = c_r, \quad \frac{d(d/r)}{d\tau} = \frac{1}{\gamma}$$

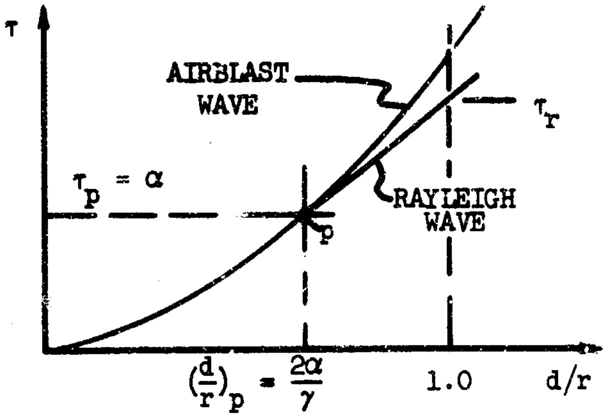

Figure 43(b). Time-Distance Curve.

From the geometry of Figure 43(b), it is seen that

$$\tau_r - \tau_p = \gamma\,[1 - (\frac{d}{r})_p]$$

where the subscript, p, indicates values at the point of tangency, p, and the subscript, r, indicates values at d/r = 1.0. Then

$$\tau_r = \gamma - \alpha$$

Thus the Rayleigh wave generated by the cylindrical loading arrives at d/r = 1.0 when

$$\tau_{so} = \gamma - \alpha_{so}$$

and the Rayleigh wave generated by the ring loading arrives when

$$\tau_{s1} = \gamma - \alpha_{s1}$$

These relationships are valid of course only for $\alpha \leq \gamma/2$. At larger values of α, d/r is greater than 1.0 and the point of tangency, that is the point at which the airblast and Rayleigh wave velocities are equal, occurs at a ground range beyond the point of interest.

It is seen that these are precisely the values of τ at which the velocity $\dot{w}$ becomes infinite. Thus at range $d = r$, the value $\tau = \gamma$ simply marks the arrival of a Rayleigh wave which was generated at the source at $\tau = 0$. The value $\tau = \gamma - \alpha_{s1}$ indicates the arrival at r of a Rayleigh wave either which traveled at the velocity of the ring loading until it became less than the Rayleigh wave velocity or which originated at the point where the two velocities were equal. At greater ranges where $c_r > v$, the Rayleigh wave continued at constant velocity c_r, arriving at range r when $\tau = \gamma - \alpha_{s1}$. Similarly the third infinite value of $\dot{w}$ occured when the Rayleigh wave generated by the cylindrical loading at the point where the two velocities were equal reached range r at $\tau = \gamma - \alpha_{so}$.

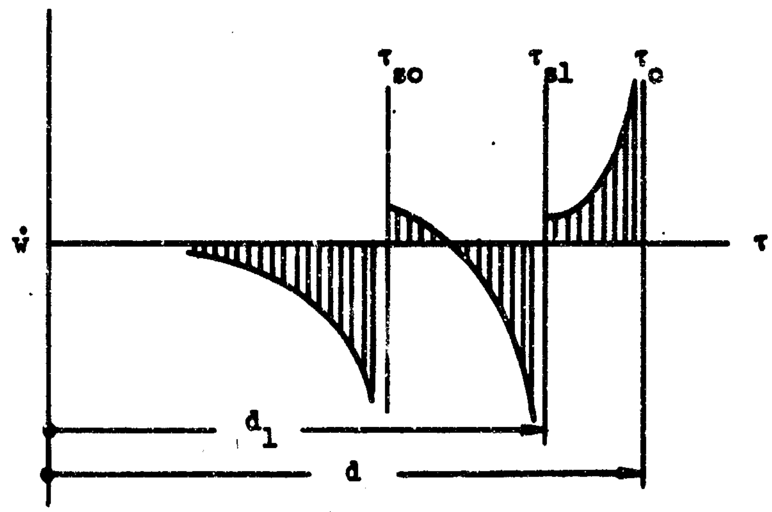

Figure 44. Vertical Velocity at Surface.

Using Equation (13), the response can be approximated as shown in Figure 44. If the two pressure loadings were to move with the same speed, the center of pressure of the line loading would coincide with the wavefront of the area loading and their phases would coincide. It is improbable that an airblast wave having the continuous variation of pressure with time typical of those generated by nuclear bursts would produce the two distinct pulses such as the first two shown in Figure 44 even though the pressure decay rate following the wavefront were very rapid. Thus the two simple peaks at τ_{so} and τ_{s1} would merge into one.

Another characteristic of the response that can be obtained by Equation 13 is the relatively slow rise in the response, $\dot{w}$, followed by a very abrupt decay. This phenomenon exists not only on the surface but also below the surface to considerable depth, even though the response will be finite due to the presence of the term $\ell(\gamma^2 - 1/3)^{1/2}$ in Equation 34. The presence of this spatial decay may be of importance in regard to spalling of rock.

D. Calculated Responses, Region I. **Responses obtained by computer** solutions of Equation 34 are shown in Figures 45 through 52. It may be noted that in all eight cases, the form of the vertical velocities due to Rayleigh waves agrees closely with that predicted in Figure 44 and by a study of the relationship of the parameters. In each case a wave originating at the source at $\tau = 0$ reaches range $d = r$ at $\tau = \gamma = 1.08$ and at $\tau = \gamma - \alpha_{s1}$ a negative spike of lower amplitude occurs. This latter wave originates at the range at which the velocity of the airblast wave from the ring loading equals the Rayleigh wave velocity, i.e., at $d/r = 2\alpha_{s1}/\gamma$.

The first wave to reach the point of interest in all figures except 48 and 52 reached range $d=r$ at $\tau = \gamma - \alpha_{so}$ and originated at range $d/r = 2\alpha_{so}/\gamma$ at $\tau = \alpha_{so}$ when the velocity of the airblast wave from the cylindrical loading was equal to the Rayleigh wave velocity. In Figures 48 and 52, the values of α_{so} and α_{s1} are 1.0 and 0.6 respectively. Thus Rayleigh

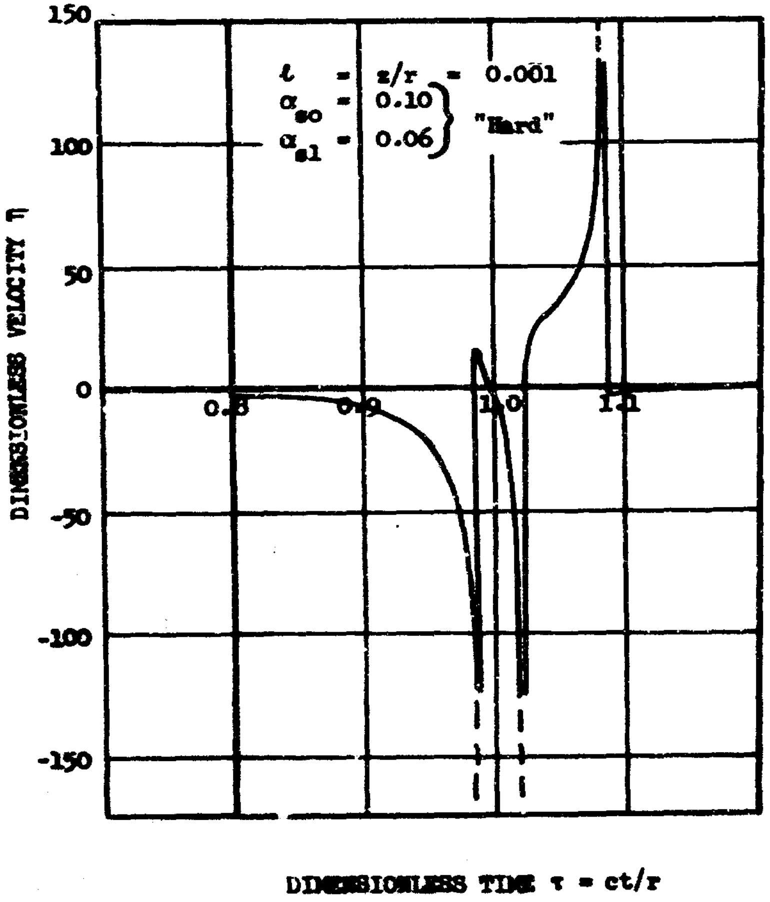

Figure 45. η vs. τ for Rayleigh Waves in Region I; $\ell = 0.001$, $\alpha_{so} = 0.1$, $\alpha_{s1} = 0.06$.

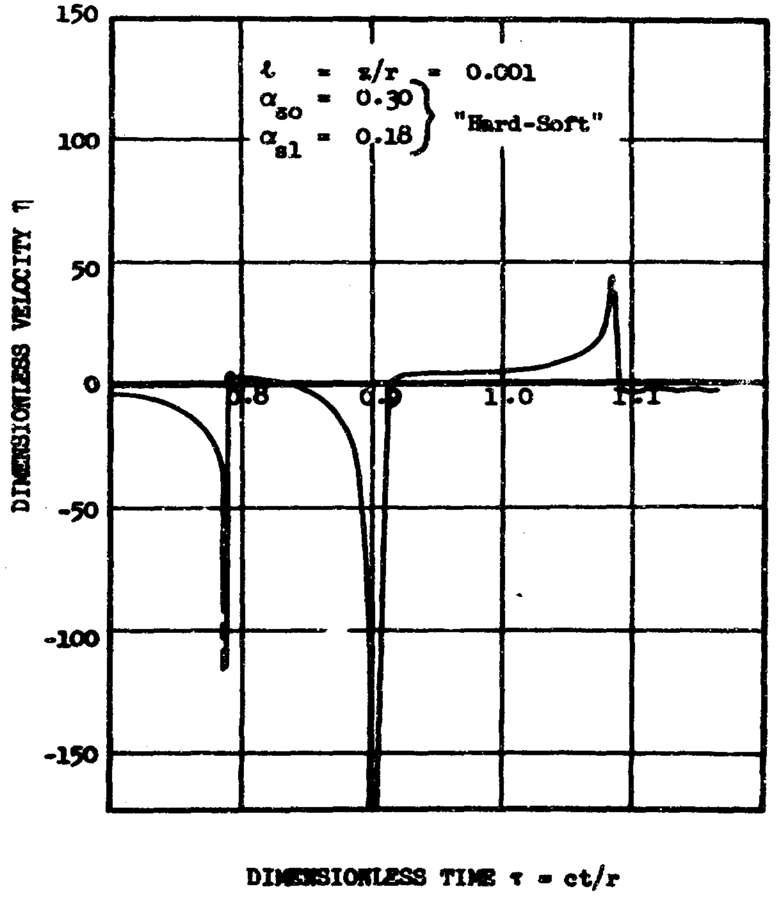

Figure 46. η vs. τ for Rayleigh Waves in Region I; $\ell = 0.001$, $\alpha_{so} = 0.30$, $\alpha_{s1} = 0.18$.

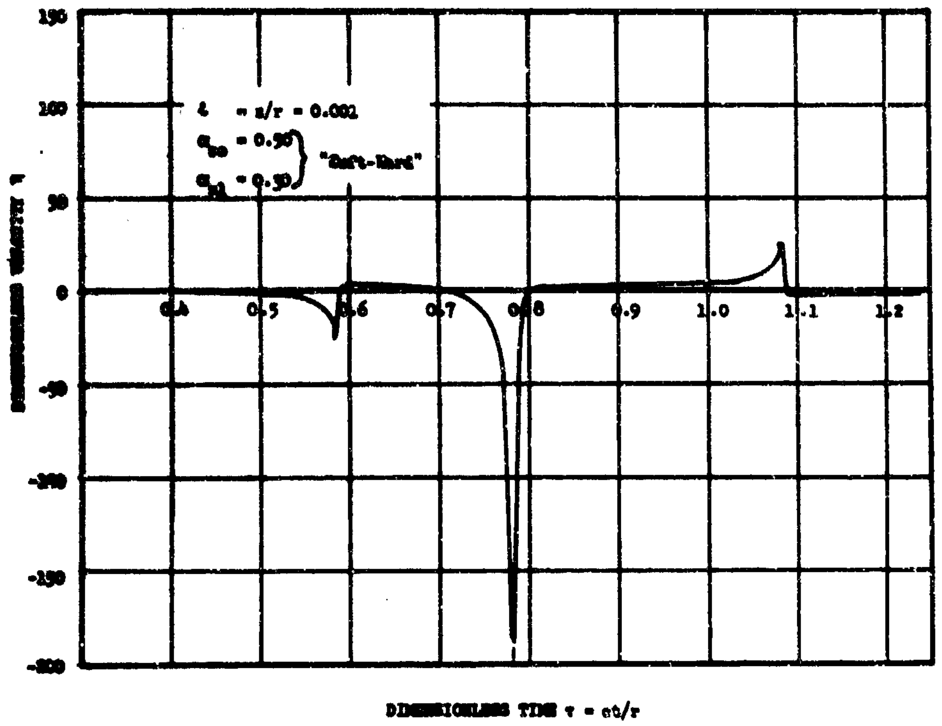

Figure 47. η vs. τ for Rayleigh Waves in Region I; $\ell = 0.001$, $\alpha_{so} = 0.50$, $\alpha_{sl} = 0.30$.

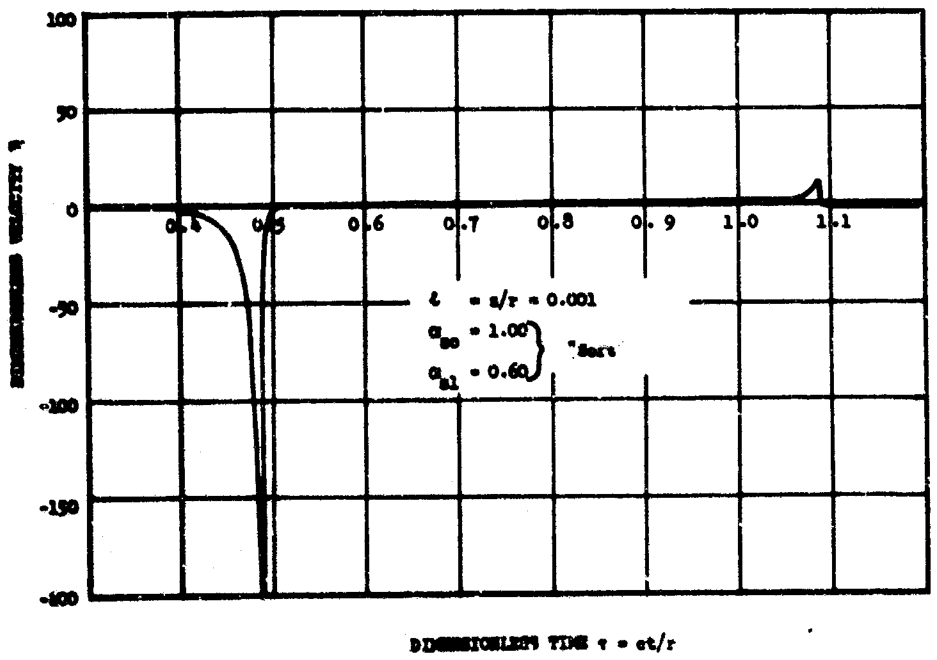

Figure 48. η vs. τ for Rayleigh Waves in Region I; $\ell = 0.001$, $\alpha_{so} = 1.00$, $\alpha_{sl} = 0.60$.

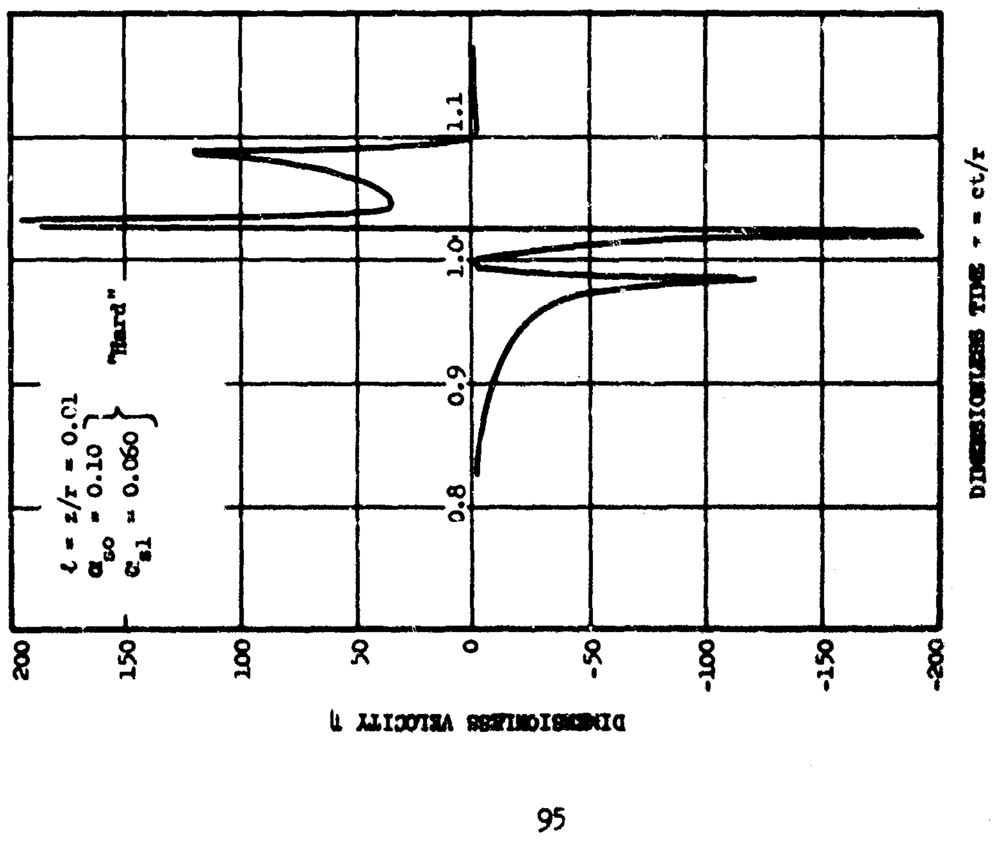

Figure 49. η vs. τ for Rayleigh Waves in Region I; $\ell = 0.01$, $\alpha_{so} = 0.10$, $\alpha_{s1} = 0.060$.

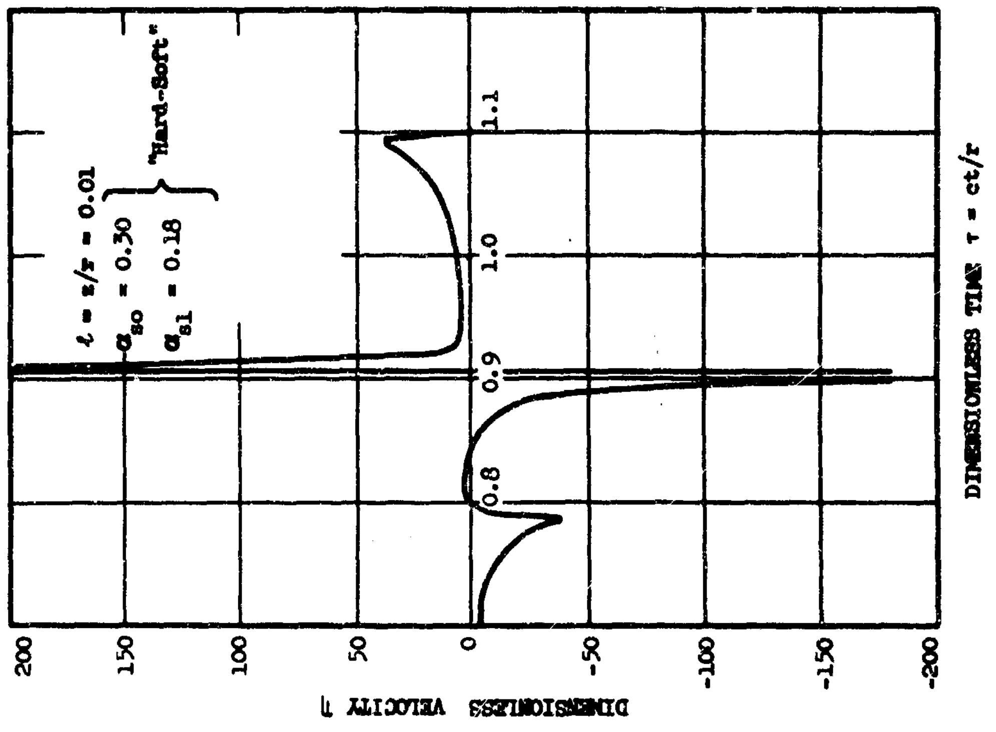

Figure 50. η vs. τ for Rayleigh Waves in Region I; $\ell = 0.01$, $\alpha_{so} = 0.30$, $\alpha_{s1} = 0.18$.

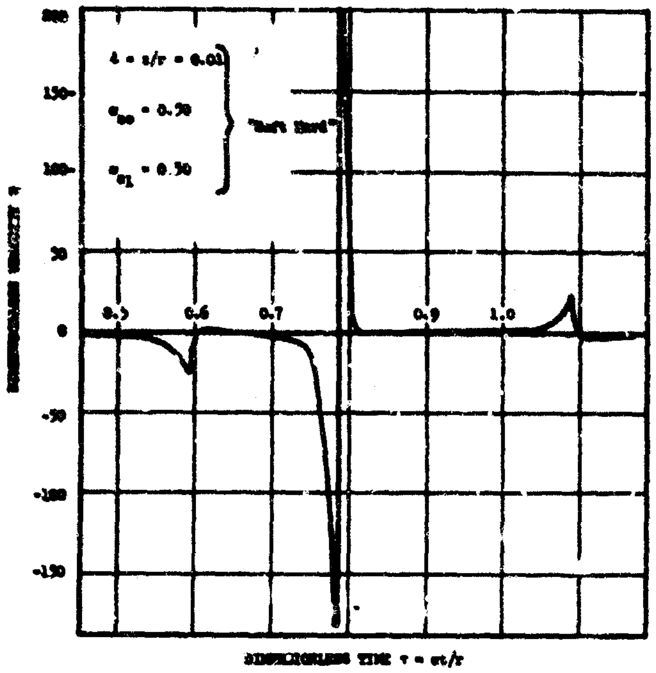

Figure 51. η vs. τ for Rayleigh Waves in Region I;
$\ell = 0.01, \alpha_{so} = 0.50, \alpha_{sl} = 0.30$.

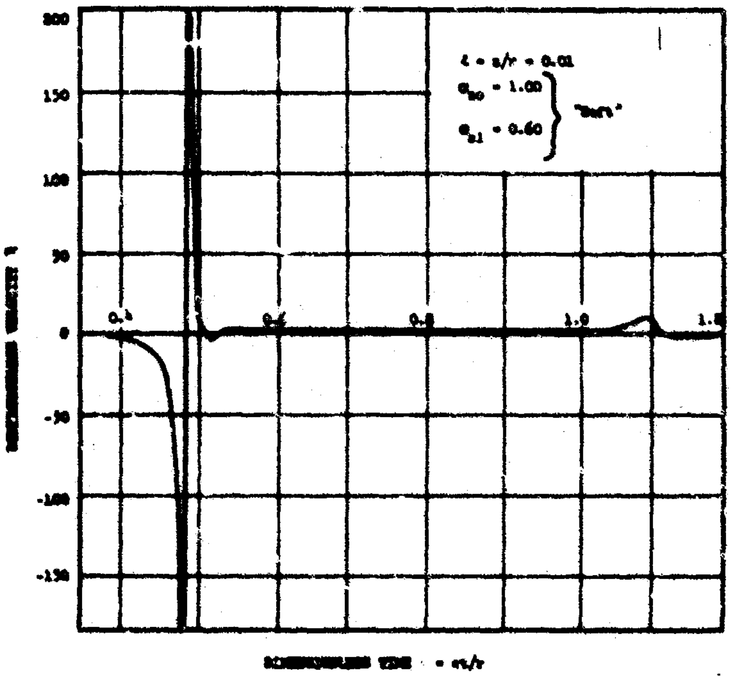

Figure 52. η vs. τ for Rayleigh Waves in Region I;
$\ell = 0.01, \alpha_{so} = 1.00, \alpha_{sl} = 0.60$.

waves arrived at d = r simultaneously with the airblast waves. These times were,

$$\tau_o = \frac{\gamma^2}{4\alpha_{so}} = 0.29$$

for the cylindrical loading and

$$\tau_1 = \frac{\gamma^2}{4\alpha_{s1}} = 0.48$$

for the ring loading.

It may be noted that the Rayleigh waves resulting from the passage of the cylindrical loading across range r are not shown in Figures 48 and 52 as they arrive prior to the minimum value of τ shown.

In all these curves, based on an elastic medium, a fixed spike ratio $S_1/S_o = 0.3$ and a fixed velocity parameter ratio $\alpha_{s1}/\alpha_{so} = 0.6$, there should be no fundamental changes in shape if the ratios are varied only slightly. As shown previously, the phasing between the Rayleigh waves resulting from the cylindrical and from the ring loading is

$$\Delta\tau = \alpha_{s1} - \alpha_{so}$$

while the phasing between the Rayleigh wave due to the ring loading and that generated at the source is

$$\Delta\tau = \alpha_{s1}$$

Both of these differences are valid, of course, only if both α_{so} and α_{s1} are equal to or greater than $\gamma/2$.

Time-distance curves for each of the values of α_{so} are shown in Figures 53 through 56. Also indicated in the figures are the arrivals of the dilatational waves.

In Figures 45 through 52 it may be noted that the values for the dimensionless velocity parameter $\hat{v}$ are sharply peaked and that in many cases their maxima lie outside the range shown. In actual cases of groundshock

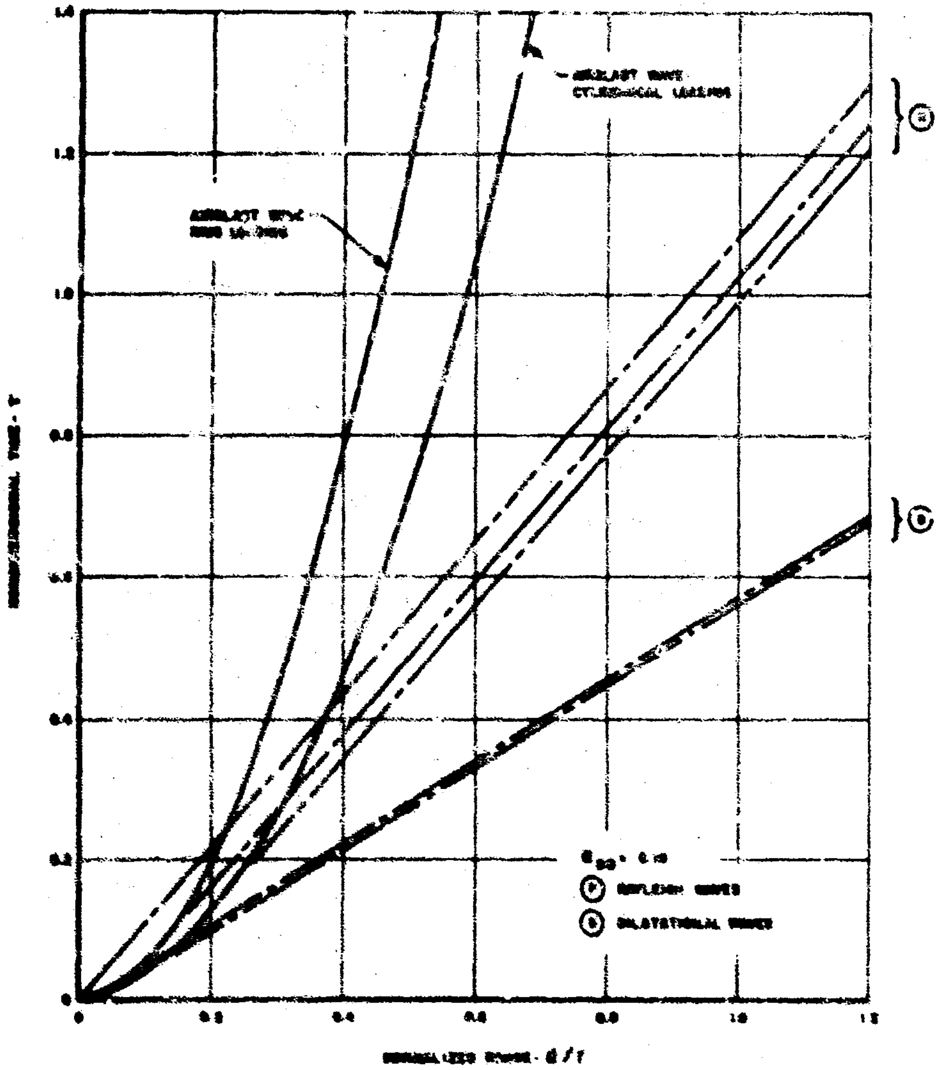

Figure 53. Time-Distance Curve for Rayleigh and Dilatational Waves, α_{so} = 0.10.

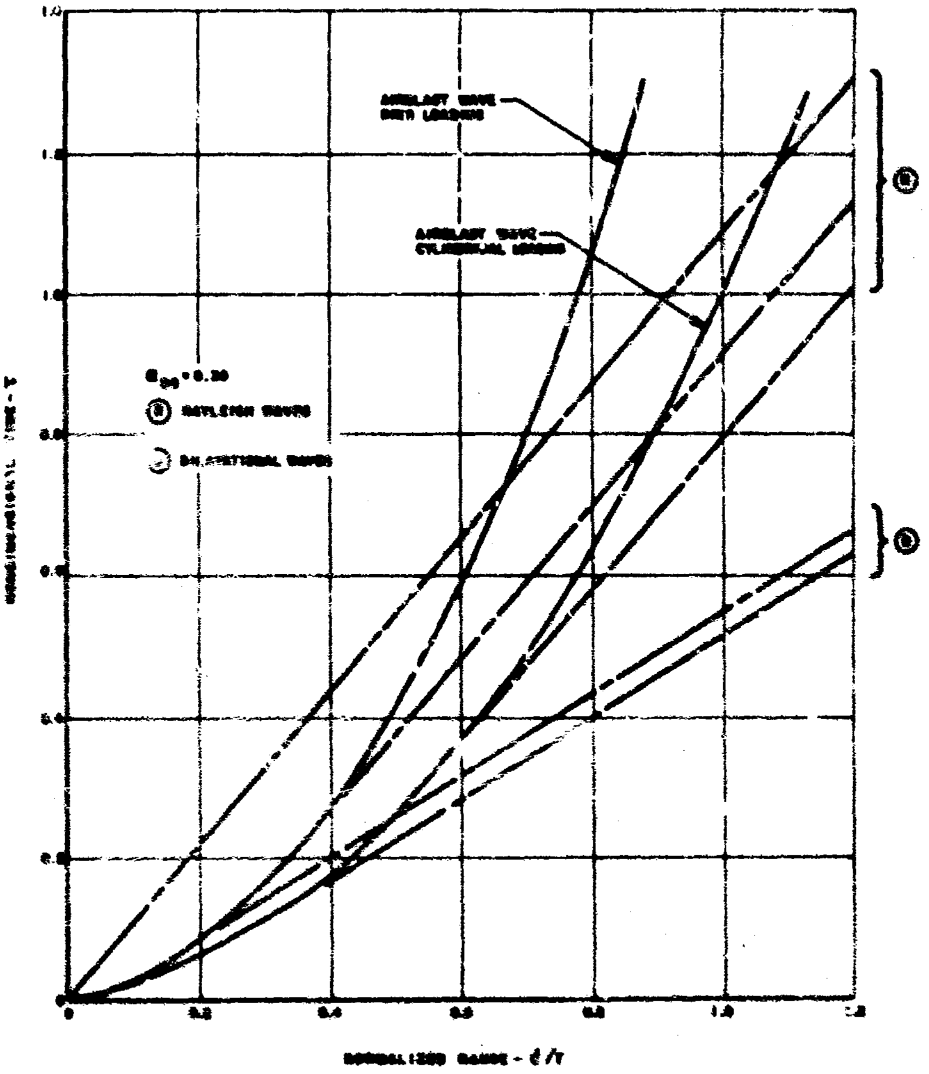

Figure 54. Time-Distance Curve for Rayleigh and Dilatational Waves, α_{so} = 0.30.

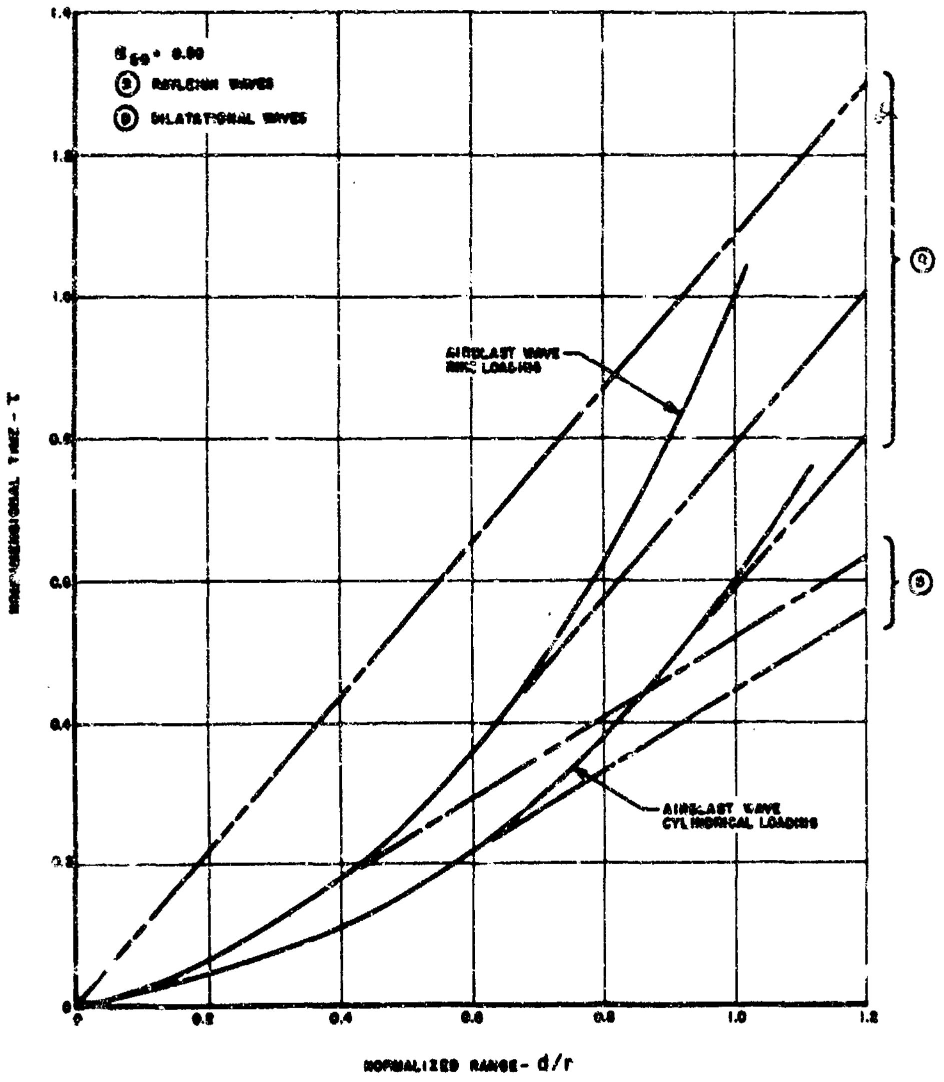

Figure 55. Time-Distance Curve for Rayleigh and Dilatational Waves, α_{so} = 0.50.

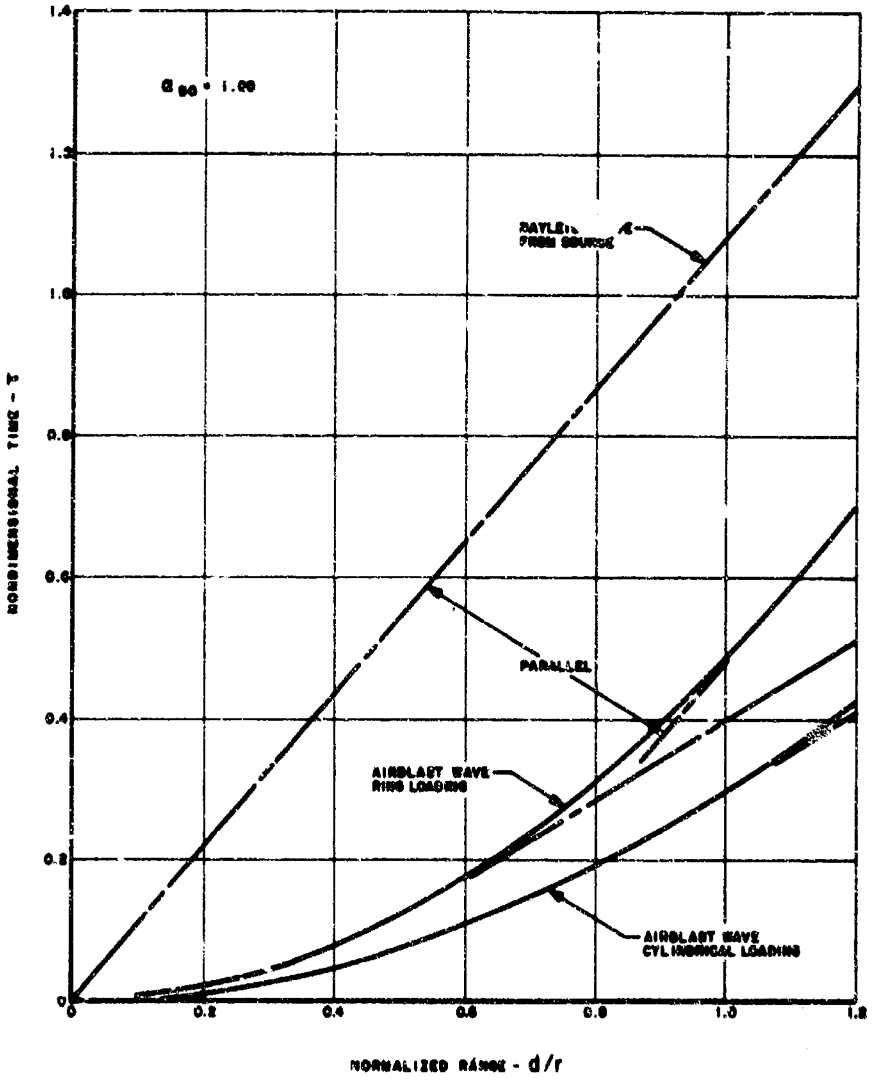

Figure 56. Time-Distance Curve for Rayleigh and Dilatational Waves, α_{sc} = 1.00.

these peaks would be attenuated significantly due to two factors. First, in the region surrounding the point of burst, the elastic theory is invalid since at the extremely high pressures in this region the medium acts essentially like a fluid, in which of course, Rayleigh waves do not occur. Thus waves originating within this region would be expected to be less severe than those predicted by elastic theory.

A second factor tending to reduce the strength of the waves is that even competent rock will not remain elastic at the high stresses accompanying the high velocities. Soils, of course, will produce even greater attenuations particularly if near the surface, since they will yield appreciably in compression and can sustain tensile loads no greater than the in situ compression.

Thus the strengths of the waves shown in the curves represent an upper bound of those that might be expected to occur in a real medium. Further, the wave velocities and shapes would be altered by nonlinearities in the medium, thus changing the arrival times and phasing of the waves from those indicated. This latter effect however would be expected to be relatively small.

Although the strengths of Rayleigh waves in a real medium could be appreciably less than those shown in the curves, it is of interest to compare their strengths with those of dilatational waves generated by the airblast loading at the same sites. Of the four cases for which numerical values were obtained, one ($\alpha_{so} = 1.00$) was at the transeismic point while the remaining three were in the subseismic or outrunning region. In the transeismic and subseismic regions, the vertical velocity at the surface due to an airblast pressure p is not equal to p/ρc but is increased by the contribution of the ground-transmitted shock from the airblast wave when it was at a lesser range. Reference 26 recommends the use of a factor of 1.4 to account for this effect. Thus

$$\dot{u} = \frac{1.4p}{\rho c_p}$$

where $\dot{u}$ is the vertical velocity due to the airblast pressure

In calculating the strengths of the Rayleigh waves, it was assumed

$$S_o = p_o \pi d^2$$

where S_o was the total force exerted on the surface of the ground by the cylindrical loading and p_o was the overpressure due to the cylindrical loading. Referring to Table 13, it is seen that the pressure p_1 due to the ring loading is about three times p_o. Then

$$S_o = \frac{\pi p_1 d^2}{3}$$

Letting $p = p_1$ and $d = r$, $c = 0.577\ c_p$

$$\dot{u} = \frac{4.2\ S_o}{\pi r^2 \rho c_p} = \frac{2.4\ S_o}{\pi r^2 \rho c}$$

The ground velocity parameter η due to the Rayleigh wave was given as

$$\eta = \frac{62.8 r^2 \mu \dot{w}}{c S_o}$$

Substituting $c\rho = \mu/c$

$$\eta = \frac{62.8 \rho c r^2 \dot{w}}{S_o}$$

Then

$$\frac{\dot{w}}{\dot{u}} = \frac{\eta}{48}$$

Now in Figures 45 through 52 it is seen that the peak strengths of the Rayleigh waves generated by the ring loading are very high, exceeding 200 units. Thus for the case of an elastic medium, and recognizing the approximate nature of the comparison, it is seen that the strength of the Rayleigh wave due to the ring loading can be larger than that due to the dilatational wave generated by the ring loading.

E. Rayleigh Waves in Real Media. A direct quantitative comparison of the Rayleigh wave pattern resulting from a disturbance in an elastic, homogeneous medium with the oscillatory motions observed at highly stratified real sites, of course, is not possible. This work however was directed primarily toward the identification of phenomena which might contribute significantly to the Type II oscillation rather than toward direct correlations. In this respect it appears that the investigation was successful and that several points of importance can be established.

The Rayleigh wave generated by a step loading consists of a single pulse-like motion in the vertical direction with negligible oscillation. The wave motion resulting from an impulse loading appears to consist of a single-cycle oscillation. In neither case is a train of waves generated. It is doubtful if the wave transmitted directly from the initial disturbance would be of significance in a real medium. As it must follow the direct-induced compressional wave and the air-induced wave, it must pass through the ruptured zone surrounding the crater. In this region it is likely that the highly inelastic behavior of the medium would damp the wave to a negligible strength.

Even for the elastic case it may be noted that the wave generated by the steep-fronted airblast wave as it recedes from ground zero at a velocity equal to that of the Rayleigh wave is by far the most severe. As the velocities of the airblast wave and the Rayleigh wave are matched outside of the rupture zone, and as this Rayleigh wave is generated in a medium which has been preconsolidated by the passage of the dilatational wave, it is possible that the strength of this wave as predicted by elastic theory may not be too far in error.

The form of an actual airblast wave consists of a single exponentially decaying pulse rather than the two distinct blast loadings assumed in the analysis. Thus the two Rayleigh waves generated by the blast loadings would, in fact, be superimposed. In addition, the strength of the combined wave would be less than that shown due to dissipation, the oscillation would be broadened due to the nonlinearity of the medium and the symmetry of the oscillation would be distorted by the inability of the medium to sustain large tensile stresses.

In this analysis, it was assumed that the medium was homogeneous. At layered sites, however, and for certain ratios of density and Lame's constants of the two media, a modified form of the Rayleigh wave can exist at the interface. As it travels at a velocity slightly different from that of the surface Rayleigh wave, it would be expected that the motion at shallow depths would be the superposition of the motions due to the two sets of Rayleigh waves but at some difference in phase. Layering would also be expected to result in other phenomena, such as refractions and reflections at the interface, which were not considered here.

Quantitatively, then, a rough picture of the Rayleigh waves at a real site can be constructed. In the outrunning or subseismic region where the Type II oscillations were observed, the Rayleigh wave can never arrive first, although near the transeismic point in a homogeneous medium it may arrive simultaneously with the airblast-induced motion. The initial direction of the vertical component will be upward similar to the initial upward motion of the Type II wave. The principal part of the ground velocity due to the Rayleigh wave will consist of one full cycle oscillation.

The lack of an indication of the intensity of the Rayleigh wave in real, layered media precludes the positive identification of any contribution they may have made to the observed Type II waveforms. Since they arrived at the point of measurement after the arrival of the refracted wave, they could not have been responsible for the initial upward motion. It is possible that some of the later oscillations however are due at least in part to Rayleigh waves.

This page intentionally left blank.

REFERENCES

1. The Ralph M. Parsons Company: *A Guide for the Design of Shock Isolation Systems for Underground Protective Structures*, Air Force Special Weapons Center, AFSWC-TDR-62-64, December 1962.
2. Thornburgh, H. R.: "Wave-Front Diagrams in Seismic Interpretation," The American Association of Petroleum Geologists, Vol. XIV, Part 2, February 1930.
3. Wilson, S. D., and M. J. Hammer: *Subsurface Investigations and Ground Motion Studies at Nevada Test Site*, Shannon and Wilson, Contract AF 04(647)-650, January 1961 (S); Addendum 1, April 1961 (S).
4. Knott, C. G.: "Reflection and Refraction of Elastic Waves with Seismological Applications," Phil. Mag., Vol. 48, 1899.
5. Jakosky, J. J.: *Exploration Geophysics*, Trija Publishing Company, California, 1950.
6. Muskat, M., and M. W. Meres: "Reflection and Transmission Coefficients for Plane Waves in Elastic Media," Geophysics, Vol. V, No. 2, April 1940.
7. Ewing, W. M., W. S. Jardetsky, and F. Press: *Elastic Waves in Layered Media*, McGraw-Hill Book Company, Inc., New York, 1957.
8. Howell, B. F., Jr.: *Introduction to Geophysics*, McGraw-Hill Book Company, Inc., New York, 1959.
9. Muskat, M. and M. W. Meres: "The Seismic Wave Energy Reflected from Various Types of Stratified Horizons," Geophysics, Vol. V, No. 2, April 1940.
10. Wolf, A.: "The Amplitude and Character of Refraction Waves," Geophysics, Vol. I, No. 3, October 1936.
11. Gutenberg, B.: "The Amplitudes of Waves to be Expected in Seismic Prospecting," Geophysics, Vol. I, No. 2, June 1936.
12. Salmon, V. and S. R. Hornig: *Earth Accelerations vs. Time and Distance - Operation Tumbler, Project 1.7, WT-517*, Stanford Research Institute, February 1953 (U).
13. Perret, W. R.: *Ground Motion Studies at High Incident Overpressures, Operation Plumbbob, WT-1405, Project 1.5*, Sandia Corporation, 1960.

14. Swift, L. M. and D. C. Sacks: Ground Motion Produced by Nuclear Detonations, Operation Hardtack, Project 1.8 Stanford Research Institute I R-1613, August 1958 (S).

15. Whitman, R. V. and G. B. Clark: Nuclear Geoplosics, Part Two - Mechanical Properties of Earth Materials, DASA-1285 (II)(Compiled by Stanford Research Institute), May 1964.

16. Sauer, F. M.: Ground Motions Produced by Aboveground Nuclear Explosions, Air Force Special Weapons Center SWC-TN-59-71, April 1959 (S).

17. Richer, N.: "The Form and Nature of Seismic Waves and the Structure of Seismograms," Geophysics, Vol. V, No. 4, October 1940.

18. Baron, M. L. and C. Lecht: "Elastic Rayleigh Wave Effects Due to Nuclear Blasts," Journal of Engineering, Mechanics Division, Proceedings of ASCE, Vol. 87, No. EM5, Part 1, October 1961.

19. Pekeris, C. L. and H. Lifson: "Motion of the Surface of a Uniformly Elastic Half-Space Produced by a Buried Pulse," Journal of the Acoustical Society of America, Vol. 29, No. 11, November 1957.

20. Chao, C. C., H. H. Bleich and J. L. Sackman: Surface Waves in an Elastic Half-Space, Rand Corporation Report P-2066, August 1960.

21. Rand Corporation: Space Plots of Pressure, Density and Particle Velocity for the Blast Wave from a Point Source in Air, RM-1913-AEC, June 1957.

22. Taylor, G. I.: "Proceedings of the Royal Society," Series A-201, 1950.

23. Lamb, H.: "Transactions of the Royal Society," Series A-203, 1904.

24. Tables of Integral Transforms, Bateman Manuscript Project, McGraw-Hill Book Company, 1957.

25. Sauer, F. M., Clark, G. B. and Anderson, D. C.: Nuclear Geoplosics, Part Four - Empirical Analysis of Ground Motion and Cratering, DASA-1285 (IV)(Compiled by Stanford Research Institute), May 1964.

26. Nathan N. Newmark Consulting Engineering Services: (U) Computations of Free-Field Motion and Shock Spectra for Linear and Nonlinear Systems, Prepared for The Ralph M. Parsons Company, 15 July 1964 (S).

27. Brode, H.L.: A Review of Nuclear Explosion Phenomena Pertinent to Protective Construction, R-425-PR, The Rand Corporation, May 1964 (U).

APPENDIX A

CONSTRUCTION OF A REFRACTION WAVEFRONT DIAGRAM

The refraction wavefront diagram is a graphical representation in a vertical plane passing through the source and the station of interest of the positions at discrete time intervals of the direct-induced and refracted waves emanating from the source. Since these waves will always precede reflected or shear waves, the refraction wavefront diagram indicates directly the earliest motion at any point. With the assumption of linearity of the medium, later arrivals can be depicted in a similar manner as can the propagation of reflected waves.

A great degree of detail can be included in the wavefront diagram if it is desired to do so. Nonhomogeneity can be represented by many homogeneous layers of very small thickness, the layers may be oriented in any manner desired, and inclusions of any shape or size may be considered. For the refraction diagram, the assumption of linearity of the medium is not necessary as the first waves to arrive at a point will always travel at the seismic velocity of the medium. For calculating later arrivals through nonlinear media, certain rules of thumb have been employed, although it is in this respect that the most severe limitation of the wavefront diagram is evident; the strength of the wave cannot be determined.

The practical limit to the detail that should be included in the wavefront diagram is dependent, of course, on the accuracies with which the site profile, the soil properties, the weapon size and coupling efficiency and the burst location are known. Since in most cases these parameters are known only within broad ranges, many refinements are not warranted.

In the example discussed here, a three-layered system is considered (Figure 58). The upper or surface layer, with seismic velocity $V_1 = 5000$

feet per second, extends to a depth of 2500 feet; the second layer, with $V_2 = 7500$ feet per second is 4000 feet in thickness; and the third or bottom layer has a seismic velocity $V_3 = 10{,}000$ feet per second. Both of the two interfaces are assumed to lie parallel to the surface although, as noted above, this assumption is not necessary and any orientation of the layers could be considered.

STEP 1: The scale is first selected and the soil profile drawn in. To facilitate construction, the horizontal scale (range) should be equal to the vertical scale (depth). Yet at most sites, the range of interest may extend to several thousands of feet while detail may be desired in a relatively thin layer. Moreover, the diagram construction begins at the source and procedes outward thus accumulating errors. A fairly large scale then is essential if any accuracy is to be achieved.

Beyond the range at which a refraction from the deepest layer returns to the surface the shape of the wavefront and its velocity remain constant. Thus the wavefront diagram need be extended only to this range which may be computed by Equation 8 or derived from the relationships given in Section 2. That is

$$x_c = 2h\sqrt{\frac{V_2 + V_1}{V_2 - V_1}} \qquad \text{for a two-layered system}$$

and

$$x_c = \frac{2}{(V_3 - V_2)}\left[\frac{h_1}{V_1}\left(V_2\sqrt{V_3^2 - V_1^2} - V_3\sqrt{V_2^2 - V_1^2}\right) + h_2\sqrt{V_3^2 - V_2^2}\right] \qquad \text{for a three-layered system}$$

The relationship for the two-layered system is shown in Figure 57.

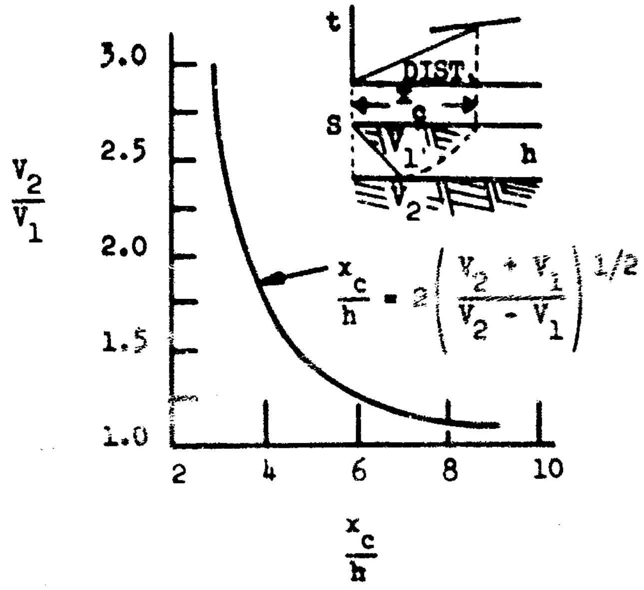

Figure 57. Range - Thickness Ratio at which a Refracted Wave First Reaches the Surface in a Two-Layer System.

STEP 2: Rays at the critical angle beyond which all waves are reflected at the interfaces are then drawn. In Figure 58 the ray $\overline{OA}$ represents the limiting path in the Layer 1 - Layer 2 system. The critical angles are determined according to Snell's Law as described in Section 2.

STEP 3: Select a time interval and from the source "O", draw in Layer 1 circular arcs representing the position of the direct-induced wave at these times. The arcs should be extended lightly into Layer 2 as shown by the dashed lines in Figure 58.

STEP 4: The wavefronts in Layers 2 and 3 will not be circular arcs. Directly below the source the wave will propagate vertically at the seismic velocity of the layer. Along the interface with a shallower, softer layer and at angles from the source less than the critical angle, the horizontal component of the wave velocity in the lower layer will be less than the horizontal component of the velocity in the upper layer. At Points A and B, the horizontal velocity components in the two adjacent layers will be

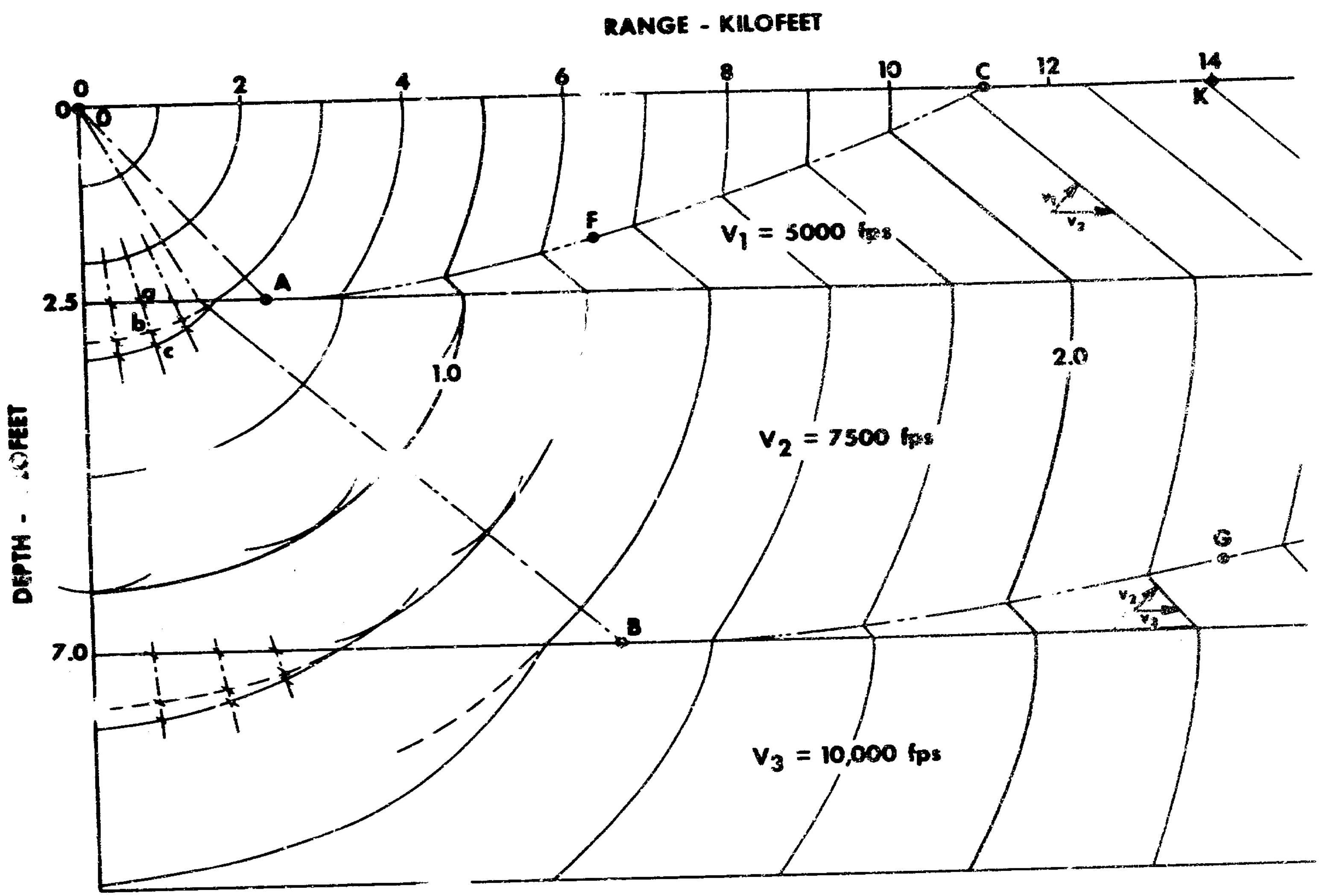

Figure 58. Construction of Refraction Wavefront Diagram.

exactly equal and at greater ranges, the velocity in the lower layer along the interface will exceed that in the upper layer. Thus along an interface, between Layers 1 and 2 for example, and at ranges greater than Point A, the initial motion is generated by the first disturbance reaching Point A. However, at all points within Layer 2 below the interface with Layer 1, except for those regions where waves are refracted into Layer 2 from lower layers, the initial motion is generated by disturbances arriving at the interface from ranges less than Point A. As noted earlier, then, the wave profiles in Layer 2 are not circular arcs.

At ranges shorter than those indicated by the critical ray, intermediate points on the wavefront lying between the interface and the depth scale can be determined graphically by constructing radii from the source through the region of interest, such as line $\overline{abc}$. As the dashed line is simply an extension of the circular arcs in Layer 1, $\overline{ab}$ is the distance the wave would travel in Layer 2 if V_2 were equal to V_1. Then the actual distance $\overline{abc}$ must be $\overline{ab} \times V_2/V_1$. Three or four such radii are sufficient for the accuracy needed in most practical applications.

At ranges greater than Point A for Layer 2 and Point B for Layer 3, the wavefronts will be equidistant from the wavefronts passing through Points A and B respectively.

<u>STEP 5</u>: The fronts in Layer 1 along the interface between Layers 1 and 2 beyond Point A are first reached and set in motion by the disturbance traveling in and along the top of Layer 2. This "underlayer wave" has a straight wavefront in Layer 1 with a slcpe of V_1/V_2 as shown in Figure 58.

The intersection of the underlayer wave and the direct wave having the corresponding time is a point on the coincident-time curve $\overline{AC}$ in Layer 1. The coincident-time curve originates at Point A in Layer 1, and at Point B in Layer 2. In Layer 2, the coincident-time curve represents the intersection between the refracted wavefront of Layer 2 and the underlayer wave originating from Layer 3.

The points where the coincident-time curve intersects the ground surface is represented on the time-distance curve by an abrupt change in the slope of the line, as shown by Points C and D in Figure 8.

The wavefront diagram started in Figure 58 is shown in its completed form in Figure 5.

APPENDIX B

THEORETICAL ANALYSIS OF GROUNDSHOCK WAVEFORMS

Blast Wave of a Nuclear Detonation and its Idealized Approximation

The characteristics of the blast wave due to a nuclear detonation can be shown roughly as in Figure 37 (21). The maximum pressure occurs at the cylindrical wavefront from which it decays rapidly and levels off toward the epicenter. If S denotes the total load on the ground surface exerted by the blast wave, d, the distance of the wavefront from the epicenter, r, the radial distance of the site from the epicenter and if the peak pressure spike at the wavefront is approximated by a δ-function, then the normal pressure σ exerted on the ground by the blast wave may be written approximately as:

$$\sigma = -S_o \frac{H(d-r)}{\pi d^2} - S_1 \frac{\delta(d-r)}{2\pi d} \qquad (14a)$$

where H(x), δ(x) represent the Heaviside step function and the δ function respectively,

$$S_o + S_1 = S \qquad (14b)$$

and

$$S_o = \frac{P_o}{d}$$

The velocity, v, of the wavefront decays with time and eventually approaches zero as limit. Because of the numerical values given in Figure 37, it is assumed to be inversely proportional to the square root of time counted from the instant of detonation. Namely,

$$v = \sqrt{a/t} \tag{15}$$

where a is a proportional constant. Accordingly, the location of the wavefront at time t can be easily computed as:

$$d = \int_0^t v\,dt = 2\sqrt{at} \tag{16}$$

It may be noted that this result, $d \sim t^{0.5}$, is very close to G. I. Taylor's intense blast wave theory (22) which shows $d \sim t^{0.4}$. A comparison between Equation 16 and the observed values from Figure 37 are plotted in Figure 40. It may be seen that the agreement is quite good if "a" is taken to be 25 $(\text{kilofeet})^2$/second.

Substitution of Equation 16 into Equation 14 gives the loading function due to a nuclear blast wave as:

$$\sigma = -S_0 \frac{H(2\sqrt{at} - r)}{4\pi at} - S_1 \frac{\delta(2\sqrt{at} - r)}{4\pi\sqrt{at}} \tag{17}$$

Mathematical Analysis

Assume that the ground is a homogeneous, elastic half-space of density ρ, shear modulus μ, and Poisson's ratio $\nu = 0.25$. Using cylindrical coordinates as shown in Figure 59, letting q and w denote the radial and the vertical displacements respectively and following Lamb (23), these displacements may be derived from a dilatational potential ϕ and from a shear potential ψ according to

$$q = \frac{\partial \phi}{\partial r} - \frac{\partial^2 \psi}{\partial r \partial z} \tag{18a}$$

$$w = \frac{\partial \phi}{\partial z} - \frac{\partial^2 \psi}{\partial r^2} - \frac{1}{r}\frac{\partial \psi}{\partial r} \qquad (18b)$$

The governing differential equations of the medium may be written in terms of ϕ and ψ as:

$$c_p^{\,2} \nabla^2 \phi = \frac{\partial^2 \phi}{\partial t^2} \qquad (19a)$$

$$c^2 \nabla^2 \psi = \frac{\partial^2 \psi}{\partial t^2} \qquad (19b)$$

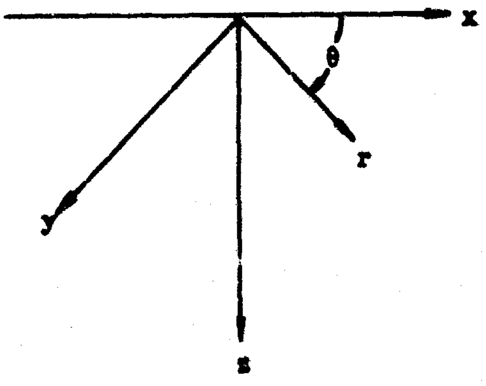

Figure 59. Cylindrical Coordinates.

where

$$c = (\mu/\rho)^{1/2} \text{ and } c_p = 3(\mu/\rho)^{1/2} = \sqrt{3c} \qquad (20)$$

denote the shear and dilatational wave speeds of the medium respectively.

The solutions to Equations 19a and 19b are subjected to the boundary conditions

$$\sigma_{zz} = \mu \left(\nabla^2 \phi + 2 \frac{\partial \psi}{\partial z} \right) = \sigma \qquad t > 0, \ z = 0 \tag{21a}$$

$$\sigma_{zr} = \frac{\partial \phi}{\partial z} + \frac{\partial \psi}{\partial r} = 0 \qquad t > 0, \ z = 0 \tag{21b}$$

where σ is defined in Equation 17 and σ_{zz}, σ_{zr} are stress components of the medium. The displacement and therefore the potentials also must vanish at infinity. The initial conditions are such that all quantities must be zero for $t = 0$.

Let $\bar{q}, \bar{w}, \bar{\phi}, \bar{\psi}, \bar{\sigma}$ and Q, W, Φ, Ψ, Σ denote Laplace and Laplace-Hankel transforms of q, w, ϕ, ψ, σ respectively according to

$$(\bar{q}, \bar{w}, \bar{\phi}, \bar{\psi}, \bar{\sigma}) = \int_0^\infty (q, w, \phi, \psi, \sigma)^{-pt} \, dt \tag{22a}$$

$$(q, w, \phi, \psi, \sigma) = \frac{1}{2\pi i} \int_{B_r} (\bar{q}, \bar{w}, \bar{\phi}, \bar{\psi}, \bar{\sigma}) e^{pt} \, dp \tag{22b}$$

$$\begin{bmatrix} W, \Phi, {}_{Q}\Psi, \Sigma \end{bmatrix} = \int_0^\infty \begin{bmatrix} \bar{w}, \bar{\phi}, {}_{\bar{q}}\bar{\psi}, \bar{\sigma} \end{bmatrix} \begin{bmatrix} J_0(\xi r) \\ J_1(\xi r) \end{bmatrix} r \, dr \tag{23a}$$

$$\begin{bmatrix} \bar{w}, \bar{\phi}, {}_{\bar{q}}\bar{\psi}, \bar{\sigma} \end{bmatrix} = \int_0^\infty \begin{bmatrix} W, \Phi, {}_{Q}\Psi, \Sigma \end{bmatrix} \begin{bmatrix} J_0(\xi r) \\ J_1(\xi r) \end{bmatrix} \xi \, d\xi \tag{23b}$$

where p and ξ are Laplace and Hankel transform parameters and B_r indicates the path of integration for inverse Laplace transform such that $\bar{q}, \bar{w}, \ldots$ are analytical functions of p to the right of B_r.

The transformed equations corresponding to Equations 19a, 19b, 21a, and 21b are:

$$\frac{d^2\phi}{dz^2} - \left(\xi^2 + h^2\right)\phi = 0 \qquad (24a)$$

$$\frac{d^2\psi}{dz^2} - \left(\xi^2 + k^2\right)\psi = 0 \qquad (24b)$$

$$\left(2\xi^2 + k^2\right)\phi + 2\xi^2\frac{d\psi}{dz} = \Sigma/\mu,\ z = 0 \qquad (25a)$$

$$2\frac{d\phi}{dz} + \left(2\xi^2 + k^2\right)\psi = 0,\ z = 0 \qquad (25b)$$

where

$$h = p/c_p = \frac{p}{\sqrt{3}c}\ ;\ k = p/c \qquad (26)$$

and Σ is the Laplace-Hankel transform of the loading function σ which takes the form (24) of:

$$\Sigma\left(\xi, p\right) = \frac{-S_o}{2\pi\xi^2}\left(1 - e^{-a\xi^2/p}\right) - \frac{S_1}{\pi ap}\,e^{-a\xi^2/p} \qquad (27)$$

With the aid of the vanishing boundary conditions at infinity, ϕ and ψ can be obtained explicitly. Substituting into the transformed version of Equations 18a and 18b, the transformed vertical and radial displacements of the medium are given by:

$$W\left(\xi,p,z\right) = \frac{\Sigma\left(\xi,p\right)}{\mu M\left(\xi,p\right)}\left(\xi^2 + h^2\right)^{1/2}\left\{\left(2\xi^2 + k^2\right)\right.$$

$$\left.\cdot\ \exp\left[-z\left(\xi^2 + h^2\right)^{1/2}\right] - 2\xi^2\exp\left[-z\left(\xi^2 + k^2\right)^{1/2}\right]\right\} \qquad (28)$$

$$Q(\xi,p,z) = \frac{\xi\Sigma(\xi,p)}{\mu M(\xi,p)}\left\{\left(2\xi^2 + k^2\right)\exp\left[-z\left(\xi^2 + h^2\right)^{1/2}\right]\right.$$

$$\left. - 2\left(\xi^2 + h^2\right)^{1/2}\left(\xi^2 + k^2\right)^{1/2}\exp\left[-z\left(\xi^2 + k^2\right)^{1/2}\right]\right\} \qquad (29)$$

Where

$$M(\xi,p) = \left(2\xi^2 + k^2\right)^2 - 4\xi^2\left(\xi^2 + h^2\right)^{1/2}\left(\xi^2 + k^2\right)^{1/2} \qquad (30)$$

and the branch of square root is chosen to yield a positive real part in order to insure the vanishing displacement conditions at infinity.

From Equations 28 and 29, similar transformed expressions for radial and vertical velocities, stress and strain components can be easily derived. In particular, the most important quantity needed for detection of the Type II waveform is the vertical component $\dot{w}$ of the particle velocity of the medium, whose Laplace-Hankel transform can be written down readily as $p\,W(\xi,p,z)$.

Formal inversion is accomplished by the aid of Equations 22b and 23b. The vertical particle velocity of the medium then is given by:

$$\frac{\partial w}{\partial t}(r,t,z) = \frac{1}{2\pi i}\int_0^\infty\int_{B_r} \xi p\, W(\xi,p,z)\, e^{pt}\, J_0(\xi r)\, dp\, d\xi \qquad (31)$$

Complete solutions of this integral valid for all stations in the medium require extremely lengthy numerical computations. The present investigation therefore is confined to two regions of practical interest for which the ratio z/r is either very small or very large. Because of the extremal values taken for this ratio, approximations based on physical argument or mathematical simplifications are employed to obtain solutions which can be computed numerically.

Solution for Shallow Depth of Station - Region I. $z/r \ll 1$

For stations far from the loading zone and near the surface, see Figure 41, the major response of the medium is due to Rayleigh waves. This has been discovered by Rayleigh and is well confirmed by seismological experience. It has also been found (19) that if the transform approach were used (as the present analysis did), the Rayleigh wave effect can be obtained from the transformed solution by utilizing only the residues of the inversion integrals at certain poles (Rayleigh poles), ignoring branch integrals which would occur in a complete solution.

The Rayleigh poles of the transformed vertical velocity, Equations 28 and 31, are the zeros of Equation 30, $M(\xi,p) = 0$, which may be easily recognized as Rayleigh's frequency equation of an elastic half-space. The location of the poles are

$$p = ic\xi/\gamma \tag{32a}$$

where

$$\gamma = \frac{1}{2}\left(3 + \sqrt{5}\right)^{1/2} \tag{32b}$$

The contributions from these two poles can be computed with the aid of simple residue theory as

$$\frac{\partial w}{\partial t}(r,t,z) = \frac{c^2\left(\gamma^2 - \frac{1}{3}\right)^{1/2}}{\mu\gamma^2 F(\gamma)}$$

$$\mathrm{Re}\left\{\int_0^\infty \xi^2 J_0(\xi r)\left(2\gamma^2 - 1\right)\exp\left[-\left(1 - \frac{1}{3\gamma^2}\right)^{1/2}\xi z\right]\right.$$

$$\left. - 2\gamma^2\left[\exp -\left(1 - \frac{1}{\gamma^2}\right)^{1/2}\xi z\right]\right\}\exp\left(\frac{ic\xi t}{\gamma}\right)\Sigma\left(\xi, \frac{ic\xi}{\gamma}\right)d\xi \tag{33}$$

where

$$F(\gamma) = -\frac{8\gamma}{\sqrt{3}}$$

and Re indicates the real part of the quantity that follows.

With the substitution of Equation 27, Equation 33 may be integrated in closed form as

$$\frac{\partial W}{\partial t} = -\frac{\sqrt{3}\, c\left(\gamma^2 - \frac{1}{3}\right)^{1/2}}{16\pi r^2 \mu}\, \mathrm{Im}\left\{ \frac{S_o}{\alpha}\left[\left(2\gamma^2 - 1\right)\left(\frac{1}{\sqrt{\chi^2 - \gamma^2}} - \frac{1}{\sqrt{(\chi + \alpha)^2 - \gamma^2}}\right) - 2\gamma^2\left(\frac{1}{\sqrt{\Omega^2 - \gamma^2}} - \frac{1}{\sqrt{(\Omega + \alpha)^2 - \gamma^2}}\right)\right] + S_1\left[\frac{\left(2\gamma^2 - 1\right)\left(\chi + \alpha\right)}{\left(\left[\chi + \alpha\right]^2 - \gamma^2\right)^{3/2}} - \frac{2\gamma^2(\Omega + \alpha)}{\left(\left[\Omega + \alpha\right]^2 - \gamma^2\right)^{3/2}}\right]\right\} \tag{34a}$$

where

$$\chi = \tau + i\ell\left(\gamma^2 - \frac{1}{3}\right)^{1/2} \tag{34b}$$

$$\Omega = \tau + i\ell\left(\gamma^2 - 1\right)^{1/2} \tag{34c}$$

$$\tau = \frac{ct}{r} \tag{34d}$$

$$\alpha = \frac{a\gamma^2}{cr} \tag{34e}$$

and

$$\ell = \frac{z}{r} \tag{34f}$$

Equation 34a, the Rayleigh phase of the vertical velocity of the medium, is plotted in Figures 45 to 52 in which the ordinate is the nondimensional vertical velocity and the abscissa is the nondimensional time τ. The meanings of various parameters in these drawings are explained in Figures 41 and 42.

Solution for Large Depth of Station - Region II. $z/r >> 1$

For stations near the loading zone and deep underground, r, the radial distance, may be assumed to be zero in comparison with the depth, see Figure 42. The Laplace transform of the vertical displacement then may be written as

$$\bar{w}\ (o,p,z) = \int_0^\infty w\ (o,t,z)\ e^{-pt} dt$$

$$= \int_0^\infty W\ (\xi,p,z)\ \xi\ d\xi \tag{35}$$

according to Equations 22a and 23b with $J_0\ (\xi r)$ evaluated at $r = 0$. Let a change of variable

$$\xi = \frac{px}{c} = kx \tag{36}$$

be introduced in Equation 35. Substitution of Equations 27 and 28 yields

$$\bar{w}(o,p,z) = -\frac{1}{2\pi\mu}\int_{o}^{\infty}\left\{\frac{\left(x^{2}+\frac{1}{3}\right)^{1/2}\left[\left(2x^{2}+1\right)e^{-\beta_1} - 2x^{2}e^{-\beta_2}\right]}{\left(\left(2 x 2 + 1\right)^{2} - 4x^{2}\left(x^{2}+\frac{1}{3}\right)^{1/2}\left(x^{2}+1\right)^{1/2}\right)}\right.$$

$$\left.\cdot\left[S_o\frac{1-\exp\left(-p\alpha_1 z x^{2}/c\right)}{p\alpha_1 z x} + S_1\frac{x}{c}\exp\left(-p\alpha_1 z x^{2}/c\right)\right]\right\} dx = \bar{w}_o + \bar{w}_1 \quad (37a)$$

where

$$\beta_1 = \frac{pz}{c}\sqrt{x^{2}+\frac{1}{3}} \quad (37b)$$

$$\beta_2 = \frac{pz}{c}\sqrt{x^{2}+1} \quad (37c)$$

$$\alpha_1 = \frac{a}{cz} \quad (37d)$$

The first part of the integral related to S_o, hereafter denoted as w_o, is the difference of two divergent integrals and therefore is difficult to obtain. To avoid this difficulty, the S_o term will be rewritten in terms of a definite integral as

$$S_o\,\frac{1-e^{-p\alpha_1 z x^{2}/c}}{p\alpha_1 z x} = \frac{x}{c}\int_{o}^{\alpha_1} e^{-p\beta z x^{2}/c}\,d\beta \quad (38)$$

Substituting this integral in Equation 37a and noting the similarities of the S_o and S_1 term, Equation 37a may be written as

$$\bar{w} = \bar{w}_o + \bar{w}_1$$

$$= \frac{-1}{2\pi\mu c}\left[S_o\int_o^{\alpha_1} f\,(\beta,p,z)\;d\beta + S_1\; f\left(\alpha_1,p,z\right)\right] \qquad (39)$$

where

$$f\,(\beta,p,z) = I_1 - I_2$$

and

$$I_1 = \int_o^{\infty} \frac{x\left(x^2+\frac{1}{3}\right)^{1/2}\left(2\,x^2+1\right)e^{-p\left[z\,\sqrt{x^2+\frac{1}{3}}\,+\,\beta z x^2\right]/c}}{\left(2\,x^2+1\right)^2-4\,x^2\left(x^2+\frac{1}{3}\right)^{1/2}\left(x^2+1\right)^{1/2}}\,dx \qquad (40a)$$

$$I_2 = \int_o^{\infty} \frac{2\,x^3\left(x^2+\frac{1}{3}\right)^{1/2}\,e^{-pz}\left[\sqrt{x^2+1}+\beta x^2\right]/c}{\left(2\,x^2+1\right)-4\,x^2\left(x^2+\frac{1}{3}\right)^{1/2}\left(x^2+1\right)^{1/2}}\,dx \qquad (40b)$$

Recalling that $\bar{w}$ is the Laplace transform of the vertical displacement w by Equation 22a, it is seen that the quantities I_1, I_2, in Equations 40a, and 40b, therefore, are the Laplace transforms of some function, say K_1 and K_2 such that

$$\left[I_1\;(p,z,\beta),\;I_2\;(p,z,\beta)\right] = \int_o^{\infty}\left[K_1\;(t,z,\beta),\;K_2\;(t,z,\beta)\right]e^{-pt}\,dt \qquad (41)$$

It is therefore apparent that the determination of the vertical velocity $\dot{w}$ hinges on the determination of K_1 and K_2 of Equation 41. To this end let

$$\frac{z}{c}\left[\sqrt{x^2+\frac{1}{3}}+\beta x^2\right] = t \tag{42a}$$

in Equation 40a, which corresponds to

$$x = \left[\frac{2\left(\tau_1^2-\frac{1}{3}\right)}{2\tau_1\beta+1+\sqrt{4\tau_1\beta+1+\frac{4}{3}\beta^2}}\right]^{1/2} \tag{42b}$$

where

$$\tau_1 = \frac{ct}{z} \tag{42c}$$

is a nondimensional time. It may be noted that the form of Equation 42b is expressed in such a way that no ambiguity will arise when β → 0. Furthermore, all square roots are chosen to be positive.

Substitution of Equations 42a, 42b and 42c into Equation 40a, with some mathematical manipulation yields the result.

$$I_1 = \frac{2c}{z}\int_{\frac{z}{c\sqrt{3}}}^{\infty} \frac{\left(x^2+\frac{1}{3}\right)^{1/2}}{\left[\left(2x^2+1\right)^2-4x^2\sqrt{x^2+1}\sqrt{x^2+\frac{1}{3}}\right]} \bullet \frac{\left(2x^2+1\right)\left(\tau_1+\frac{\beta}{3}\right)e^{-pt}}{\left[4\tau_1\beta+1+\frac{4}{3}\beta^2+\sqrt{4\tau_1\beta+1+\frac{4}{3}\beta^2}\right]}\,dt \tag{43}$$

Comparing this expression with that of Equation 41, it can be seen that

$$K_1\ (t,z,\beta)\ =\ \frac{2c\left(x^2+\frac{1}{3}\right)^{1/2}}{z\left[\left(2\ x^2+1\right)^2-4\ x^2\sqrt{x^2+1}\ \sqrt{x^2+\frac{1}{3}}\right]}$$

$$\bullet\ \frac{\left(2\ x^2+1\right)\left(\tau_1+\frac{\beta}{3}\right)}{\left[4\tau_1\beta+1+\frac{4}{3}\beta^2+\sqrt{4\tau_1\beta+1+\frac{4}{3}\beta^2}\right]} \qquad (44)$$

$$\text{for}\quad \tau_1 > \frac{1}{\sqrt{3}}$$

$$K_1\ (t,z,\beta)\ =\ 0$$

$$\text{for}\quad \tau_1 < \frac{1}{\sqrt{3}}$$

where x and τ_1 are defined in Equations 42b and 42c

Similarly, let

$$\frac{z}{c}\left[\sqrt{x^2+1}+\beta x^2\right]\ =\ t \qquad (45a)$$

in Equation 40b which leads to

$$x\ =\ \left[\frac{2\left(\tau_1^2-1\right)}{2\tau_1\beta+1+\sqrt{4\tau_1\beta+1+4\beta^2}}\right]^{1/2} \qquad (45b)$$

$$K_2\ (t,z,\beta) = \frac{4cx^2}{z\left[\left(2\ x^2+1\right)^2-4\ x^2\sqrt{x^2+1}\sqrt{x^2+\frac{1}{3}}\right]}$$

$$\cdot \frac{\left(x^2+\frac{1}{3}\right)^{1/2}}{\left[4\tau_1\beta+1+4\beta^2+\sqrt{4\tau_1\beta+1+4\beta^2}\right]} \qquad (46)$$

$$\text{for} \quad \tau_1 > 1$$

$$K_2\ (t,z,\beta) = 0$$

$$\text{for} \quad \tau_1 < 1$$

where x is defined in Equation 45b,

Referring back to Equations 22a, 39, 40a, and 40b, it can be seen that the vertical displacement of the medium directly below the loading zone is

$$w\ (o,t,z) = -\frac{1}{2\pi\mu c}\left\{S_o\int_o^{\alpha_1}\left[K_1\ (t,z,\beta)-K_2\ (t,z,\beta)\right]d\beta\right.$$

$$\left. +\ S_1\left[K_1\ \left(t,z,\alpha_1\right)-K_2\ \left(t,z,\alpha_1\right)\right]\right\} \qquad (47)$$

where K_1, K_2 are defined in Equations 44 and 46 respectively. The vertical velocity of the medium can be easily obtained by a direct differentiation, namely

$$\dot{w}\ (o,t,z) = \frac{d}{dt}\ w\ (o,t,z) \qquad (48)$$

DISTRIBUTION

No. cys	
	HEADQUARTERS USAF
	Hq USAF, Wash, DC 20330
3	(AFOCE)
1	(AFRDQ)
1	(AFTAC)
1	(AFRSTG)
1	USAF Dep, The Inspector General (AFIDI), Norton AFB, Calif 92409
1	USAF Directorate of Nuclear Safety (AFINS), Kirtland AFB, NM 87117
	MAJOR AIR COMMANDS
	AFSC, Andrews AFB, Wash, DC 20331
1	(SCTR)
1	(SCTN)
1	TAC (DORQ-M), Langley AFB, Va 23365
1	AUL, Maxwell AFB, Ala 36112
1	CINPACAF (DCEEE), APO San Francisco 96553
1	USAFA (DFLBA), Colo 80840
	AFSC ORGANIZATIONS
1	AFSC Scientific and Technical Liaison Office, Research and Technology Division, AFUPO, Los Angeles, Calif 90045
1	FTD (TDBTL), Wright-Patterson AFB, Ohio 45433
1	AF Materials Laboratory, Wright-Patterson AFB, Ohio 45433
1	AF Flight Dynamics Laboratory, Wright-Patterson AFB, Ohio 45433
1	AF Aero-Propulsion Laboratory, Wright-Patterson AFB, Ohio 45433
1	SEG (SEPIR), Wright-Patterson AFB, Ohio 45433
	RTD, Bolling AFB, Wash, DC 20332
1	(RTTW)
1	(RTS)
1	AF Msl Dev Cen (SRRT), Holloman AFB, NM 88330
1	AEDC (AEYD), Arnold AFS, Tenn 37289
1	SSD (SSSD), Los Angeles AFS, AFUPO, Los Angeles, Calif 90045
1	ESD (ESTI), L. G. Hanscom Fld, Bedford, Mass 01731
	BSD, Norton AFB, Calif 92409
1	(BSR)
1	(BSR-1)
1	(BSSF)
1	(BSQR)

DISTRIBUTION (cont'd)

No. cys	
1	RADC (EMLAL-1), Griffiss AFB, NY 13442
	KIRTLAND AFB ORGANIZATIONS
	AFSWC, Kirtland AFB, NM 87117
1	(SWEH)
1	(SWT)
1	SAC Res Rep (SACLO), AFSWC, Kirtland AFB, NM 87117
1	TAC Liaison Office (TACLO-S), AFSWC, Kirtland AFB, NM 87117
	AFWL, Kirtland AFB, NM 87117
10	(WLIL)
1	(WLAS)
20	(WLDC)
	OTHER AIR FORCE AGENCIES
	Director, USAF Project RAND, via: Air Force Liaison Office, The RAND Corporation, 1700 Main Street, Santa Monica, Calif 90406
1	(RAND Physics Div)
1	(RAND Library)
1	OAR (RROS), 1400 Wilson Blvd, Arlington, Va 22209
1	AFOSR (SRGL), 1400 Wilson Blvd, Arlington, Va 22209
1	AFCRL, L. G. Hanscom Fld, Bedford, Mass 01731
	ARMY ACTIVITIES
1	Commanding Officer, Ballistic Research Laboratories, (AMXBR-TB, Mr. J. Meszaros), Aberdeen Proving Ground, Md 21005
1	Chief of Engineers (ENGMC-EM), Department of the Army, Wash, DC 20315
1	Director, Army Research Office, 3045 Columbia Pike, Arlington, Va 22204
1	Director, US Army Waterways Experiment Sta (WESRL), P. O. Box 631, Vicksburg, Miss 39181
2	Director, US Army Engineer Research and Development Laboratories, ATTN: STINFO Branch, Ft Belvoir, Va 20260
1	US Army Engineer Division, Ohio River, Corps of Engineers (ORDLBVR), 5851 Mariemont Avenue, Mariemont, Cincinnati, Ohio 45227
	NAVY ACTIVITIES
1	Chief of Naval Research, Department of the Navy, Wash, DC 20390
1	Naval Air Systems Command (RRNU), Department of the Navy, Wash, DC 20360
1	Facilities Engineering Command, Department of the Navy, Code 22.102 (Branch Manager, Code 42.330), Wash, DC 20360

DISTRIBUTION (cont'd)

No. cys	
1	Commanding Officer, Naval Research Laboratory, Wash, DC 20390
1	Commanding Officer and Director, David Taylor Model Basin, Wash, DC 20007
1	Superintendent, US Naval Postgraduate School, ATTN: George R. Luckett, Monterey, Calif 93940
1	Commanding Officer and Director, Naval Civil Engineering Laboratory, Port Hueneme, Calif 93041
1	Commanding Officer and Director, Naval Applied Science Laboratory, Brooklyn, NY 11251
1	Commander, Naval Ordnance Laboratory, ATTN: Dr. Rudlin, White Oak, Silver Spring, Md 20910
1	Officer-in-Charge, Naval Civil Engineering Corps Officers School, US Naval Construction Battalion Center, Port Hueneme, Calif 93041
1	Office of Naval Research, Wash, DC 20360
1	Commanding Officer, NWEF (Code WE), Kirtland AFB, NM 87117
	OTHER DOD ACTIVITIES
2	Director, DASA (Document Library Branch), Wash, DC 20301
1	Commander, Field Command, DASA (FCAG3, Special Weapons Publication Distribution), Sandia Base, NM 87115
1	Director, Weapon Systems Evaluation Group, Wash, DC 20305
1	Director, ARPA, DoD, The Pentagon, Wash, DC 20301
1	Office of Director of Defense Research and Engineering, ATTN: John E. Jackson, Office of Atomic Programs, Rm 3E1071, The Pentagon, Wash, DC 20330
1	US Documents Officer, Office of the US National Military Representative (SHAPE), New York, NY 09055
20	DDC (TIAAS), Cameron Station, Alexandria, Va 22314
	AEC ACTIVITIES
1	Sandia Corporation (Information Distribution Division), Box 5800, Sandia Base, NM 87115
1	Sandia Corporation (Tech Library), P. O. Box 969, Livermore, Calif 94551
1	University of California Lawrence Radiation Laboratory, ATTN: Director's Office, P. O. Box 808, Livermore, Calif 94551
	OTHER
1	Massachusetts Institute of Technology, Lincoln Laboratory (Document Library), P. O. Box 73, Lexington, Mass 02173
1	Aerospace Corporation, P. O. Box 95085, Los Angeles, Calif 90045
1	Aerospace Corporation, ATTN: Ali M. Naqvi, San Bernardino Operations, P. O. Box 1308, San Bernardino, Calif 92402

DISTRIBUTION (cont'd)

No. cys	
1	NASA Scientific and Technical Information Facility, ATTN: Document Services Dept, P. O. Box 33, College Park, Md 20740
1	Kaman Nuclear, Div of Kaman Aircraft Corporation, ATTN: Dr. A. P. Bridges, Garden of the Gods Road, Colorado Springs, Colo 80907
20	The Ralph M. Parsons Company, ATTN: Mr. Herbert R. Saffell, 617 West Seventh Street, Los Angeles, Calif 90017
1	Applied Theory, ATTN: John G. Trulio, 1950 Cotner Avenue, West Los Angeles, Calif 90025
1	Battelle Memorial Institute, ATTN: William L. Buckel, 505 King Avenue, Columbus, Ohio 43201
1	The Boeing Company, ATTN: F. H. Carlson, 1701 First National Bank Bldg East, 5301 Central Avenue NE, Albuquerque, NM 87108
1	Bell Telephone Laboratories, Inc., ATTN: L. W. Fagel, Whippany, NJ 07981
1	Carnegie Institute of Technology, ATTN: Thomas E. Stelson, Schenley Park, Pittsburgh, Pa 15213
1	Duke University, ATTN: Aleksandar S. Vesic, Dept of Civil Engineering, Durham, NC 27706
1	University of New Mexico, CERF, ATTN: Dr. Zwoyer, Box 188, University Station, Albuquerque, NM 87106
1	Engineering Mechanics Laboratory, ATTN: Millard V. Barton, TRW Systems, One Space Park, Redondo Beach, Calif 90278
1	General American Research Division, General American Transportation Corporation, ATTN: G. I. Neidhardt, 7449 N. Natchez Ave, Niles, Ill 60648
1	General Electric Company, Missile and Space Division, ATTN: Lawrence I. Chasen, P. O. Box 8555, Philadelphia, Pa 19101
1	IIT Research Institute, ATTN: C. A. Miller, 10 West 35 Street, Chicago, Ill 60616
1	Michigan Technological University, ATTN: George A. Young, Dept of Civil Engineering, Houghton, Mich 49931
1	The Mitre Corporation, ATTN: Mr. Walter Gunther, P. O. Box 208, Bedford, Mass 01730
1	North Carolina State University, ATTN: R. E. Fadum, School of Engineering, Office of the Dean, Box 5518, Raleigh, NC 27607
1	National Engineering Science Company, ATTN: Dr. Lewis B. McCammon, 711 South Fair Oaks Avenue, Pasadena, Calif 91105
1	Northwestern University, ATTN: Dr. Robert L. Kondner, Civil Engineering Dept, Technological Institute, Evanston, Ill 60201
1	OSA-OCD The Pentagon, ATTN: Eugene J. Taylor, A/E Services Div, Univ Projects Branch, Wash, DC 20301
1	Polytechnic Institute of Brooklyn, ATTN: Robert B. B. Moorman, Dept of Civil Engineering, 333 Jay St, Brooklyn, NY 11201

DISTRIBUTION (cont'd)

No. cys	
1	Paul Weidlinger, 777 Third Avenue, New York, NY 10017
1	Princeton University, ATTN: Norman J. Sollenberger, School of Engineering and Applied Science, Princeton, NJ 08540
1	Purdue University, ATTN: G. A. Leonards, School of Civil Engineering, Lafayette, Ind 47907
1	Rice University, ATTN: A. S. Veletsos, Dept of Civil Engineering, Houston, Tex 77001
1	Rensselaer Polytechnic Institute, ATTN: Prof. J. M. Beatty, Dept of Civil Engineering, Troy Building, Troy, NY 12180
1	Southwest Research Institute, ATTN: Robert C. DeHart, Dept of Structural Research, 8500 Culebra Road, San Antonio, Tex 78228
1	Stanford Research Institute, ATTN: Jean L. Moncur, Menlo Park, Calif 94025
1	San Jose State College, ATTN: Franklin J. Agardy, Dept of Civil Engineering, San Jose, Calif 95100
1	Shannon and Wilson, Inc., ATTN: Earl A. Sibley, 1105 N. 38 Street, Seattle, Wash 98103
1	Tulane University, ATTN: Walter E. Blessey, Dept of Civil Engineering, New Orleans, La 70112
1	Texas A&M University, ATTN: Dr. C. H. Samson, Jr., Civil Engineering Dept, College Station, Tex 77843
1	University of Notre Dame, ATTN: Bruce B. Schimming, Dept of Civil Engineering, Notre Dame, Ind 46556
1	University of New Mexico, ATTN: Richard H. Clough, College of Engineering, Albuquerque, NM 87106
1	University of Arizona, ATTN: Charles H. Peyton, College of Engineering, Tucson, Ariz 85721
1	University of Denver, ATTN: Dr. Rudolph Szilard, Senior Engineer, Denver Research Institute, University Park, Denver, Colo 80210
1	University of Missouri, ATTN: Adrian Pauw, College of Engineering, Dept of Civil Engineering, Columbia, Mo 65201
1	University of Rhode Island, ATTN: Vito A. Nacci, Dept of Civil Engineering, Kingston, RI 02881
1	University of California, Los Angeles, ATTN: C. Martin Duke, Dept of Engineering, Los Angeles, Calif 90024
1	University of Illinois, ATTN: Dr. N. M. Newmark, Dept of Civil Engineering, 205 Engineering Hall, Urbana, Ill 61803
1	University of Kentucky, ATTN: Prof Bobby O. Hardin, Dept of Civil Engineering, Lexington, Ky 40506
1	University of Washington, ATTN: Bill Miller, Dept of Civil Engineering, 307 More Hall, Seattle, Wash 98105
1	University of Massachusetts, ATTN: Merit P. White, Dept of Civil Engineering, Amherst, Mass 01002

DISTRIBUTION (cont'd)

No. cys	
1	Worchester Polytechnic Institute, ATTN: Carl Koontz, Dept of Civil Engineering, Worchester, Mass 01600
1	West Virginia University, ATTN: James H. Schaub, Dept of Civil Engineering, Morgantown, WVa 26506
1	Aerospace Corporation, 1111 East Mill Street, San Bernardino, Calif 92408
1	Columbia University, ATTN: R. D. Stoll, Dept of Civil Engineering, and Engineering Mechanics, Seeley W. Mudd Bldg, New York, NY 10027
1	Auburn University, ATTN: Donald A. Sawyer, Civil Engineering, Auburn, Ala 36830
1	University of Dayton, ATTN: Seymour James Ryckman, Dept of Civil Engineering and Engineering Mechanics, Dayton, Ohio 45409
1	Rensselaer Polytechnic Institute, Dept of Civil Engineering, ATTN: E. C W. A. Guese, Soil Mechanics and Foundation Engineering (Info Only), Troy Bldg, Troy, NY 12180
1	Official Record Copy (Lt Williams, WLDC)

UNCLASSIFIED
Security Classification

DOCUMENT CONTROL DATA - R&D

(Security classification of title, body of abstract and indexing annotation must be entered when the overall report is classified)

1. ORIGINATING ACTIVITY (Corporate author)
The Ralph M. Parsons Company
617 West Seventh Street
Los Angeles, California 90017

2a. REPORT SECURITY CLASSIFICATION
UNCLASSIFIED

2b. GROUP

3. REPORT TITLE
STUDY OF WAVEFORM CHARACTERISTICS FOR USE IN THE ANALYSIS OF SHOCK ISOLATION SYSTEMS FOR UNDERGROUND PROTECTIVE STRUCTURES

4. DESCRIPTIVE NOTES (Type of report and inclusive dates)
22 December 1963-13 December 1966

5. AUTHOR(S) (Last name, first name, initial)
Saffell, H. R., The Ralph M. Parsons Company; Frankian, R. T., R. T. Frankian and Associates; Chao, C. C., Agbabian-Jacobsen Associates

6. REPORT DATE
January 1967

7a. TOTAL NO. OF PAGES
148

7b. NO. OF REFS
27

8a. CONTRACT OR GRANT NO. AF 29(601)-6277

b. PROJECT NO. 1080

c. Task No. 108015

d. Subtask No. 13.167

9a. ORIGINATOR'S REPORT NUMBER(S)
AFWL-TR-65-67

9b. OTHER REPORT NO(S) (Any other numbers that may be assigned this report)

10. AVAILABILITY/LIMITATION NOTICES This document is subject to special export controls and each transmittal to foreign governments or foreign nationals may be made only with prior approval of AFWL (WLDC), Kirtland AFB, NM, 87117. Distribution is limited because of the technology discussed in the report.

11. SUPPLEMENTARY NOTES

12. SPONSORING MILITARY ACTIVITY
AFWL (WLDC)
Kirtland AFB, NM 87117

13. ABSTRACT

A recent review of nuclear groundshock test data revealed oscillatory motions of undetermined origin, but of sufficient magnitude to be of concern in the design of shock isolation systems for underground protective structures. Response spectra of the oscillations exhibited amplification ratios far exceeding those employed in most groundshock prediction methods, the ratios being functions of the number of oscillations, and the amplitude and period of each cycle. As the source of the oscillations was not identified, there was no rational basis for relating these waveform parameters to such basic site and weapon conditions as yield, range, geologic structure and properties of the medium. In this investigation, two possible sources of the oscillatory motion are examined. First, the propagation of waves in a stratified site are studied and their directions and phase relationships estimated by use of wavefront diagrams and time-distance curves. Second, the form and strength of Rayleigh waves in an elastic, homogeneous half-space which result from surface pressure distributions similar to those generated by nuclear bursts were calculated. In both cases, oscillatory phenomena can be predicted and certain features related to the observed oscillations. However, the simple approaches employed in this analysis will not yield realistic wave strengths and thus, the composite waveform at a point in the half-space cannot be determined quantitatively.

(DISTRIBUTION LIMITATION STATEMENT NO. 2)

DD FORM 1 JAN 64 **1473**

UNCLASSIFIED
Security Classification

14. KEY WORDS	LINK A		LINK B		LINK C	
	ROLE	WT	ROLE	WT	ROLE	WT
Shock isolation						
Groundshock						
Wave propagation						
Wavefront diagrams						
Time-distance curves						
Rayleigh waves						
Energy transmission						
Energy reflection						

INSTRUCTIONS

1. **ORIGINATING ACTIVITY:** Enter the name and address of the contractor, subcontractor, grantee, Department of Defense activity or other organization (*corporate author*) issuing the report.

2a. **REPORT SECURITY CLASSIFICATION:** Enter the overall security classification of the report. Indicate whether "Restricted Data" is included. Marking is to be in accordance with appropriate security regulations.

2b. **GROUP:** Automatic downgrading is specified in DoD Directive 5200.10 and Armed Forces Industrial Manual. Enter the group number. Also, when applicable, show that optional markings have been used for Group 3 and Group 4 as authorized.

3. **REPORT TITLE:** Enter the complete report title in all capital letters. Titles in all cases should be unclassified. If a meaningful title cannot be selected without classification, show title classification in all capitals in parenthesis immediately following the title.

4. **DESCRIPTIVE NOTES:** If appropriate, enter the type of report, e.g., interim, progress, summary, annual, or final. Give the inclusive dates when a specific reporting period is covered.

5. **AUTHOR(S):** Enter the name(s) of author(s) as shown on or in the report. Enter last name, first name, middle initial. If military, show rank and branch of service. The name of the principal author is an absolute minimum requirement.

6. **REPORT DATE:** Enter the date of the report as day, month, year; or month, year. If more than one date appears on the report, use date of publication.

7a. **TOTAL NUMBER OF PAGES:** The total page count should follow normal pagination procedures, i.e., enter the number of pages containing information.

7b. **NUMBER OF REFERENCES:** Enter the total number of references cited in the report.

8a. **CONTRACT OR GRANT NUMBER:** If appropriate, enter the applicable number of the contract or grant under which the report was written.

8b, 8c, & 8d. **PROJECT NUMBER:** Enter the appropriate military department identification, such as project number, subproject number, system numbers, task number, etc.

9a. **ORIGINATOR'S REPORT NUMBER(S):** Enter the official report number by which the document will be identified and controlled by the originating activity. This number must be unique to this report.

9b. **OTHER REPORT NUMBER(S):** If the report has been assigned any other report numbers (*either by the originator or by the sponsor*), also enter this number(s).

10. **AVAILABILITY/LIMITATION NOTICES:** Enter any limitations on further dissemination of the report, other than those imposed by security classification, using standard statements such as:

(1) "Qualified requesters may obtain copies of this report from DDC."

(2) "Foreign announcement and dissemination of this report by DDC is not authorized."

(3) "U. S. Government agencies may obtain copies of this report directly from DDC. Other qualified DDC users shall request through
__________________________________."

(4) "U. S. military agencies may obtain copies of this report directly from DDC. Other qualified users shall request through
__________________________________."

(5) "All distribution of this report is controlled. Qualified DDC users shall request through
__________________________________."

If the report has been furnished to the Office of Technical Services, Department of Commerce, for sale to the public, indicate this fact and enter the price, if known.

11. **SUPPLEMENTARY NOTES:** Use for additional explanatory notes.

12. **SPONSORING MILITARY ACTIVITY:** Enter the name of the departmental project office or laboratory sponsoring (*paying for*) the research and development. Include address.

13. **ABSTRACT:** Enter an abstract giving a brief and factual summary of the document indicative of the report, even though it may also appear elsewhere in the body of the technical report. If additional space is required, a continuation sheet shall be attached.

It is highly desirable that the abstract of classified reports be unclassified. Each paragraph of the abstract shall end with an indication of the military security classification of the information in the paragraph, represented as *(TS)*, *(S)*, *(C)*, or *(U)*.

There is no limitation on the length of the abstract. However, the suggested length is from 150 to 225 words.

14. **KEY WORDS:** Key words are technically meaningful terms or short phrases that characterize a report and may be used as index entries for cataloging the report. Key words must be selected so that no security classification is required. Identifiers, such as equipment model designation, trade name, military project code name, geographic location, may be used as key words but will be followed by an indication of technical context. The assignment of links, rules, and weights is optional